UNIVERSITY OF CALIFORNIA, SAN DIEGO

Energy Harvesting Paradigms for Autonomously-Powered Sensor Networks

A dissertation submitted in partial satisfaction of the
requirements for the degree Doctor of Philosophy

in

Structural Engineering

by

Scott Anthony Ouellette

Committee in charge:

Professor Michael Todd, Chair
Professor Yuri Bazilevs
Professor William Hodgkiss
Professor Francesco Lanza di Scalea
Professor Patrick Mercier

2015

The Dissertation of Scott Anthony Ouellette is approved, and it is acceptable in quality and form for publication on microfilm and electronically:

_____

_____

_____

_____

_____

Chair

University of California, San Diego

2015

DEDICATION

To my grandfather, Al Vela. Everything I know about family, love, community, and integrity I learned from our many summer days at the driving range. While I will forever miss your presence, the gift of your knowledge and mentorship will always remain with me to serve as a guiding set of principles to live my life; for what we have once enjoyed and deeply loved we can never lose, for all that we love deeply becomes a part of us. I dedicate this dissertation to the memory of who you were, and for the family you built.

EPIGRAPH

"The price of success is hard work, dedication to the job at hand,
and determination that whether we win or lose,
we have applied the best of ourselves to the task at hand".

Vince Lombardi

"The worthwhile problems are the one you can really solve or help solve,
the ones you can really contribute something to…
No problem is too small or too trivial if we can really do something about it".

Richard Feynman

"They say there are no stupid questions. That's obviously wrong…
But it turns out that trying to thoroughly answer a stupid question
can take you to some pretty interesting places".

Randall Munroe

"Things turn out the best for people who make the best of the way things turn out".

John Wooden

"I may not have gone where I intended to go,
but I think I have ended up where I needed to be".

Douglas Adams

TABLE OF CONTENTS

LIST OF ABBREVIATIONS

SHM	Structural Health Monitoring
MIG	Modulated Inertial Generator
DAQ	Data Acquisition
LDV	Laser-Doppler Vibrometer
IC	Integrated Circuit
AC	Alternating Current
DC	Direct Current
SPICE	Simulation Program with Integrated Circuit Emphasis
CMOS	Complimentary Metal-Oxide Semiconductor
PCB	Printed Circuit Board
PZT	Piezoelectric Transducer
PWM	Pulse-Width Modulation

LIST OF SYMBOLS

t	Time
x	Spatial coordinate
θ	Rotation of MIG beam tip
$\phi(x)$	Mode shape
$\omega[x,t]$	Lateral displacement of MIG
λ	Nondimensional eigenvalue parameter
$i(t)$	Instantaneous current (electrical)
$V(t)$	Voltage (electrical)
nI	Total current (electrical)
B	Magnetic flux density vector
H	Magnetic coercive force vector
Φ	Magnetic flux path
$R_{c/gap}$	Core/gap reluctance
μ_0	Permeability of free space
B_r	Remnant flux density
μ	Magnetic dipole moment vector
r	Position vector for repulsing magnet displacement
U	Potential energy
ζ	Damping ratio
ω_n	Natural frequency
E	Modulus of elasticity
I	Second moment of area
Ω	Ohms (resistance)
Hz	Hertz

LIST OF FIGURES

LIST OF TABLES

ACKNOWLEDGEMENTS

I first and foremost would like to begin by acknowledging my advisor, Professor Michael Todd. While periods of personal growth are often fraught with difficulties, under your stewardship I was able to mature into a self-reliant engineer with a suite of technical abilities ready to forge an exciting career in engineering and technical leadership. I look forward to our future research collaborations, and I cannot thank you enough for the support and guidance you have provided me.

I feel honored to have collaborated with the talented engineers of the UCSD SHM research group. The jovial atmosphere and rousing technical discussions made the Ph.D. process seem more akin to play, rather than work. In particular, I'd like to acknowledge Colin Haynes, Dustin Harvey, Richard Do, Eric Flynn, Greg Jarmer, and Zhu Mao for your constructive feedback and comraderie. You gentlemen are my academic brothers, and I look forward to many years of fruitful collaboration.

It has been my pleasure to serve my home department as a teaching assistant, and I'd like to acknowledge the friendships I've developed with my fellow TA's and teaching faculty throughout the years. Namely, I'd like to share my gratitude with Sam Lee, Andrew Sander, Michael Daneshvar, Reverend Steve Porter, and Dr. Lelli Van Den Einde. Many long nights were shared over mountains of exams in need of grading, and – strangely enough – these memories are often what I cherish most upon reflection.

I'd also like to express my love and gratitude to all of my family and friends who supported me throughout the Ph.D. process. My parents, Ken Ouellette and Elaina Phillips, played a central role in this regard. I thank you both for your unwavering love and support, and for my wonderful step-parents, Debbie and Dean. Dad – our golf adventures were a much needed source of stress relief. Mom – your attentive listening and warm advice have always kept

me grounded and humble. To my older brother, Chris, I am deeply thankful for your guidance, and friendship. I have always looked to you as my role model in life, and I consider myself blessed to have you, Coleen and Sofía. To my younger step-brother, Corey, I thank you for sharing so much of your life with me by letting me be your brother. It is a badge of honor that I wear with pride, and I can't wait to watch you take the world by storm.

To my wonderful in-laws, Stuart and Lorraine Rumley, I cannot thank you enough for your love, support, advice, and encouragement at every step. To my sister-in-law, Brooke, you are uniquely awesome in so many ways. Words cannot fully describe the gratitude I have for being welcomed into your family.

Finally, I would like to thank my wife, Brittany. It seems like yesterday when you asked to sit next to me in Statics, and I'll never forget the moment of realization in Bristol, England when I decided that I wanted to spend the rest of my life with you. I wake up every day in awe of your tireless work ethic, professionalism, dedication to community service, and warm personality. Who you are challenges and inspires me to be a better human being. Our journey together has just begun, and I can't wait to see where our next adventure takes us.

The research presented in this dissertation was primarily funded by the National Science Foundation, through a Graduate Research Fellowship.

A portion of Chapter 1 and a portion of Chapter 4 are to be submitted as a technical report for Los Alamos National Laboratory, Scott Ouellette, Charles Farrar, and Michael Todd, 2015. The title of this report is "Energy Harvesting for Autonomous Sensor Networks." The dissertation author was the primary investigator and author of this paper.

A portion of Chapter 2 and a portion of Chapter 3 have been published in IEEE Sensors Journal, Scott Ouellette and Michael Todd, 2013. The title of this paper is "Cement Sea-Water

Battery for Marine Infrastructure Monitoring". The dissertation author was the primary investigator and author of this paper.

A significant portion of Chapter 5 has been submitted for publication in Smart Materials and Structures, Scott Ouellette and Michael Todd, 2015. The title of this paper is "Modulating the Bistable Potential Energy Separatrix for Augmented Broadband Vibration Energy Harvesting". The dissertation author was the primary investigator and author of this paper.

A portion of Chapter 2 and a portion of Chapter 3 has been published in Proc. of SPIE, Scott Ouellette and Michael Todd, 2012. The title of this paper is "Ultra-Low Power Corrosion-Enabled Sensor Node". The dissertation author was the primary investigator and author of this paper.

Another portion of Chapter 2 and a portion of Chapter 3 have been published in Proc. of SPIE, Scott Ouellette and Michael Todd, 2013. The title of this paper is "Uncertainty Quantification of a Corrosion-Enabled Energy Harvester for Low-Power Sensing Applications". The dissertation author was the primary investigator and author of this paper.

Another portion of Chapter 3 has been published in Proc. of SMASIS, Scott Ouellette and Michael Todd, 2013. The title of this paper is "A Systematic Approach to Corrosion-Powered Sensor Network Design". The dissertation author was the primary investigator and author of this paper.

A portion of Chapter 5 has been published in Proc. of SPIE, Scott Ouellette and Michael Todd, 2014. The title of this paper is "Broadband Energy Harvesting via Adaptive Control of the Bistable Potential Energy Separatrix". The dissertation author was the primary investigator and author of this paper.

VITA

2009	B.S. in Structural Engineering	University of California, San Diego
2011	M.S. in Structural Engineering	University of California, San Diego
2015	Ph.D. in Structural Engineering	University of California, San Diego

PUBLICATIONS

*Work that has been incorporated into this dissertation

Peer Reviewed Journal Articles

Gallant TB, Van Den Einde L, Ouellette S, Lee S. "A Systematic Analysis of Cheating in an Undergraduate Engineering Mechanics Course." Science and Engineering Ethics. 2014 Mar 1; 20(1):277-298.

*Ouellette S, Todd M. "Cement Sea-Water Battery Energy Harvester for Marine Infrastructure Monitoring." Sensors Journal, IEEE. 2013 Nov 11; 14(3):865–872.

Journal Articles in Progress

*Ouellette S and Todd M. "Modulating the Bistable Potential Energy Separatrix for Augmented Broadband Vibration Energy Harvesting." Smart Materials and Structures.

Conference Proceedings

*Ouellette S, Todd M. "Broadband energy harvesting via adaptive control of the bistable potential energy separatrix." SPIE San Diego, CA: 2014.

*Ouellette S, Todd M. "A systemic approach to corrosion-powered sensor network design." ASME Conference on Smart Materials, Adaptive Structures and Intelligent Systems: 2013.

*Ouellette S, Todd M. "Uncertainty quantification of a corrosion-enabled energy earvester for low-power sensing applications." SPIE San Diego, CA: 2013.

*Ouellette S, Todd M. "Ultra-low power corrosion-enabled sensor node." SPIE San Diego, CA: 2012.

Schlichting A, Ouellette S, Carlson C, Farinholt KM, Park G, Farrar CR. "Multi-source energy harvester to power sensing hardware on rotating structures." SPIE San Diego, CA: 2010.

*Ouellette S, Todd M. "Corrosion-enabled powering approach for structural health monitoring sensor networks". SPIE San Diego, CA: 2009.

FIELDS OF STUDY

Major Field: Structural Engineering

Studies in Structural Dynamics
Professors Michael Todd

Studies in Advanced Structural Behavior
Professor Francesco Lanza di Scalea

Studies in Signal Processing
Professor William Hodgkiss

Studies in Computational Mechanics
Professors Yuri Bazilevs

ABSTRACT OF THE DISSERTATION

Energy Harvesting Paradigms for Autonomously-Powered Sensor Networks

by

Scott Anthony Ouellette

Doctor of Philosophy in Structural Engineering

University of California, San Diego, 2015

Professor Michael Todd, Chair

Within the past 15 years, significant advances in semiconductor integrated circuits (ICs) have reduced power consumption requirements such that mechanisms of transducing various forms of ambient energy for providing autonomous power are a viable technology. The field of energy harvesting has grown immensely as new solutions for developing self-sustaining wireless sensor networks for applications such as structural health monitoring (SHM), precision viticulture, and biometric wearable devices are continually investigated. Due to the wide variety of energy transduction methods and the inherent multidisciplinary nature of energy harvesting, a systematic paradigm for the capture and use of ambient energy is presented. The research outlined in this dissertation covers two energy transduction mechanisms: electrochemical energy

harvesting, and vibration energy harvesting. The first project presented details the modeling, development and testing of a novel cement sea-water battery (C-SWB) and a complimentary low-power sensor node designed for long-term marine infrastructure health monitoring. The second project investigates analytically and experimentally the augmented broadband vibration energy capture of a modulated inertial generator (MIG). Closed-form analytical expressions of interacting electromagnetic dipole moments are derived and used as a nonlinear control parameter to modulate the response of an inertial generator to expand the resonant frequency response spectrum.

Chapter 1
Introduction

In the context of autonomously powered wireless sensor networks, energy harvesting is conventionally described as the process of converting ambient/environmental energy to useful electrical energy. The scale of energy captured by transduction mechanisms is dependent on several environmental factors, as well as the efficiency of the energy transducer. The amount of useful power generated by common energy harvesting devices typically range from the order of micro-Watts (μW) to milli-Watts (mW) when normalizing by volume. This research field has grown as a direct result of advances in wireless technology and low-power electronic devices, as well as a growing interest in embedded wireless sensor networks which contain their own power supply. The conventional power supply for wireless sensors are batteries; however, due to size and weight limitations, commercial batteries often fail to provide enough energy for long-term sensing operations.

Once a battery has been consumed, the sensor must be retrieved and the battery replaced. Because of the remote placement of these devices, accessing the sensor simply to replace the battery can become a hazardous, expensive and tedious, or even impossible, task.

Energy harvesting technologies can potentially satisfy the power demands for a sensor network while simultaneously eliminating costs typically associated with battery replacement and chemical waste. Ideally, there would exist enough ambient energy for an energy harvesting scheme to prolong the lifetime of a power supply (e.g. recharging a battery), or to provide unlimited energy for the intended service life of the electronic device. Given these reasons, interest in energy harvesting research has been rapidly increasing with applications to all types of unattended embedded sensing systems such as: structural health monitoring (SHM), automotive applications (such as regenerative braking), and *in-vivo* bio-mechanical devices. The following sections of this chapter will propose a systemic approach to energy harvesting which considers the entire process of ambient energy conversion to information, and cover each stage of the paradigm in detail.

1.1. Three-Stage Energy Harvesting Paradigm

The proposed systemic energy harvesting paradigm can be parsed into three stages: energy source/transduction (supply), power conditioning and management (storage), and sensing and communications (demand), as shown in Figure 1. Implementation of Stage 1 consists of identifying the sources of ambient energy available and determining the most viable approach for capturing the maximum amount of energy subject to transducer technology, subject to various environmental and economic factors. Since the output power of most energy harvesting transducers is subject to local environmental conditions, the voltage or current is often non-stationary. Therefore, power conditioning and management (Stage 2) is often required for converting the harvested power to a regulated source for low-power sensing and communications telemetry (Stage 3).

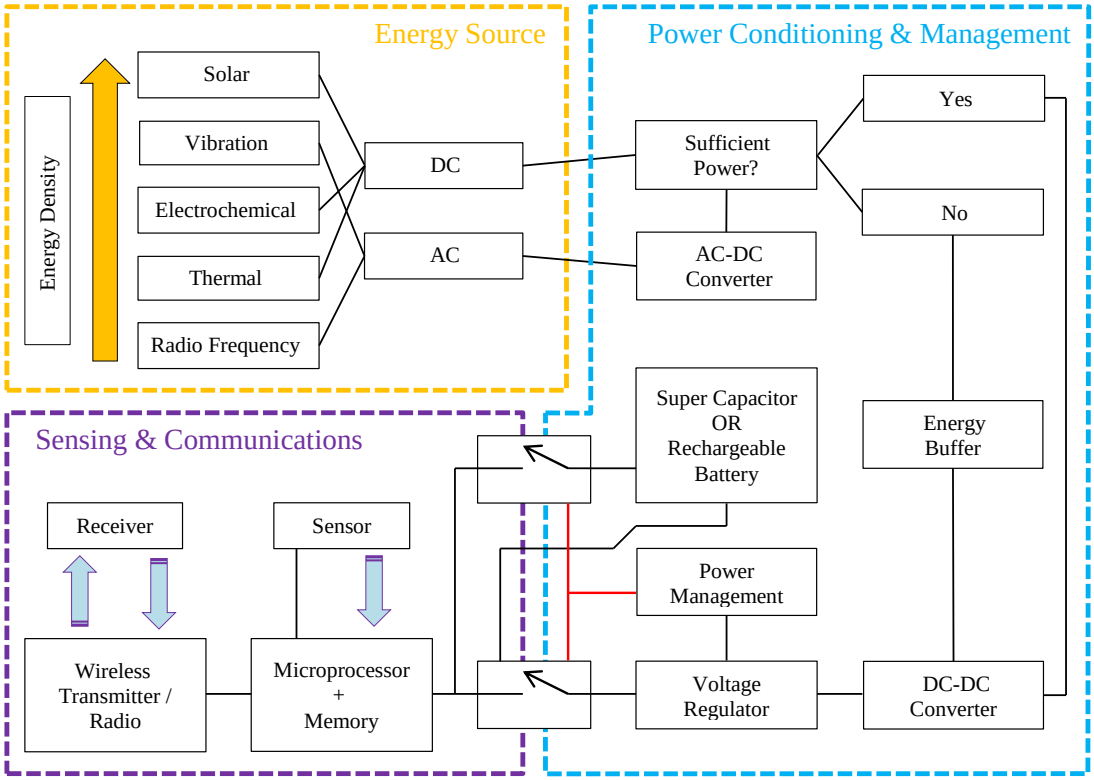

Figure 1. Energy harvesting paradigm

The process involved in Stage 2 begins with assessing the output power characteristics of the energy harvesting device and determining whether or not there exists sufficient power for the latter stage. If the harvested energy is insufficient – as is often the case – then an energy buffer (e.g. a super capacitor) is necessary to acquire enough energy to power communications telemetry. Power management schemes are often used to regulate the flow of energy subject to the sensing protocol specified by the end user. In certain scenarios, the energy harvested can exceed the power demands of the sensing system subject to the duty cycle of the sensor node switching between active mode and idle mode. In this situation, implementing a power management scheme to switch the flow of energy from the sensing and communications

electronics to a rechargeable battery or super capacitor would provide the sensing system a greater level of autonomy under varying environmental conditions.

Lastly, Stage 3 consists of converting the regulated energy into information, and then transmitting the information to a remote server location, often in a wireless modality. Various commercially available low-power sensors exist, as well as low-power microprocessors and radios. This part of the paradigm mainly deals with design considerations of the network topology, number of sensors and type, data acquisition rate and storage, and transmission frequency /duty cycle. With regards to remote, autonomously powered sensor networks, these design parameters play a central role in the selection of a transducer. Therefore, development of an energy harvesting strategy is often an iterative process, and conventionally results in an *ad-hoc* system. In a latter section of this chapter, a detailed description of various network topologies and power consumption metrics will be presented.

1.2. Energy Transduction Methods

The sources of conventionally sourced ambient energies are sunlight, thermal gradients, human motion and body heat, vibration, electrochemical reactions, and RF energy. Several excellent articles reviewing possible energy sources for energy harvesting can be found in references [1]–[7]. Fry et al. [2] provides an overview of portable electric power sources that meet US military special operation requirements. The potential power sources surveyed by the report are thermoelectric generators, mechanical vibration devices such as piezoelectric devices and wind turbines, solar cells, and exotic portable power sources including tapping the laser beam and ambient electromagnetic radiation, as well as traditionally available portable power sources such as batteries and fuel cells. Although the report is concerned only with portable

energy sources for military combat missions, it provides critical insight into future research trends in energy harvesting. For instance, the report defines a list of general attributes intended to suggest what a standard characterization of various portable energy supplies should include. The list includes electrical (energy density, total energy content, power density, maximum voltage and current, RF emission power, electrical interconnects), physical (size/shape, weight), environmental (acoustic emission power, mechanical shock tolerance, electrical shock tolerance, water resistance, operating temperature range), operational (energy requirements for recharging, orientation), maintenance (testing requirements), safety, and disposal requirements. The report also categorizes each energy harvesting scheme by its technical maturity, highlighting those that require considerable development before their feasibility for use in the field can be demonstrated.

Piezoelectric devices have been extensively investigated since the early 2000s, and based on the criteria set in Fry's report are still categorized as still requiring development for field operations. The report concludes with the suggestion that the development of a general standard to address the technical capabilities of energy sources should be pursued in such a way that system designers and integrators are able to assemble components to produce a satisfactory final design. It is still questionable if such design standards currently exist after the tremendous research efforts dedicated to energy harvesting.

Roundy [4] compared the energy density of available and portable energy sources, shown in Table 1. He concluded that for a device whose desired lifetime is in the range of 1 year or less, battery technology alone is sufficient for most field operations. However, if a persistent sensing system requires a longer service life, which is often the case, an energy harvesting scheme is considered a better solution than battery technologies. Paradiso and Starner [7] argued that battery technology has evolved very slowly relative to mobile

computing, in that commercial battery energy densities have increased only by a factor of 3 since 1990. Over the same time period, disk storage density has increased by a factor of 1300, and CPU speed by a factor of nearly 800. They also provide the energy harvesting capabilities of various transduction mechanisms (shown in Table 2), which are slightly different from those suggested by Roundy [4].

Glynne-Jones and White [3], Qidwai et al. [5], and Mateu and Moll [6] also summarize the basic principles and components of energy harvesting techniques, including piezoelectric, electrostatic, magnetic induction, and thermal energy. A common suggestion listed in these articles is the combined use of several energy harvesting strategies in the same device, such that the harvesting capabilities in many different situations and applications can be increased. Furthermore, energy consumption can be minimized in an effort to close the gap between required and harvested energy [6]. For the sake of clarity and completeness, the energy transduction methods listed in Figure 1 will be detailed in a manner that will motivate the following section on power conditioning and management, and highlight the necessity of a systemic paradigm.

Table 1. Comparison of energy sources.

		Power Density ($\mu W/cm^3$) 1 Year Lifetime	Power Density ($\mu W/cm^3$) 10 Year Lifetime	Source of Information
Scavenged Power Sources	Solar (Outdoors)	15,000 – direct sun 150 – cloudy day	15,000 – direct sun 150 – cloudy day	Commonly Available
	Solar (Indoors)	6 – office desk	6 – office desk	Roundy [Error! Bookmark not defined.]
	Vibrations	200	200	Roundy et al. [Error! Bookmark not defined.]
	Acoustic Noise	0.003 @ 75 dB 0.96 @ 100 dB	0.003 @ 75 dB 0.96 @ 100 dB	Theory
	Daily Temp. Variation	10	10	Theory
	Temperature Gradient	15 @ 10°C gradient	15 @ 10°C gradient	Stordeur and Stark 1997 [i]
	Shoe Inserts	330	330	Starner 1996 [Error! Bookmark not defined.]
Energy Reservoirs	Batteries (non-recharg. Lithium)	45	3.5	Commonly Available
	Batteries (rechargeable Lithium)	7	0	Commonly Available
	Fuel Cells (methanol)	280	28	Commonly Available
	Nuclear Isotopes (Uranium)	**6×10^6**	**6×10^5**	Commonly Available

Table 2. Energy harvesting demonstrated capabilities.

Energy Source	Performance
Ambient radio frequency	< 1 $\mu W/cm^2$
Ambient light	100 mW/cm^2 (directed toward bright sun) 100 $\mu W/cm^2$ (illuminated office)
Thermoelectric	60 $\mu W/cm^2$
Vibrational microgenerators	4 $\mu W/cm^3$ (human motion – Hz) 800 $\mu W/cm^3$ (machines – kHz)
Ambient airflow	1 mW/cm^2
Push buttons	50 $\mu J/N$
Hand generators	30 W/kg
Heel strike	7 W potentially available (1 cm deflection at 70 kg per 1 Hz walk)

1.2.1. Solar Energy Transduction

Solar energy harvesting is the process of converting solar radiation (sunlight) into useful electrical energy. This process is conventionally accomplished by means of a photovoltaic (PV) cell, which uses semiconductor materials (or, more recently, organic materials) to absorb photon energy and generate an output electric current. Figure 2a shows a schematic diagram of the conversion process in a PV cell. In order for an electric current to be generated, photons carrying a certain type/amount of energy (band-gap energy) are absorbed into the semiconductor material, whereby weakly bonded electrons are released to a specially designed conduction band – the typical band gap energy for semiconductor materials is in the range of 1-2eV. From there, the electrons collected in the conduction band are free to do electrical work (e.g. power a wireless sensor network). The output voltage of a photovoltaic cell is limited by the band gap energy of the semiconductor material. In order to generate CMOS compliant voltages (and higher), PV cells are connected serially into a PV module.

It is important to note that a PV cell produces zero output power in the absence of band gap compliant solar radiation. An equivalent circuit schematic of a PV cell is shown in Figure 2b. A couple observations regarding the operation of a PV cell can be made from this circuit: 1) the output is an electric current (this implies the cell output voltage is fixed, and that only current fluctuates with time), and 2) the performance largely depends on the diode saturation current (I_D), shunt resistance (R_{SH}), and series resistance (R_S). Current fluctuations aside, the device is best characterized as a DC power source with a very high relative energy density, when compared to other energy harvesting technologies.

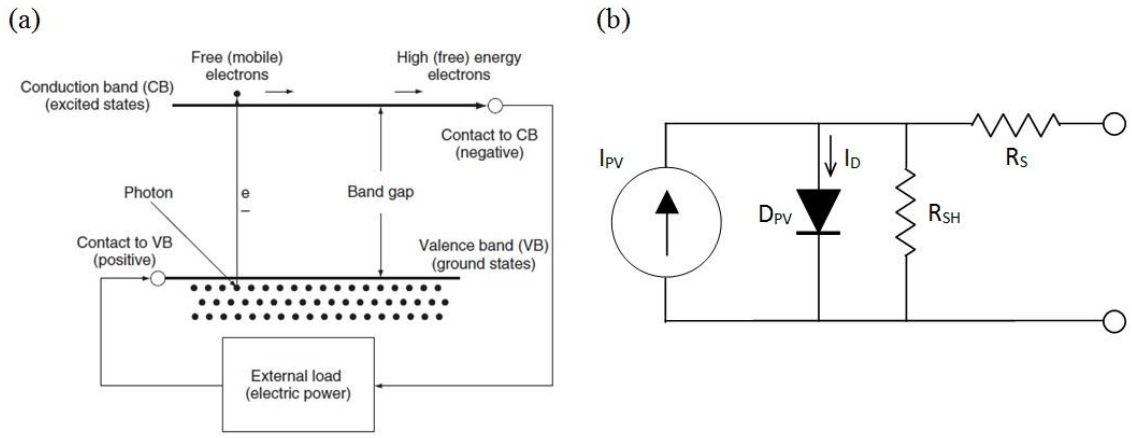

Figure 2. (a) Schematic diagram of PV cell operation, and (b) equivalent circuit diagram of photovoltaic cell

1.2.2. Vibration Energy Transduction

Energy generation from mechanical vibration typically uses ambient vibration around the energy harvesting device as an energy source and then converts it into useful electrical energy. The process of converting mechanical energy to electrical energy occurs either by transduction of elastic strain into electrical energy via the piezoelectric effect [8], or by electromagnetic induction (EMI) using a copper coil and permanent magnet.

Vibration of structural components can result from numerous factors such as flow-induced forces, unbalanced mass in a system, material damage / fatigue, and is an inherent feature of almost every dynamical system. The response of a system to dynamic forces can be primarily characterized by the resonance (natural) frequency, and the rate at which response oscillations decay in the absence of forcing (a.k.a. damping). The conventional model for a vibrating system is a single degree-of-freedom (SDOF / 1DOF) spring-mass-damper lumped parameter model. The most conventional device configuration for vibration energy harvesting is a cantilever beam with a tip-mass subject to base excitation; a piezoelectric system is shown

in Figure 4.2. The general equation of motion for a 1DOF uncoupled energy harvesting system is as follows:

$$M\ddot{x} + C\dot{x} + Kx = -M\ddot{z} \tag{1}$$

where $x = u - z$ is the displacement of the mass relative to the base. Here the parameters (M, C, K) are "lumped" into their equivalent effective magnitudes that contribute to the response dynamics. Equation 4-1 can be rewritten in terms of the damping constant (ζ) and natural frequency (ω_n), where the damping constant is defined as the ratio of the system damping (C) to the critical damping (C_c):

$$\zeta = \frac{C}{C_c} = \frac{C}{2\sqrt{MK}} \tag{2}$$

and the natural frequency is proportional to the ratio of the stiffness to mass:

$$\omega_n = \sqrt{\frac{K}{M}} \tag{3}$$

which results in the equation of motion as a function of the characteristic response parameters:

$$\ddot{x} + 2\zeta\omega_n\dot{x} + \omega_n^2 x = -\ddot{z} \tag{4}$$

In terms of vibration energy harvester design, the left-hand side of Equation 4-2c describes the system response to an applied acceleration($\ddot{z}$), the parameters of which can be tailored to achieve maximal energy output for energy capture. Most types of vibration excitations studied are either harmonic (determinate) or stochastic (random). In either case, the goal of energy harvesting device design is to achieve resonance, the scenario in which the excitation frequency matches the system natural frequency. The result of this scenario is a phenomenon in which the response amplitude can far exceed the input excitation amplitude. For the purposes of vibration energy harvesting, this effect leads to increased energy generation, which ultimately allows for a higher amount of electrical energy for sensing, computation, telemetry, etc.

Depending on the transduction method, either piezoelectric (PZT) or electromagnetic induction (EMI), the manner in which the mechanical energy harvester couples to the electrical circuit changes as a result of the transduction physics, as shown in Figure 3. As such, equivalent circuit models for piezoelectric and electromagnetic energy harvesting schemes have been developed to study the coupled vibration energy harvesting problem, and gain more detailed knowledge on the interaction between the two domains.

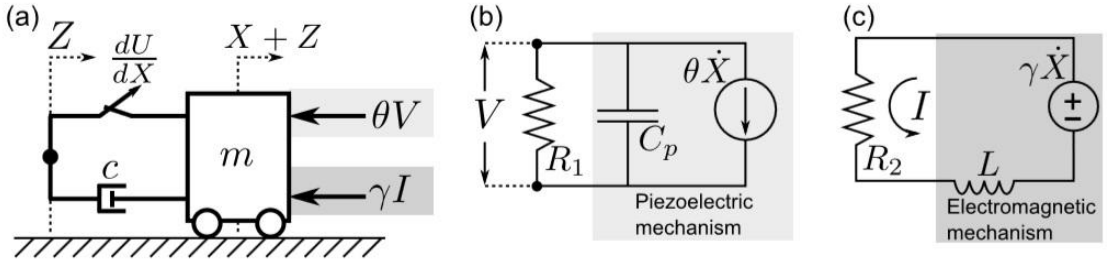

Figure 3. 1DOF lumped-parameter coupled energy harvester with equivalent circuit models for PZT and EMI transduction methods

An important observation on the electromechanical modeling of an energy harvester is that the equation of motion for a device where piezoelectric transducers are used for energy harvesting requires an additional equation to account for the coupling effects, whereas for EMI energy harvesting, the coupling effects can be added to the system damping factor. In more recent years, researchers have pushed to improve vibration energy harvesters by developing methods to capture broadband excitation energy. This report will detail the methods used in a categorical manner by classifying each method based on the design approach.

1.2.3. Electrochemical Energy Transduction

For underwater sensor network applications, the most well-suited energy harvesting techniques fall under the category of electrochemical energy harvesting. These methods generate electrical current from redox reactions that occur naturally as a result of corrosion processes, or organic processes, for example. The fundamental currency of redox reactions is an electron, in that for every single reaction between electrodes (anodes and cathodes) there is a transfer of at least one electron. The two electrochemical energy harvesting techniques presented in this section are seawater batteries (SWBs), and sediment microbial fuel cells (SMFCs). While these techniques share a common chemical process that governs their operation, there are performance characteristics that define them apart from one another.

Electrochemistry is commonly defined as the controlled flow of electrons between two reacting species in a conductive media (electrolyte). This process is chemically defined by redox reactions, in which electrons are removed (oxidized) from one material (anode), and accumulated (reduced) at another (cathode). In order to generate electrical power from this type of reaction, the two reactions must be isolated from one another to avoid chemical equilibrium. The flow of electrons between the two electrodes must then occur via a conductive material, at

which point work can be done (i.e. powering a wireless sensor node). It is conventional to represent the redox reaction as two half-reactions, one for the anode and one for the cathode, in order to show the transfer of electrons more clearly, as the complete reaction is charge neutral. A general expression of the anode half-reaction for a redox process can be represented as:

$$Anode \rightarrow Anode^{n+} + ne^{-} \tag{5}$$

The advantages of the electrochemical energy harvesting methods presented here are that they have a relatively long life-span, require little to no maintenance, and can operate in most underwater environments. Central to the chemical reactions detailed in this section is the abundant presence of oxygen (O_2), which serves as a catalyst for the reduction reaction. The amount of dissolved oxygen available for use in seafloor systems applications decreases drastically in conjunction with depth, and has large variation across the global latitude scale. This scenario largely affects the fuel cell design in that, typically, a large cathode surface area is required. However, with a volumetric increase in fuel cell size, an equivalent decrease in power density occurs.

Seawater batteries are a form of electrochemical energy harvesters that generate electrical power from the process of corrosion. They are aptly named because of the manner in which they function, whereby the device operates on the same chemical process principles that define conventional alkaline battery operation with the electrolyte being seawater. Several environmental parameters affect the operation of seawater batteries, such as water temperature, flow rate, electrode material selection, electrolyte acidity, anode to cathode surface area ratio, and electrode spacing.

The chemical process that defines a seawater battery is referred to as galvanic corrosion. Galvanic corrosion is a special type of electrochemical reaction in which two dissimilar metals are immersed in a common electrolyte and undergo a redox reaction. From an electronics perspective, the parameters (voltage and current) that define a seawater battery are primarily the selected electrode materials based on the Galvanic series, and the equivalent series resistance between the two electrodes. The voltage of a corroding metal is defined as the electrical potential of its half reaction, and is defined relative to a reference electrode, such as saturated calomel or hydrogen. The overall seawater battery voltage is the sum of the individual electrode voltages for a given electrolyte. As a result of the Galvanic series, many seawater battery designs utilize magnesium (Mg) as the anode, and either carbon/graphite (C) or aluminum (Al) as the cathode.

An important aspect to consider in the function of these devices is the removal of reaction by-products that can adversely affect the output power, as well as having access to a fresh supply of oxygen to drive the corrosion reaction. These criteria can be accommodated in underwater, or water surface, applications with sufficient flow rates such that the shear force of the water removes the magnesium hydroxide from the surface of the magnesium anode. It should be noted that seawater is not a source that is abundant with oxygen, which, in cases of underwater sensor nodes, requires the carbon cathode to have a large surface area. This observation is more prevalent in the context of the chemical reactions, as will be explained below. Equation 6 below shows the half reaction for the magnesium anode in the presence of a corrosive electrolyte.

$$Mg \rightarrow Mg^{2+} + 2e^{-} \tag{6}$$

Here, the magnesium releases two of its valence shell electrons, which then traverse through the external conductive path (circuit) to the cathode. Assuming there are no metallic ions present in the electrolyte, the electrolyte is either neutral or basic, and oxygen is present, then the reduction reaction consists of oxygen and water molecules combining to form hydroxyl ions [9], as shown below in equation 7.

$$O_2 + 2H_2O + 4e^- \rightarrow 4OH^- \tag{7}$$

This is most commonly the case with carbon-anode seawater batteries, as the carbon is noble to the point of being chemically inert in this reaction. In this capacity, it is highly useful for accumulating oxygen at its surface, and for its highly conductive properties. The secondary reactions result in an insoluble precipitate on the magnesium surface, and a calcareous deposit on the cathode surface, as shown in equations 8a and 8b.

$$Mg^{2+} + 2OH^- \rightarrow 2Mg(OH)_2 \tag{8a}$$

$$4Ca^{2+} + 4HCO_3^- + OH^- \rightarrow 4CaCO_3 + H_2O \tag{8b}$$

For both secondary reactions, the resulting effect reduces the active surface area of the electrodes, which adversely affects the battery performance [10]–[12].

Another novel approach to electrochemical energy harvesting comes from exploiting redox reactions from organic microbial activity found in sediment. The energy harvester design

uses conductive inert materials, such as carbon/graphite, or stainless steel, to accumulate microbes in sediment (anode) and reduce oxygen in water (cathode). As opposed to seawater batteries, SMFCs do not require a salt water electrolyte for operation. Typically, organic microbes present in the sediment are oxidized at the sediment-electrode interface. The set of reactions that take place produce both protons, either via ionized hydrogen sulfide or organic carbon, and electrons. The oxidation half-reaction at the anode are shown below in equations 9a and 9b.

$$[organic\ microbe] - C + H_2O \rightarrow CO_2 + H^+ + e^- \quad (9a)$$

$$HS^- \rightarrow S + H^+ + e^- \quad (9b)$$

As with the seawater batteries, the electrons are transferred from the anode to the cathode through an external conductive wire. The cathode reaction is once again a reduction of oxygen to form hydroxyl ions or water, depending on the sediment composition. The reduction half-reaction expressions are shown below in equations 10a and 10b [13]–[15].

$$O_2 + 4H^+ + 4e^- \rightarrow 2H_2O \quad (10a)$$

$$O_2 + 2H^+ + 2e^- \rightarrow 2OH^- \quad (10b)$$

A unique aspect of SMFCs is that the lifetime of their power generation is relatively unbounded due to the fact that natural sedimentation processes continually renew the organic microbes present at the anode surface. Furthermore, since the electrodes are typically

comprised of chemically inert materials, their operational lifetime is not a system limitation. The main limitations with SMFCs deal with their low power generation, mostly resulting from low output voltage [16]. As we will show in Chapter 3 of this dissertation, low power generation is not prohibitive in developing remote sensing systems as it is a fairly ubiquitous feature amongst energy harvesting technologies, with many clever electronics solutions, such as power management systems, already existing.

Another potentially limiting feature is the nonlinear scaling between power generation and electrode surface area. In essence, the power density of a SMFC is inversely proportional to the electrode size, rendering large scale harvesting systems cost ineffective. In regards to remote sensing systems, this nonlinear scaling is not too much of an issue. In reality, the nonlinear scaling merely eliminates the SMFC technique from acting as a grid-scale power generation tool.

1.2.4. Thermoelectric Energy Transduction

A thermoelectric energy generator (TEG) is a device that produces electrical energy from thermal gradients. These devices are often deployed in situations where large differences in heat occur over a short distance, or at a material interface such as soil and water, air and water, etc. The governing process that defines the operation of a thermoelectric generator is described the by the Seebeck effect in which electrical current is generated when the junction of two dissimilar metals are subject to a temperature gradient. Using this principle, numerous p-type and n-type junctions are connected electrically in series and thermally in parallel to construct a TEG. The series connection of the electrical network is used to generate a higher output voltage, whereas the parallel thermal connection is required to expose the elements to the same temperature gradient. Thus, when an electrical current is applied to the TEG a thermal

gradient is generated, allowing the device to function as a small solid-state heat pump. The inverse operation is also possible, in which a thermal gradient is applied to the device to generate an electrical current that can be utilized to power other electronics. When a thermal gradient is applied across the n-type and p-type thermocouples, charge carrying electrons and holes move in opposite directions polarizing the opposite ends of the module.

The conventional metric for evaluating the performance of a TEG is the figure of merit (ZT), which determines the maximum efficiency of a TEG module as a function of thermal gradient (T_h - T_c), thermal conductivity (λ), electrical conductivity (σ), and the Seebeck coefficient (S) which describes the properties of a thermoelectric material where electrons carry both electricity and heat. The equation that relates the terms listed is shown below in equation 11:

$$ZT = \frac{\sigma S^2}{\lambda}\left(\frac{T_h - T_c}{2}\right) \tag{11}$$

The figure of merit for a TEG module is largely an average of the component materials' figure of merit (zT) values. Silva et al. [17] performed as study on thin-film thermoelectric modules, and charted the progress made by researchers looking to improve the figure of merit, as shown below in Figure 4.

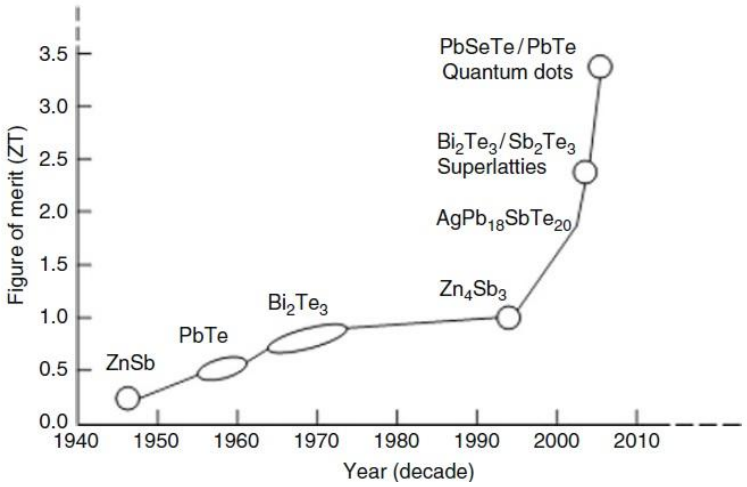

Figure 4. Progress in improving TEG figure of merit

Overall, the efficiency of a thermoelectric device is expressed as a function of the figure of merit, and is scaled by the Carnot thermodynamic efficiency (the same scaling efficiency that limits photovoltaic cells) [18]. The expression for the efficiency of a thermoelectric device is as follows in equation 12:

$$\eta = \frac{\Delta T}{T_h}\left(\frac{\sqrt{1+ZT}-1}{\sqrt{1+ZT}+\frac{T_c}{T_h}}\right) \tag{12}$$

The TEG is a mature technology and a reliable energy converter with no moving parts compared to vibration-based harvesters. The TEG has been actively studied for the last three decades and the literature in this area is extensive. One of the drawbacks of this technology is low efficiency (<8%) if there is a small temperature gradient present. Further, the fabrication cost is high, and the volume and weight are still too large for micro-scale sensing systems.

1.2.5. Radio Frequency Energy Transduction

Another way of supplying power to sensor networks is that of wireless energy transmission. This field of research experienced rapid growth in the early 1990s with the advent of RFID applications. In this case, power is generated elsewhere and transmitted to a sensor node by some form of electromagnetic wave or RF radiation. The frequency range of primary interest in RF energy harvesting applications exists within the ISM band of 900 MHz – 5.8GHz. Previous studies showed that electronics can be used to efficiently capture ambient radiation sources and convert them to useful electricity. In general, an RF energy harvesting-enabled sensor node can be characterized by three parameters, shown pictorially in Figure 5:

1. RF source: ambient or controlled, and power density from source
2. RF propagation channel: free space, indoors, and line-of-sight
3. Rectenna: antenna resonant frequency, rectifier efficiency, DC-DC converter efficiency, and impedance matching
4.

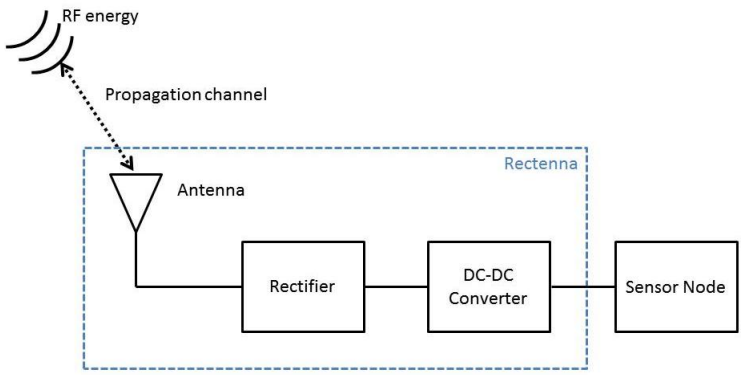

Figure 5. Generic RF energy harvesting paradigm

In this section, we will define ambient RF as having emanated from a singular (or in some cases multiple) omnidirectional transmitter, whereas a focused, or controlled, RF source is often from a directional transmitter (i.e. a Yagi antenna). In a recent paper for the Proceedings of IEEE, Visser and Vullers [19] defined the accumulation of energy from an ambient RF source as "RF energy harvesting", whereas extracting energy from a dedicated source is referred to as "RF energy transport". The distinction between the two methods has a direct effect on the sensor node energy capture and conditioning electronics, such as the area of the RF energy harvesting antenna. For applications of ambient energy harvesting, the primary RF energy sources are cellular phone communication base stations (GSM900, LTE, etc.), and Wifi routers. These sources are ubiquitous in an urban environment, and, due to their operating frequencies, allow for receiver antennas on the order of 10-50 cm^2. A study of the power density supplied by GSM base stations across Europe was performed by Visser et al. [20], and they found the mean power density measured at a range of 25 – 100 m to be between 0.01 and 1.0 mW/m^2. Based on the results, they concluded that ambient RF energy harvesting is insufficient for powering sensing applications which require smaller form factors.

For situations where size limitations govern the sensor node design, RF energy transport methods are the preferred method for delivering wireless energy over short distances. Since this method requires a dedicated RF transmitter antenna, the choice of transmission frequency is an important factor. Other factors to contend with are the limitations on transmission power and exposure time set by regulatory commissions, such as the FCC and the International Commission on Non-Ionizing Radiation Protection (ICNIRP) [21]. Visser and Vullers summarized the frequency band allocations and transmit power restrictions for RF energy transport systems, using the following table.

Once an electromagnetic wave is transmitted, the amount of electrical power received at the sensor node is determined in large part by the propagation channel. A well-known expression for the received power through free-space transmission is described by the Friis transmission equation:

$$\frac{P_R}{P_T} = G_T G_R \left(\frac{\lambda}{4\pi r}\right)^2 \tag{13}$$

where, P_R is the received power, P_T is the transmitted power, G_T is the transmitter gain, G_R is the receiver gain, λ is the transmission wavelength, and r is the separation distance between the two antennas. A common representation for describing the effect of the propagation channel is by expressing the power attenuated by the transmission path (i.e. the path loss). A general expression for the path loss is provided by Visser and Vullers [19], and is shown below in Equation 14:

$$P_L(dB) = 20\log\left(\frac{4\pi r_o}{\lambda}\right) + 10n\log\left(\frac{r}{r_o}\right) \tag{14}$$

where, r_o is a reference distance, and n is a constant value pertaining to the propagation channel. The values for n are most typically within the range of 2 for indoor environments without line-of-sight corruption. In essence, the amount of energy available for use by the sensor node is highly influenced by environmental parameters, antenna design and spacing, and transmission signal characteristics.

When considering the RF energy harvesting paradigm as an energy conversion system, such as in Figure 8.1, further losses to the power available to the sensor node are incurred within the rectenna. As stated before, a rectenna is conventionally comprised of three main components: an antenna, a rectifier, and a DC-DC converter. Special care is given to each component in order to ensure optimal operational efficiency so as to maximize the amount of energy available for the sensor node and or to recharge a battery. Parasitic losses due to imperfect RF to DC conversion efficiency in the rectifier, as well as an impedance mismatch between the rectifier and DC-DC converter are an inevitable characteristic of the system.

Starting with the antenna, it is important to first determine the space available for the intended application, as this will inevitably place restrictions on the antenna geometry. Next, the optimal geometry must be chosen, in particular, one with enough features that can allow for tuning the input impedance at the operating resonant frequency. The antenna characteristics must then be approximated either by means of an analytical or numerical model, or by commercial software simulation. Once the antenna design is verified to operate in an acceptable manner, with minimal losses, the rectifying circuit and DC-DC converter are then designed, with careful consideration given to matching the input and output impedances between each stage – the details of these procedures will be covered in Part III. With regards to the rectifying circuit for RF energy harvesting applications, the component that has the greatest effect on the impedance is the diode, which most commonly is a Schottky diode.

In the next section, a cursory review of power conditioning and management electronics is presented, with special regards to applications in energy harvesting and wireless sensor network topologies.

1.3. Power Conditioning Electronics

As shown in the energy harvesting paradigm depicted in Figure 1, each energy transduction method produces a unique electrical signal in terms of voltage and current. In order to develop a robust autonomously-powered sensor system, it is imperative that the designer implements a power conditioning and management strategy to account for the needs of the sensing and telemetry electronics under environmental and operational variations.

The majority of energy harvesting transduction methods generate a DC signal; however, in the cases of vibration and RF energy harvesting, an AC-DC converter will be required. While there have been several research initiatives focused on the optimal method AC-DC conversion, the most conventional approach is to use a full-wave diode bridge with a filter capacitor. The resulting DC signal now must be assessed under a variety of operational scenarios to determine if the output power is sufficient to directly supply the sensing and telemetry electronics.

For the majority of energy transduction technologies, an energy buffer is required to store and release the captured energy in such a way that the sensor node microcontroller (MCU) and transmission radio can operate. Energy buffers typically consist of either an electrolytic supercapacitor (low energy density, high rate of charge/discharge), or rechargeable batteries (high energy density, low rate of charge/discharge). For the buffering approach to work, an isolation switch is required to prevent the sensing telemetry from continuously discharging the stored energy.

The primary goal of the power conditioning and management circuitry is to provide the sensing telemetry with a regulated supply of power for reliable operation. For CMOS integrated circuits, this regulated supply voltage is typically within the range of 2.2 – 3.6 VDC. As such, given the mostly non-stationary nature of ambient energy capture, a DC-DC converter is

recommended for dynamically regulating the supply voltage to specific levels set for the electrical load (sensing telemetry). There are various forms of DC-DC converters that serve multiple operational functions with varying degrees of conversion efficiency; however, most commercial off-the-shelf CMOS integrated circuit (IC) converters can operate at efficiency levels above 90%. Furthermore, with built-in error amplifiers and feedback current sensing, these ICs are able to provide a closed-loop output voltage regulated supply to an electric load for a wide range of dynamic input voltages.

A natural consequence of the periodic nature of ambient energy capture are the potential phase issues with the measurement acquisition and transmission schedule. A parasitic and dynamic power management strategy is essential to account for operational variability inherent to autonomous system design. These systems often consist of an independent low-power MCU that is programmed to track and manage the operational states of a sensor node (active mode, and idle mode) in order to minimize total energy consumption. In most cases, power management ICs feature an algorithm designed to sample sensor node cycles, power consumption, and energy generation and storage levels to optimize usage. In essence, the function of power management circuitry is to intelligently control the flow of energy and to store any excess energy generation (e.g. trickle-charging a rechargeable battery) for use in scenarios where the ambient energy is not present for consumption.

The following section in Chapter 1 provides information on various sensor network paradigms with regards to their operational environment, and motivation for implementing energy harvesting strategies for providing autonomous power to persistent surveillance systems.

1.4. Sensing and Communications Telemetry

In the realm of information collection and sharing, there are two common types of sensor network paradigms: wired and wireless. Since the energy harvesting schemes presented in this dissertation are developed for the application of remote sensing operations, the focus of this section will be on wireless sensor network (WSN) paradigms, applications, and open research issues in the field. The manner in which sensor nodes are deployed, communicate, and how long they operate (assuming their power supply is a battery) depends on their environmental deployment. For simplicity, WSNs in this report will be defined into three categories of sensor operation: terrestrial (ground) sensors, floating sensors, and underwater sensors. Wireless sensor networks have been demonstrated to be useful for a variety of applications in scenarios like target tracking (military) and surveillance, hazardous environment exploration, seismic sensing, and structural health monitoring [22]–[27]. A graphical representation of sensor network applications reported in the literature has been provided by Yick et al. [28], and is shown below in Figure 6. In essence, a wireless sensor network is implemented to perform two types of tasks: monitoring and/or tracking. The information presented in this section is intended to serve as a high-level overview of WSN topologies, applications, and known issues. For a more detailed survey of WSN research, refer to Yick et al. [28], as well as several more recent surveys [29]–[33].

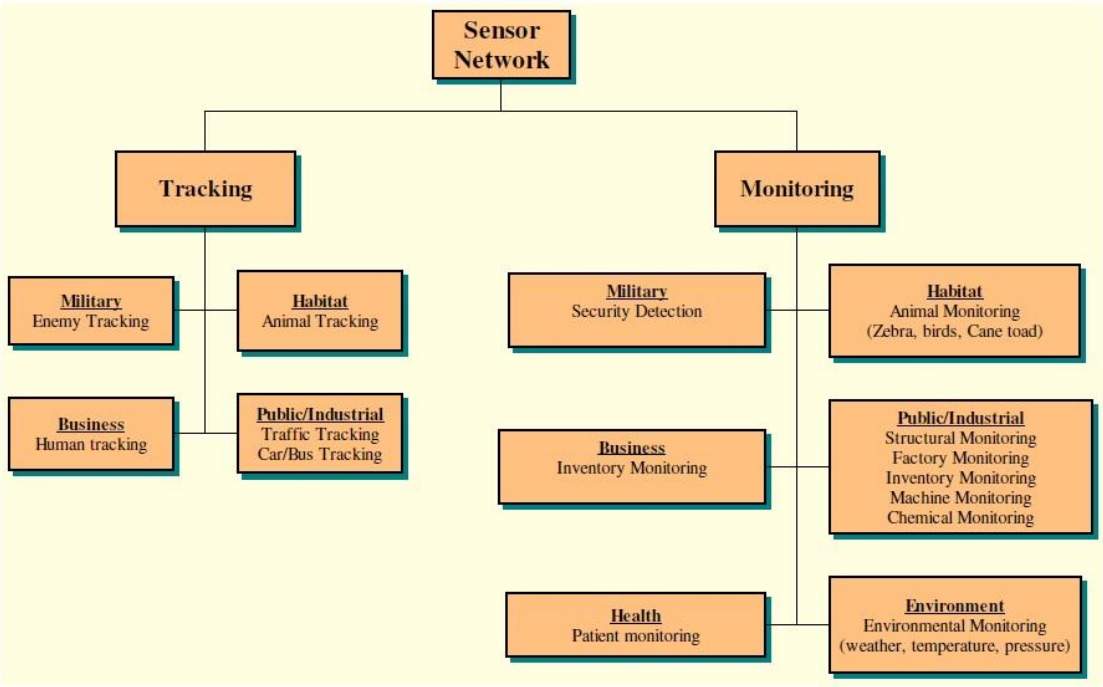

Figure 6. An overview of sensor network applications

It is important to note that there are other forms of WSNs reported in the literature, such as underground sensor networks, and mobile sensor networks. Attention to specific research applications of these network types will be highlighted based on the unique monitoring approaches taken.

A wireless sensor network is typically a collection of sensor nodes, ranging from tens to thousands, working in concert to obtain environmental data over a defined region. In this manner, there are two types of WSNs: unstructured and structured. An unstructured WSN contains a dense array of sensor nodes deployed in an *ad hoc* manner, whereas a structured WSN places sensor nodes in a uniform, grid-like manner, thus requiring fewer nodes to cover a defined region. Wireless sensor networks are limited by numerous design and resource constraints, such as finite power supply (energy harvesting is a potential solution here), short communication range, and limited data storage and processing. Design constraints are

dependent on the environment in which the WSN is deployed, network size, deployment scheme (structured or unstructured), and communication protocol / network topology. A major concern in the design process of a WSN is the sensitivity of wireless communications to physical obstructions, which can further reduce the communication range between nodes, or completely block all data transmission.

For ground-based (terrestrial) WSNs, the ability to communicate in a dense environment is essential. Energy conservation can be achieved at the individual node level by implementing a multi-hop data routing scheme, reducing the communication range, optimizing data transmission in terms of unique information packets and message frequency, and using low duty-cycle operations. Werner-Allen et al. [34] deployed a terrestrial WSN for monitoring a volcano in Ecuador using seismic and infrasonic sensors. In their study, they found the weak-link in the system was the finite battery life; the issue being the need for continuous sensor node operation to monitor seismic events that normally preempts a volcanic eruption.

Underwater sensor networks require a different communication protocol, as well as routing scheme, and, as such, underwater sensors are more expensive and fewer in number [35], [36]. The typical configuration consists of an autonomous underwater vehicle that interrogates data from fixed sensor nodes. A unique aspect of underwater sensor networks is that they communicate wirelessly via acoustic transmission. This communication protocol exhibits low bandwidth, significant propagation delay, high signal attenuation, and requires more power than radio communication. Furthermore, the ocean environment is particularly harsh on commercial electronic devices. This unavoidable consequence means that underwater sensor networks must be self-configurable in order to adapt to scenarios where a node (or several nodes) fail. Mijarez et al. [37] developed an underwater sensor network for flood detection monitoring in hollow sub-sea structural members on off-shore oil rigs. Their paper investigated the use of underwater

acoustic transmission, as well as ultrasonic guided wave transmission (using the steel structure to transmit sensor data) to transmit sensor data to an above-water base station. Despite a low signal-to-noise ratio for both communication approaches, the system was demonstrated to work effectively for the desired monitoring need.

Floating sensor networks, while also having to operate in harsh environments, have the benefit of using radio communication protocols for data transmission. The floating sensor nodes are mostly placed in a structured grid in order to allow for energy-conserving communication algorithms to be used. Floating sensors are most commonly mounted to a buoy, and are used for weather monitoring, surface wave monitoring, ship navigation, and various military applications like remote sonar [38]–[40].

A novel wireless sensor network that is designed for post-disaster assessment of civil infrastructure was proposed by Mascareñas et al. [41], whereby a roving mobile host would deliver microwave energy to passive displacement sensors on a bridge to wirelessly interrogate the sensor node. A diagram of the system is shown below in Figure 7

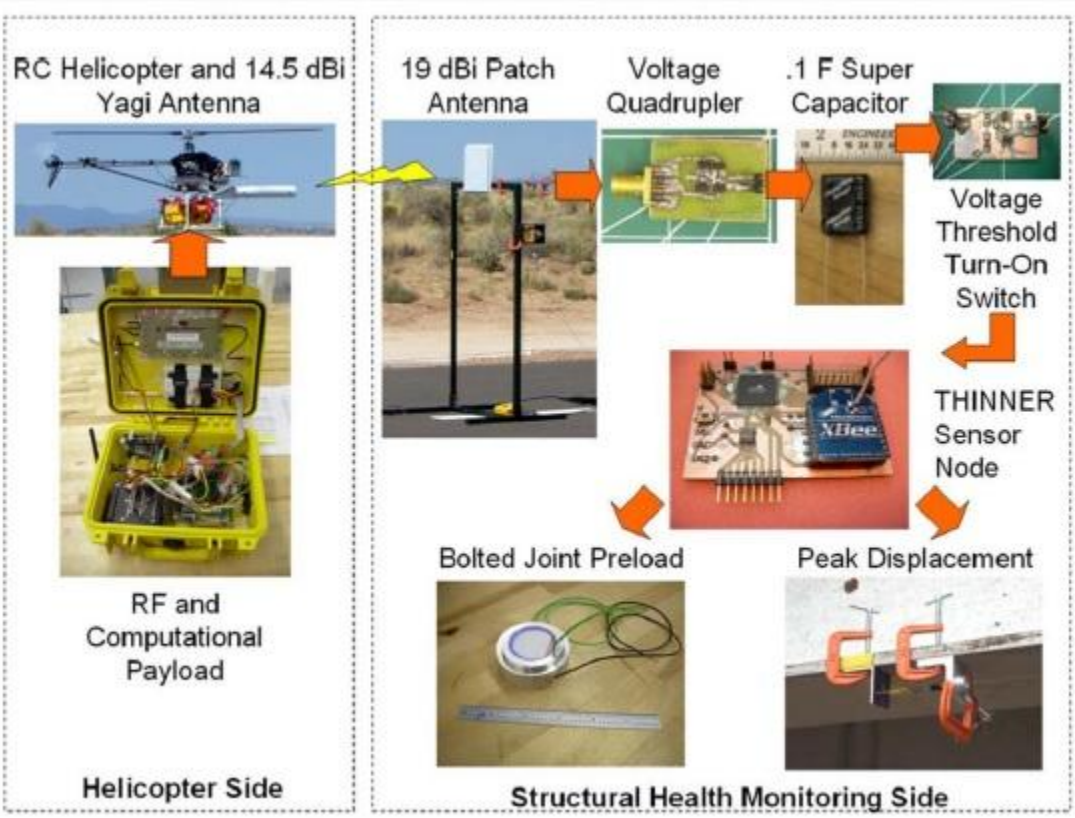

Figure 7. Diagram of roving mobile host sensor network paradigm

A significant effort was put forth in this system to develop a passive sensor node (THINNER) that could collect data in the absence of electrical power. This was accomplished with the use of a capacitance-to-digital converter in concert with an ATmega128L microcontroller. The mobile host used was a commercially available radio-controlled helicopter equipped with a 2.5GHz, 14.5dBi Yagi antenna for wireless energy delivery. The host would be piloted to close proximity of a patch antenna connected to the THINNER sensor node, and would commence wireless energy delivery. Once enough energy was collected on a charge capacitor on the THINNER sensor node, the ATmega controller would wake up and transmit the stored displacement data back to the mobile host via a ZigBee radio. Experimental field

tests successfully demonstrated the ability of the system to deliver energy and receive a return packet of information, even if the total charge time was prolonged due to flight control issues.

Embedded system design is characterized by a tradeoff between a need for good performance and low power consumption. Proliferation of wireless sensing devices has stressed even more the need for energy minimization as battery capacity has improved very slowly (by a factor of 2 to 4 over the last 30 years), while computational demands have drastically increased over the same time frame, as shown in Figure 8.

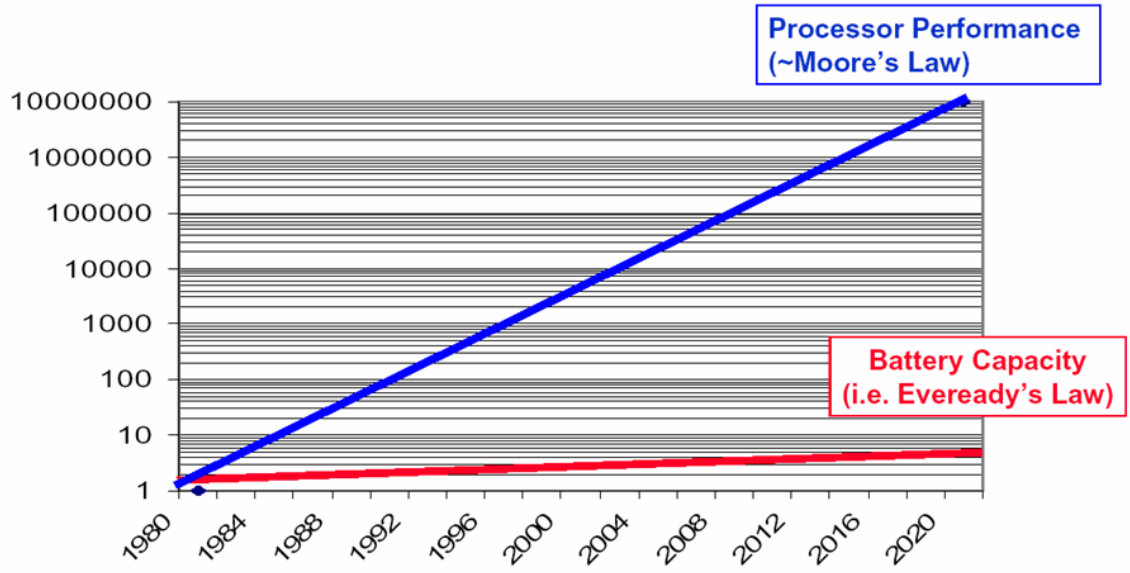

Figure 8. Battery capacity vs. processor performance

Since the introduction of wireless computing, the demands on battery lifetime have grown even more. In fact, in most of today's embedded sensing devices, the wireless connectivity consumes a large fraction of the overall energy consumption. Figure 9 shows a power consumption breakdown for a small sensor node (top of the figure) and a larger

embedded device based on a Strong ARM processor (200 MHz) coupled with a wireless local area network (WLAN) for communication. On small sensor nodes, as much as 90% of the overall system power consumption can go to wireless communication, while on the larger devices, such as the one shown at the bottom of Figure 9, the wireless takes approximately 50% of the overall power budget. In both cases, the second most power-hungry device is the processor. Therefore, in order to achieve long battery lifetimes, optimization of both computing and communication energy consumption is critically important.

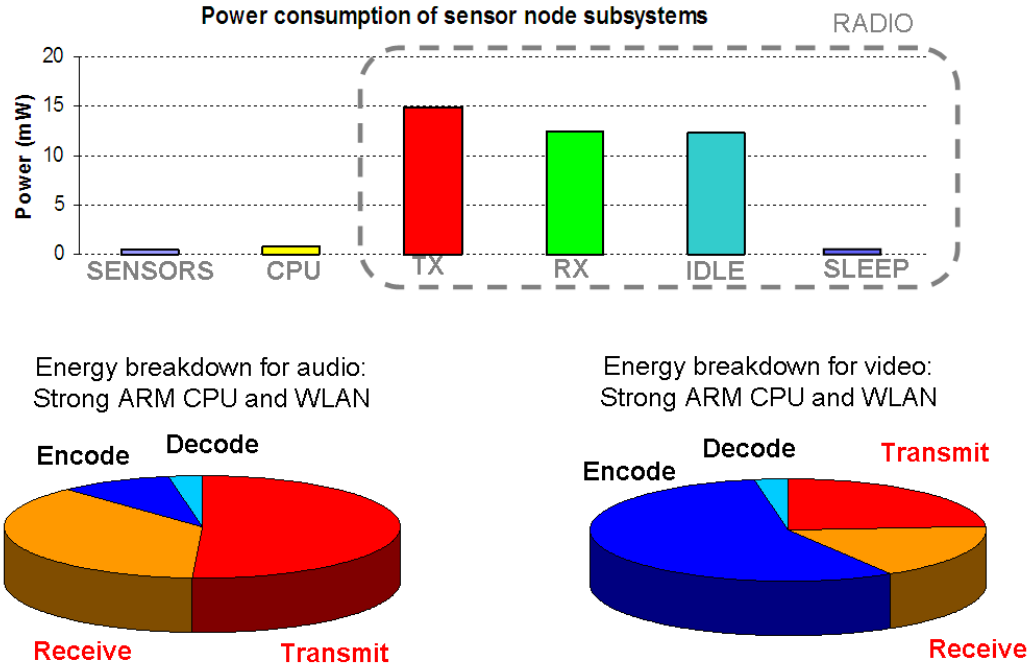

Figure 9. Power consumption of two different embedded system designs

Better low-power circuit design techniques have helped to lower the power consumption. On the other hand, managing power dissipation at higher levels can considerably decrease energy requirements and thus increase battery lifetime and lower packaging and

cooling costs. Two different approaches for lowering the power consumption at the system level have been proposed: dynamic voltage scaling, primarily targeted at the processing elements, and dynamic power management, which can be applied to all system components.

A portion of this chapter is to be submitted as a technical report for Los Alamos National Laboratory, Scott Ouellette, Charles Farrar, and Michael Todd, 2015. The title of this report is "Energy Harvesting for Autonomous Sensor Networks." The dissertation author was the primary investigator and author of this paper.

Table 3. List of remote sensors and power requirements.

Category	Applications	Types of sensors	Parameter measured	Power requirements (mW)
Underwater sensors [15], [36], [37], [42]–[48]	Habitat monitoring	Ultrasonic, pressure, vibration, acoustic, infrared	Tracking numbers, distribution	6000, 10
	Monitor equipment and structure	Ultrasonic and piezoelectric	Cracks in structure	--
	Military surveillance	Acoustic vibration	Intruder	28
	Environmental applications	Electrochemical, thermocouple, oxygen, conductivity, fluorescence, seismic	Trace chemicals, pH, salinity, temperature, pressure, conductivity, oxygen, fluorescence, phosphate, turbidity	50—450
Ground sensors [27], [34], [49]–[56]	Weather monitoring	Thermocouple, thermistors, electrochemical, electromechanical	Temperature, pressure, humidity, radiation	1—50
	Military surveillance	Infrared, magnetometer, acoustic, vibration	Intruder	420—6000
	Volcano monitoring	Seismic, acoustic and infrasonic	Seismic wave	10,000
	Habitat monitoring	Infrared, thermocouple, barometric, ultrasonic, capacitive, photo-resistance, vibration, acoustic	Occupancy, intruder, temperature, pressure, humidity, sound	1—6000
	Environmental applications	Electrochemical, thermocouple	Trace chemicals, temperature	0.01, 0.025
	Agricultural monitoring	Thermocouple, electrochemical, actuator	Temperature, soil moisture content, pH, conductivity	0.01—50
Floating sensors [40], [57]–[60]	Weather monitoring (weather buoy)	Anemometer, rain gauge, thermocouple, electrochemical, electromechanical, barometric, optical	Temperature, pressure, humidity, rain, salinity, wind speed	50
	Environmental applications	Electrochemical, meteorological, oceanographic, acoustical	Trace chemicals, color, ocean processes	5.4—85,000
	Underwater surveillance	Acoustic, magnetic, radiation	Intruder, ocean processes	5.4—85,000

Chapter 2

Corrosion-based Energy Harvesting

2.1. Introduction to Electrochemistry and Galvanic Corrosion

In 2002, corrosion damage to the U.S. industry had an estimated annual cost of $137.9 billion, with the U.S. infrastructure cost being 16.4% ($22.6 billion). Further analysis shows that, of the five categories of infrastructure studied, highway bridges account for 37% ($8.3 billion) of the estimated annual cost, while waterways and ports are roughly 1% ($300 million) [61].

Currently, U.S. highway bridges, dams, waterways, and ports are routinely inspected using mostly the visual inspection (VI) technique [62], [63]. However, the VI technique fails to provide sufficient information on incipient corrosion damage to reinforcing steel, and, as such, there have been developments towards embedded sensing of reinforcing steel rebar corrosion by proactively interrogating for regions of chloride concentration [64], [65]. Since corrosion is an electrochemical process, there are methods to exploit the potential difference relative to a reference cell (e.g. copper – copper sulfate) as a means of detection [66]. This method assumes

the system impedance to have a fundamental frequency dependence that is revealed via Nyquist plot when excited with a chirp signal.

For most active sensing systems employed in structural health monitoring applications, the conventional power supply is a battery (e.g. NiCd, NiMH, etc.). However, all conventional battery designs have a finite power capacity, and most embedded sensing applications render battery replacement in the deployed state prohibitively difficult [67]. Furthermore, there exists a trade-off between power demands and damage feature detection and localization when considering active versus passive sensing of corrosion in infrastructure health monitoring. One possible solution to this problem is to utilize the failure mechanism (corrosion) as the source of power for deploying a sensing strategy.

Corrosion has, on several occasions, been shown to be a viable source of energy for powering sensing and control systems [10]–[12]. Previous initiatives employing magnesium anodes oxidized in seawater, for a Galvanic series corrosion process, have shown to be suitable for powering deep-sea systems, such as oil wells [68], and geophysical observation devices [47] for long-term operations. Though operating deep beneath the water surface reduces the potential for bio-fouling, it also reduces the concentration of oxygen available for the reduction reaction – requiring the battery design to have an open structure to ensure the unabated access to fresh seawater. Serially connected multi-cell designs are prone to current leakage between electrodes, resulting in inter-cell corrosion, housing corrosion, and eventually battery failure. Due to the power demands of the submerged devices (15-25 W) for operational periods spanning multiple years. As such, a DC-DC converter, and, sometimes, a secondary battery are required for the single cell design. Other researchers have used the corrosion of reinforcing steel in concrete structures as the working electrode for powering custom corrosion sensors embedded in the concrete slab [69]–[71].

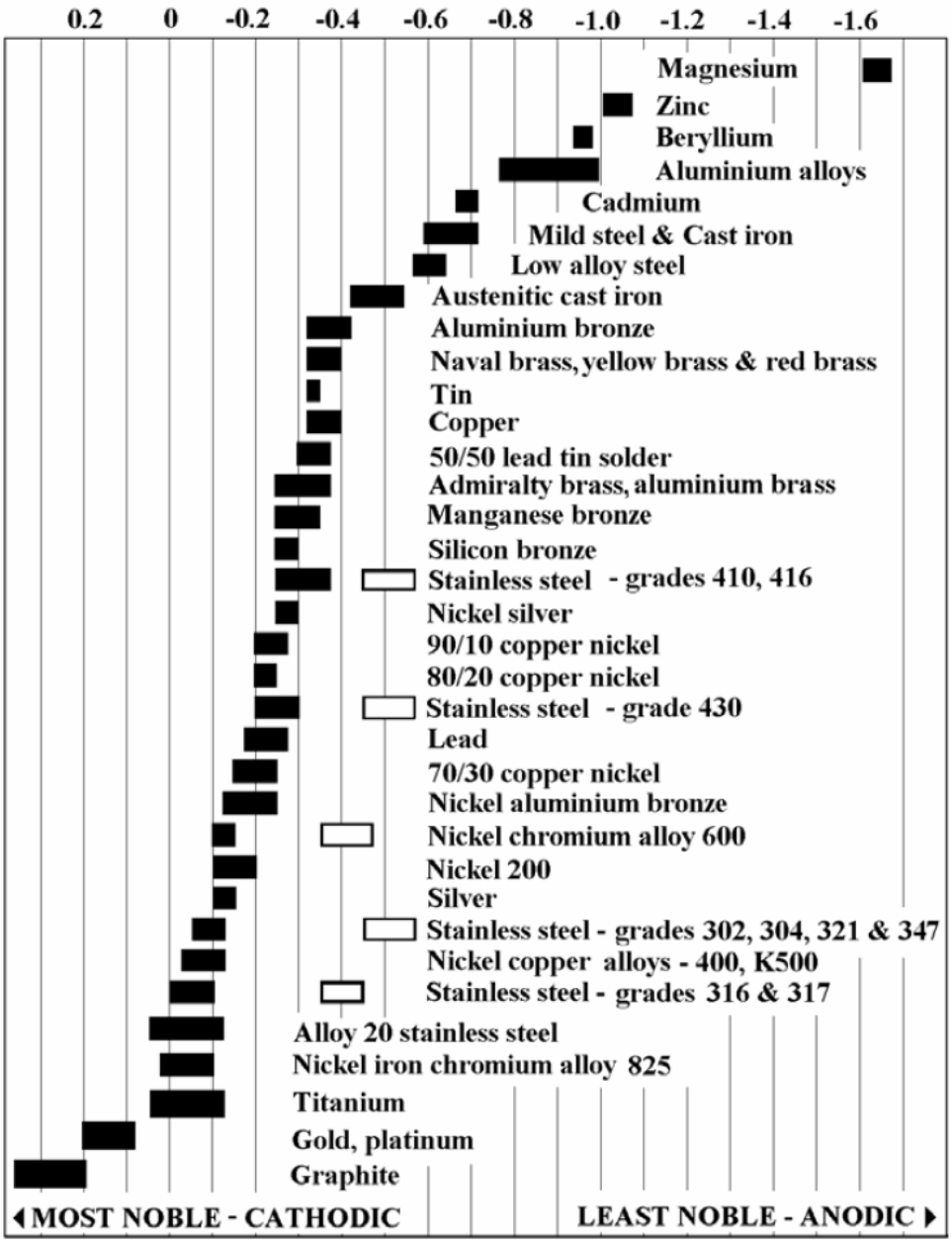

Figure 10. Galvanic series chart for various transition metals

This chapter details the use of cement to limit, in a passive manner, the amount of consumable oxygen for shallow-depth, low-power generation applications in monitoring marine infrastructure subject to corrosive attack. The following sections will describe in detail the

design and corrosion chemistry of the Galvanic series cement seawater battery (C-SWB). Two battery specimens were fabricated and placed in a seawater bath for a period of two weeks. For the duration of the experiment, the specimens were tested continuously to observe the evolution of the power output. An equivalent circuit model of the cement seawater battery is verified and used in the design of the power condition circuit in Chapter 3.

The concept for the cement battery was inspired by the need to monitor the health of reinforced concrete marine structures (e.g. bridges, piers, ports, etc.), in which one of the main damage modes of marine structures is due to the corrosion of steel. Steel corrosion is the process in which iron atoms are purged from the material surface by an electrochemical reaction, and subsequently dissolved into the surrounding electrolyte solution. In the case of reinforcing steel in concrete, the corrosion process only occurs at instances where pores meet the steel surface. The chemical reaction requires the transfer of electrons from the anode site (where the steel is losing mass) to the cathode site. These reactions occur simultaneously and are referred to as a redox reaction. Steel molecules at the anode site are oxidized (loses electrons) by the solution, and another location on the surface is reduced (cathode site). The corrosion process itself is electrochemical, and therefore can be exploited for electrical energy, as there is a transfer of electrons (current) as well as an activation voltage (i.e., the electromotive force).

2.2. Design of Cement Sea-Water Battery

The following sections will detail the various design considerations for the C-SWB energy harvester. Of particular significance in regards to the harvester design are the chemical

process model, equivalent electrical circuit model (which be used to estimate the output power that can be delivered to an electrical load), and the overall capacity and operational lifetime.

2.2.1. Chemical Process Model

The cement battery operates via Galvanic corrosion, in which two dissimilar metals are immersed in a common electrolyte and share electrical contact. In the case of the C-SWB experiments, the electrodes are connected by a known resistive load. The total electrochemical potential (i.e. battery voltage) of the energy harvester is the sum of the half-cell potentials of the anode and cathode [9]. A major advantage in using the Galvanic series corrosion scheme is the cathodic protection of the more noble metal, which is carbon in this case. This model could prove to be useful in the corrosion defense of reinforced concrete structures by creating a Galvanic series battery using magnesium as a sacrificial anode with the reinforcing steel serving as the cathode. By using magnesium as a sacrificial anode, it is possible to design an energy harvester that both protects a significant bearing structural element from corrosive attack, and still provides sufficient power for a wireless sensor node.

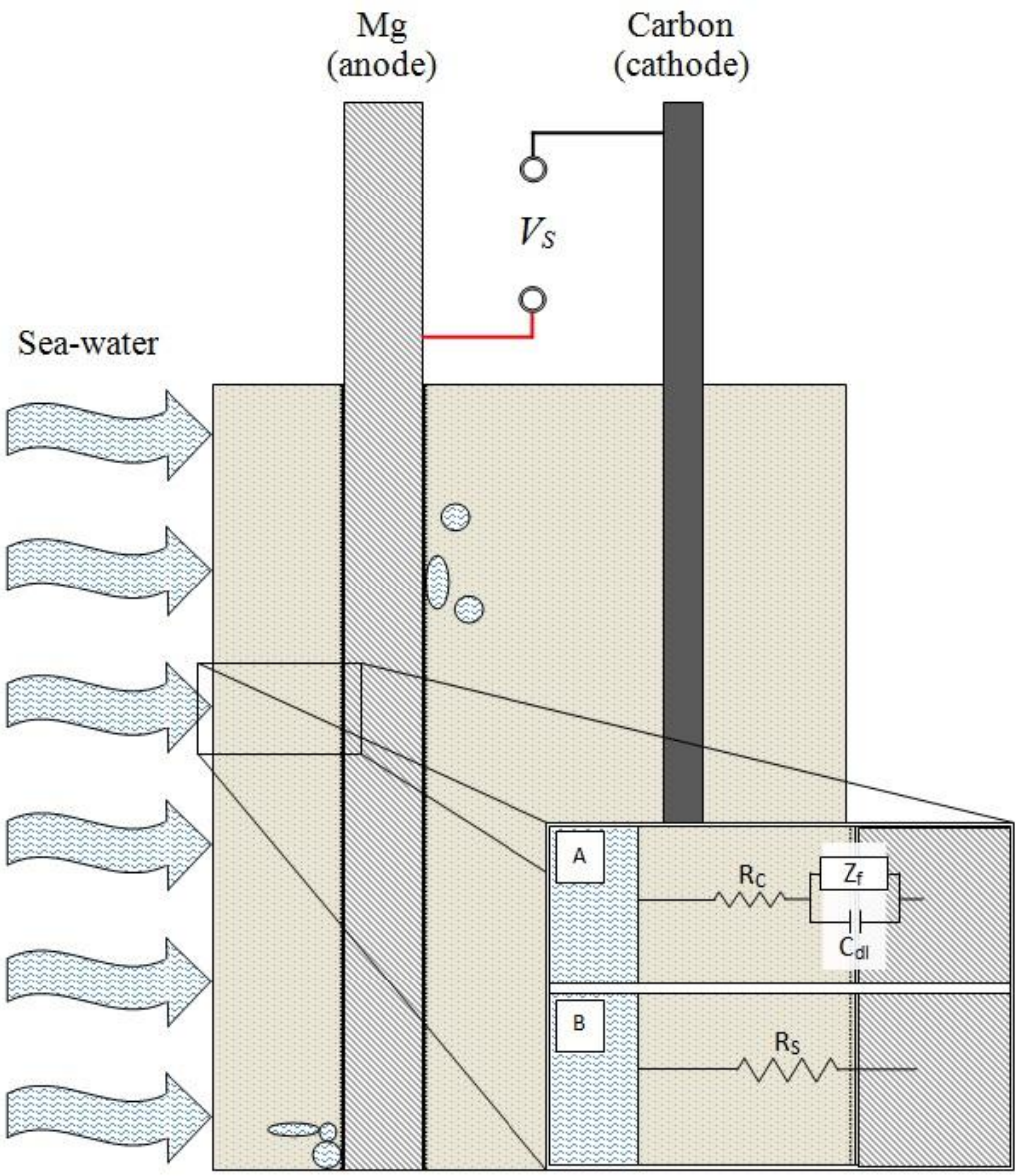

Figure 11. Diagram of C-SWB design, and the equivalent circuit models used to describe the ionic charge transfer.

Due to their high relative electrical potential, the electrodes selected for the cement battery are magnesium (Mg) and carbon (C). Based on the Galvanic series for corroding metals, the expected output voltage for the energy harvester is approximately 1.8 V. The magnesium

samples used in this study are from a generic water heater unit since it was easier to procure, in the correct shape (cylinder), and of affordable cost. However, the specific properties of the samples were not listed by the manufacturer, and, based on the experimental results, we have concluded that the sample was not pure magnesium. For the purposes of this study, the equivalent circuit model and power conditioning circuitry are intended to be robust to minor parameter variations such as material purity/homogenity.

Under uniform corrosive attack in an aqueous solution, the chemical process is described by equations 15a and b below.

$$Mg \rightarrow Mg^{2+} + 2e^{-} \quad (15a)$$

$$O_2 + 2H_2O + 4e^{-} \rightarrow 4OH^{-} \quad (15b)$$

Since there are no carbon ions in the electrolyte to be reduced to carbon atoms for a cathode reaction, oxygen and water molecules will react to form hydroxyl ions [9]. This reaction occurs because the pH of seawater ranges from basic to neutral depending on local environmental conditions [72]. Charge neutrality will impose on equation 15a that two magnesium atoms will be oxidized on the surface for each reduced oxide (O_2) molecule.

There are additional aspects of the chemical process of this battery unique to the design implementation of the cement cover. As a result of the porous structure of the cement, the magnesium anode will start to exhibit pitting corrosion at the local metallic surface sites where a cement pore is filled with seawater. This compositional heterogeneity results in a local increase in the corrosion rate of the anode. The oxidation reaction that takes place is the same as indicated in equation 15a; however, the increased concentration of metal ions requires a

proportional increase in chloride ions to sustain charge neutrality in the pit. Furthermore, a highly acidic by-product of the charge neutrality condition causes a proportional increase in the rate of local corrosion. Thus, the entire chemical reaction would become autocatalytic if not for the limited rate of oxygen diffusion to the pitting site. The pitting reaction is shown below in equation (16).

$$Mg(Cl)_2 + 2H_2O \rightarrow Mg(OH)_2 + 2HCl \quad (16)$$

The by-product of the corrosion process for the C-SWB is an insoluble magnesium-oxide. Consequently, this battery design suffers from a similar issue with reinforced concrete in that the resulting deposits generate expansive stresses on the cement cover, which, if left unabated, can result in cracking. An appropriate solution to this problem would come from the implementation of a local solvent to dissolve the magnesium-oxide precipitate.

2.2.2. Equivalent Circuit Model

When implementing an energy harvesting scheme, it is often useful to develop an equivalent circuit model to approximate the electrical characteristics of the energy harvester. A common low-order circuit model is one which has an ideal voltage source and a series resistor. This type of model is known as Thevenin's equivalent circuit, and it is derived from his theorem which states that any two-terminal network of voltage sources and resistors is equivalent to a single resistor (R_{TH}) in series with a single voltage source (V_{TH}). This section will apply the Thevenin model to the C-SWB energy harvester as a power supply (i.e. a source

of voltage and current), and use this basis for the power electronics and control circuit design detailed in Chapter 3.

Determining the Thevenin equivalent source voltage ($V_{TH} = V_S$) and series resistance ($R_{TH} = R_S$) for an uncharacterized power supply can be accomplished in two steps. First, the Thevenin equivalent voltage is simply the open circuit voltage, which can easily be measured using a voltmeter. The conventional method for determining the Thevenin equivalent series resistance is to apply a variable resistive load in series with the two terminals (Figure 12a). This can be accomplished by using any two adjacent terminals in a potentiometer and measuring the voltage (V_{load}) across the potentiometer (load) for each resistor/resistance value. The equivalent series resistance can then be experimentally identified using Ohm's Law, equation (17a), and the expression for electrical power, as shown in equation (17b). Using the measured resistive loads and their respective load voltage values, it is possible to generate the power versus resistance characteristic curve shown in Figure 12b.

The circuit diagram in Figure 12a is commonly referred to as a voltage divider, and an expression for the voltage across the load resistor (V_{load}) is easily derived, and shown in equation (17c). Therefore, generating the characteristic power versus resistance curve can be accomplished analytically, and thus provides a basis for comparing experimental results to the Thevenin model (Figure 12b).

$$V_{load} = I_{load} R_{load} \tag{17a}$$

$$P_{load} = V_{load} I_{load} = \frac{V_{load}^2}{R_{load}} = I_{load}^2 R_{load} \tag{17b}$$

$$V_{load} = \frac{R_{load}}{R_S + R_{load}} V_S \tag{17c}$$

a) b)

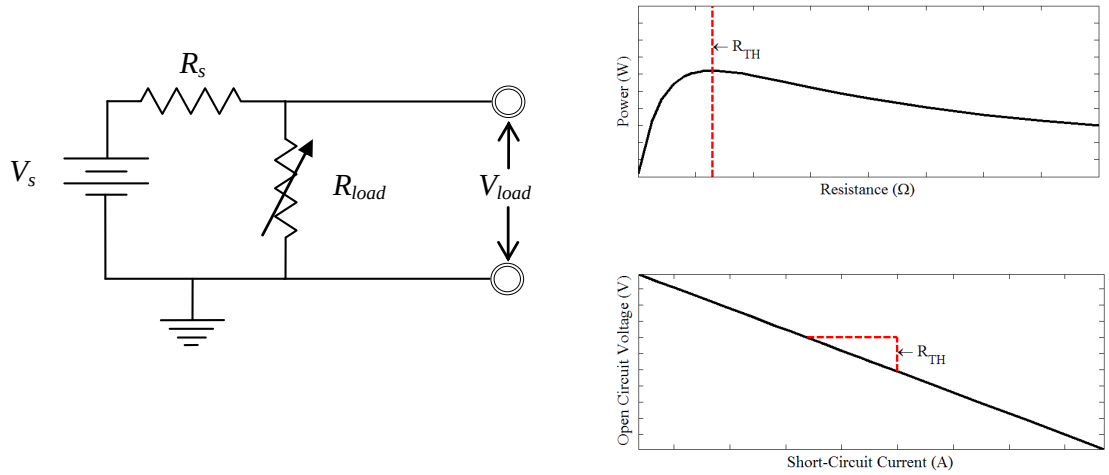

Figure 12. a) Schematic setup for experimentally determining the source resistance of a Thevenin circuit, and b) the characteristic results.

The peak power point for a Thevenin circuit occurs when the load resistance (or impedance, for AC sources) is equivalent to the source resistance; a scenario widely known as impedance matching. Plotting the open circuit voltage versus the short circuit current will verify Ohm's law in which the slope of the line is the source resistance (R_S), as shown in Figure 12b. Additionally, plotting this data for experimental power supply platforms is a good measure of circuit linearity.

With regard to the application presented in this chapter, Thévenin's equivalent circuit is used to model the C-SWB. As shown in Figure 12a, the energy harvester is modeled as an ideal voltage supply with an ideal series resistor representing the resistivity of the cement barrier between the electrodes. It should be noted that more accurate circuit models for corrosion of reinforcing metals in concrete with seawater as the electrolyte exist [73], [74]. These models feature an additional series capacitor and resistor in parallel in order to approximate the surface resistance and capacitance to charge transfer. This section is mainly focused on the dominant

resistive behavior of the cement as it pertains to the total output power characteristics as a DC source, and therefore will ignore the second-order effects of frequency dependence in the corrosion process [75].

The application of Ohm's Law and the equation for electrical power can be used to determine the power (P_L) supplied to a resistive load (R_L):

$$P_L = V_S^2 \frac{R_L}{(R_S + R_L)^2}, \tag{18}$$

where, V_S, and R_S are the equivalent source voltage and resistance for the cement battery, respectively. The implications of equation (18) dictate that the maximum power extracted from the battery occurs when $R_S = R_L$, the condition for impedance matching.

2.3. Experimental Setup and Results

Two galvanic series C-SWB specimens were fabricated and tested over the course of 9 days in a controlled sea-water bath at the Scripps Institution of Oceanography (SIO), as shown in Figure 13. The testing procedure was designed as a resistor sweep over 50 discrete resistance values in which the voltage across the load resistance was measured. Between each load resistance measurement trial, a baseline measurement of the open-circuit voltage of the C-SWB specimen was obtained. Each trial, in which the C-SWB was connected to a load resistance, lasted 30 s in duration. The NI PXI 1042Q (National Instruments) data acquisition (DAQ) controller would then switch the NI TB-2627 multiplexer (MUX) to connect the other specimen to perform the same test. As shown in **Error! Reference source not found.**a, there was a

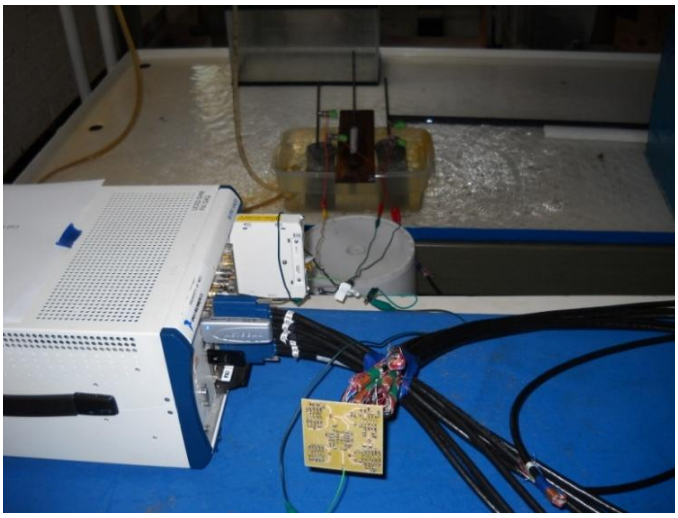

Figure 13. Experimental setup of C-SWB specimen, sea-water bath, and DAQ

programmed 15 s delay in between each trial, and an open-circuit voltage measurement trial lasting 30 s was performed.

The resistor sweep was performed from low-to-high resistance for each specimen, and then from high-to-low resistance in the following test. This testing regimen occurred continuously for the duration of the 9 day experiment. The 50 discrete ceramic surface-mount resistors were placed on a custom designed and fabricated printed circuit board (PCB) developed to interface with the MUX. The resistance values spanned the range from 10-800 Ω, with the highest value density in the range of 100-250 Ω in order to observe the peak power for each specimen and test. Each ceramic resistor was connected to a specific channel on the MUX, and of the 50 resistors used, 9 suffered from connectivity issues. Additionally, for tests in which the resistance values were swept from high-to-low, an additional 8 channels suffered from cross-talk power corruption. The exact source of the cross-talk power is unknown; however, as seen in Figure 14b, this effect was quantified by running the DAQ tests with no external power connected to the resistor board.

(a)

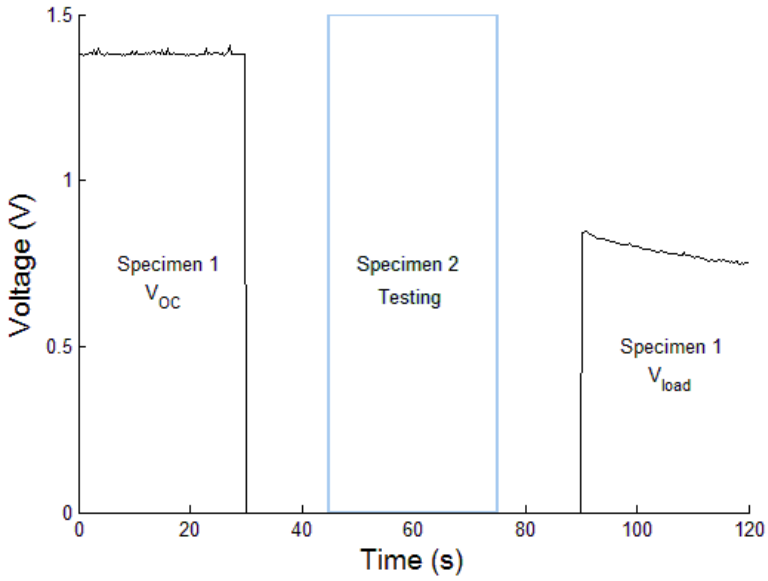

(b)

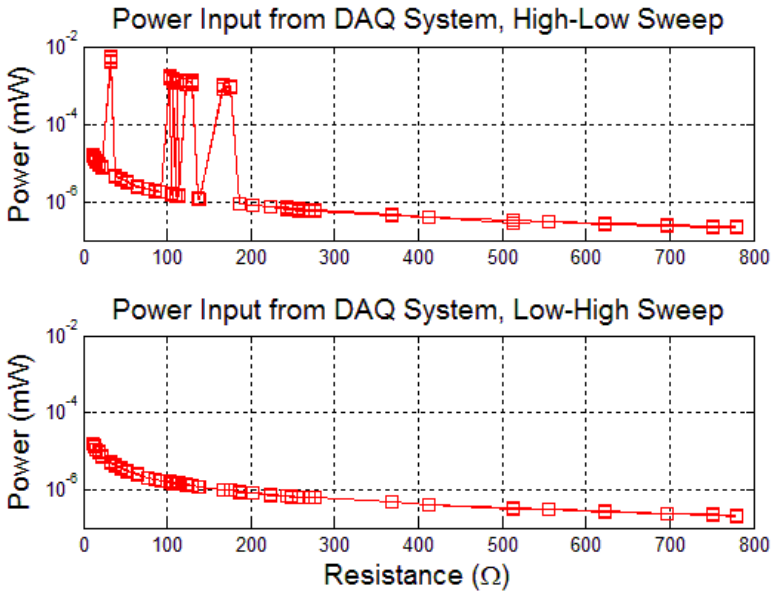

Figure 14. (a) Voltage traces as stored on the DAQ detailing the testing protocol, (b) power contamination from DAQ on the high-to-low resistor board sweep tests

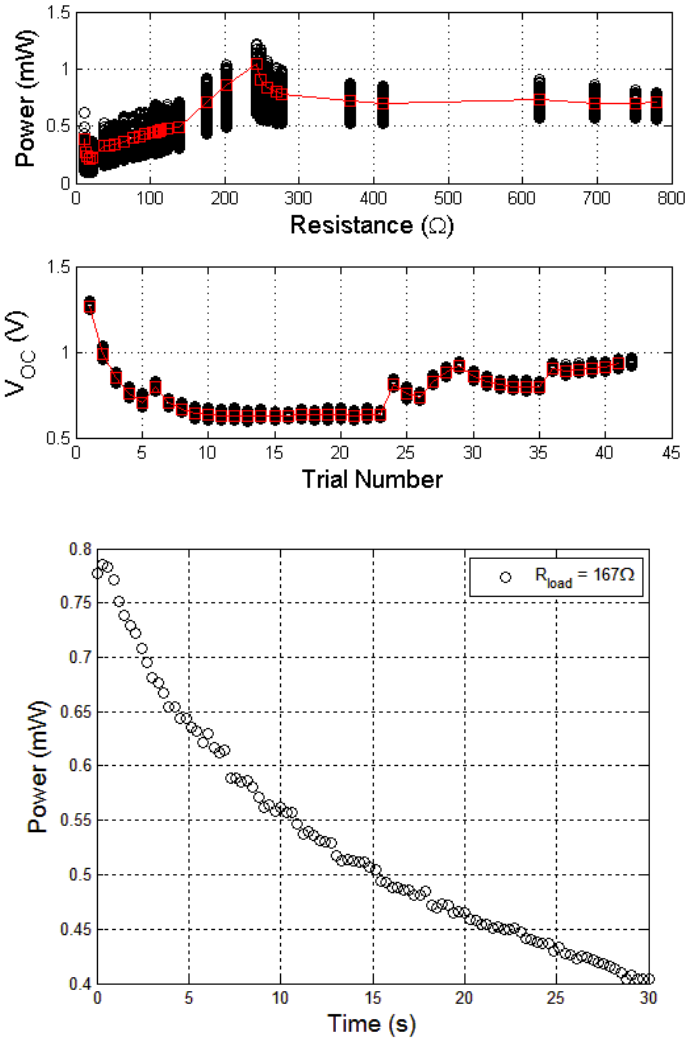

Figure 15. (top) Electrical power measured across resistive load with Thévenin equivalent power estimate (in red), and non-stationary power output across a resistive load (bottom)

The acquired data from each test was stored as a .txt file with the title automatically generated by a timestamp, and each measurement trial initiated with an identification header. The sampling frequency of the DAQ was set to its lowest sample rate at 1000 Hz. Given the time-length of each measurement trial, the DAQ would acquire and store 30,000 sample points for each resistive load trial. In order to reduce the data size for processing results, a custom Matlab function (battDataConvert.m) was written to read each line of the .txt file and sort the

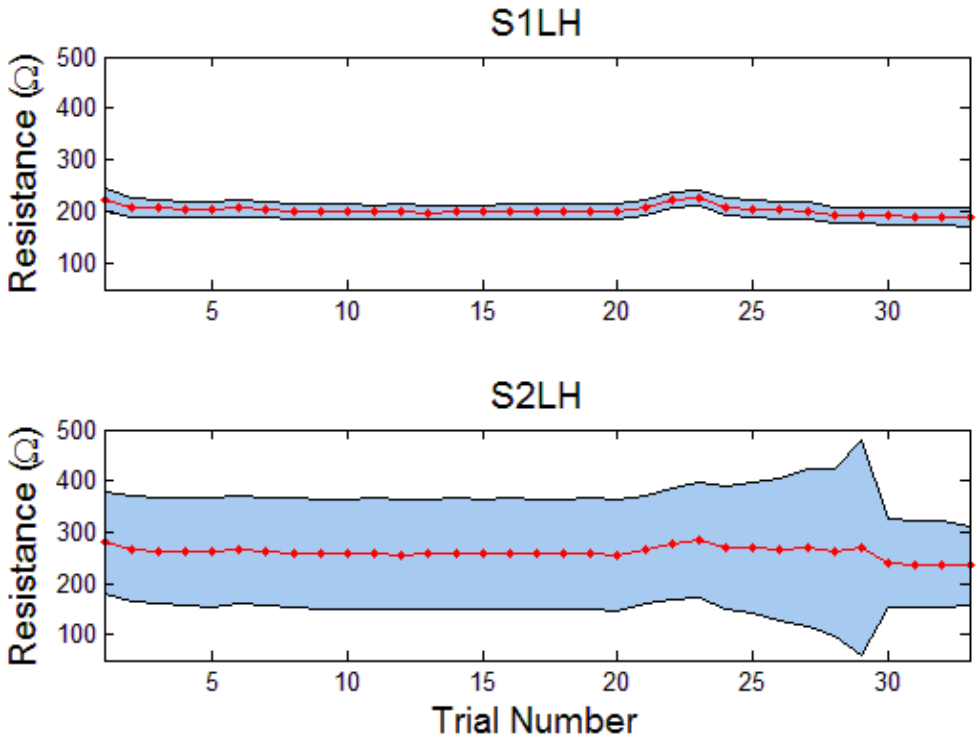

Figure 16. C-SWB parasitic resistance variability across all load resistance trials for each test specimen

data (open-circuit measurements, and load voltage measurements) into a structure where 100 evenly distributed points were recovered from the original 30,000 samples. A cursory inspection of the entire 30,000 sample points for a single test was examined to verify the decimation procedure; and though the data was non-stationary, it was not oscillatory, thus justifying the data reduction. Another Matlab m-file was then written to use battDataConvert in a loop to convert all of .txt data into a single MAT file structure which was then saved as a local variable to reduce future data processing runs.

Over the course of 9 days, over four-hundred thousand data points – 425,700 to be exact – from 129 tests were stored after the data decimation procedure. Overall, the data is stored as a 3-dimensional array (100x41x129) consisting of the sample points in each trial

(100), the number of uncorrupted load resistance trials (33), and the number of tests performed (129). The test data was sorted into specimen and sweep direction (high-to-low, and low-to-high).

$$R_{TH} = \frac{R_{load} * V_{TH}}{V_{load}} - R_{load} \tag{19}$$

Theoretically, there should be no difference in the results between sweep directions based on the equivalent circuit model; however the data will suggest otherwise. This is partially due to the power contamination from the DAQ, and partly due to the low order model applied to the C-SWB energy harvester which fails to capture the non-stationary capacitive effects of the corrosion process [73]. The power output from each C-SWB energy harvester specimen was calculated from the expression:

$$P_{source} = P_{load} = \frac{V_{load}^2}{R_{load}} \tag{20}$$

where V_{load} is the measured voltage on the DAQ for a known resistive load (R_{load}). Due to the non-stationarity of the output power across the load resistance, the task of characterizing the power output of the energy harvester requires a statistical approach. Therefore, for each load resistance trial, the max, min, and mean power were calculated. The same calculations were performed on each open-circuit voltage trial.

When plotting the measured power versus the applied load resistance, the expected curve for a Thévenin circuit is not observed exactly. The reason for this is because the model assumes an ideal constant voltage source. The C-SWB energy harvester, however, has a non-stationary voltage output as a result of several parameters involved in the corrosion process, as will be described in the following section. Therefore, in order to correct for these variations, the open-circuit voltage measured prior to each resistive load trial is used as the representative source voltage for the model. The results show that the Thévenin model (shown in red) performs fairly well when compared to the data for each trial and test. For the results shown in Figure 15, an assumed internal resistance of 200 Ω was used. Since the Thévenin model was accurate to within 4%, the internal resistance of the C-SWB can be determined by manipulating equation (19), the application of which yielded internal resistance values of approximately 200 and 250 Ω, respectively.

2.3.1. Statistical Properties of C-SWB Output Power

Due to the non-stationary characteristics of the corrosion process involved in generating the battery power, as well as variations from specimen to specimen, a statistical approach to describing the energy harvester is used to assist with modeling the expected supply power to the sensor node. The parameters that can be varied for the energy harvesters design are as follows:

Anode to cathode spacing

Cathode to anode surface area ratio

Cement cover thickness

Water-cement ratio (a controlling parameter in cement porosity)

Materials selection for anode and cathode (subject to Galvanic series)

Oxygen concentration at cathode

Constraints with data acquisition hardware allowed for only two test specimens to be made with the varied parameter being cement porosity. The cement pastes were mixed with a water-cement ratio of 0.4 and 0.45, and air-cured for a period of 14 days. Under these conditions, the expected porosity is between 14.4-29.1% and 13.7-31.6% for w/c of 0.4 and 0.45, respectively [76]. The range of measured porosity percentage is an artifact of the method used.

The open circuit voltage statistics for each cement battery specimen are shown in Figure 17. Each column in the above figures represents the sum of each histogram of the open circuit voltage measurements for a specific trial over the range of all tests. Thus, the first column represents all measured open circuit voltages at the start of each resistor sweep test. The results indicate a large variation in the measured open-circuit voltage over the course of the experiment. Specimen 1 exhibits a near tri-modal voltage distribution, with the peaks at approximately 300 mV, 600 mV, and 900 mV. The statistics for specimen 2 have much less overall variation, but still exhibit the characteristic of multiple peaks.

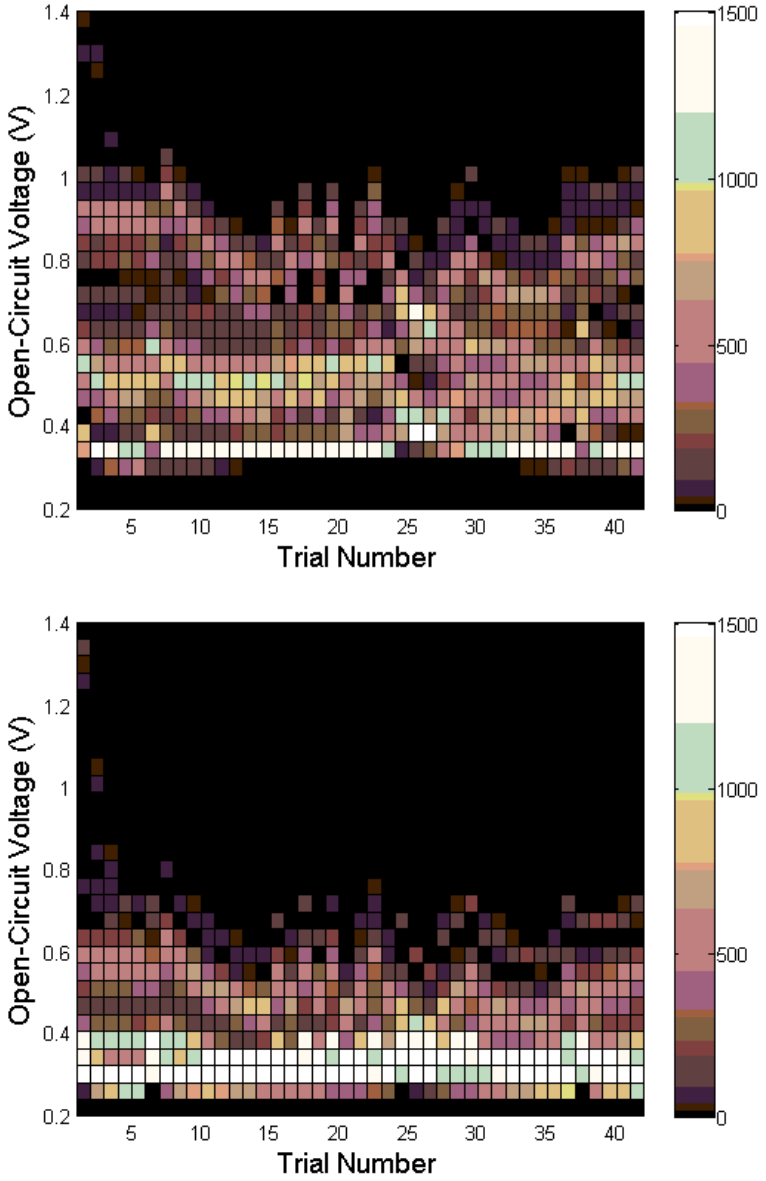

Figure 17. (top) Open-circuit voltage statistics for specimen 1, where each trial consists of a baseline open-circuit measurement between connecting to a resistive load. Open-circuit voltage statistics for specimen 2 (bottom)

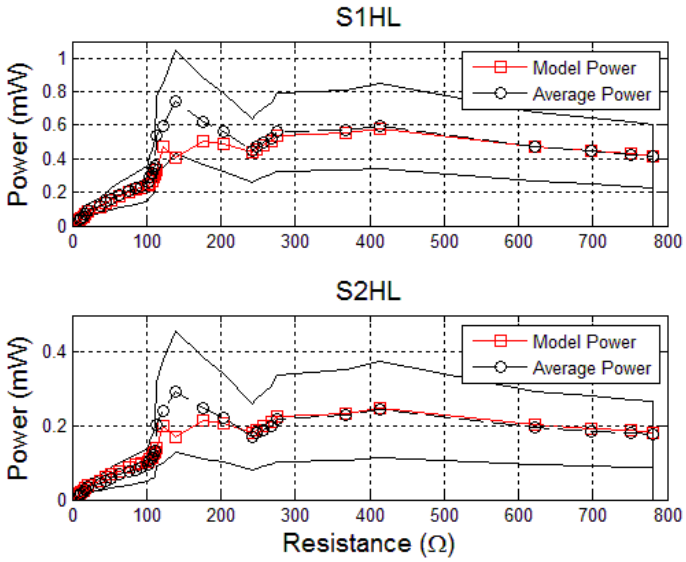

Figure 18. Power output for high-to-low resistive load sweeps for specimen 1 (top) and specimen 2 (bottom)

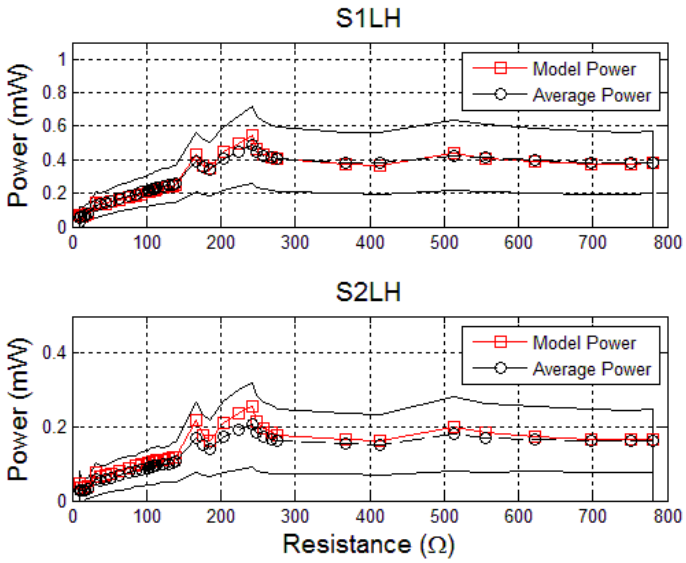

Figure 19. Power output for low-to-high resistive load sweeps for specimen 1 (top) and specimen 2 (bottom)

.

For each specimen, the modal voltage is approximately 300 mV, which is much lower than the designed output voltage of 1.6 V. Furthermore, for both specimens, there appear to be outlier voltage measurements around 1.3 V. The explanation behind this is actually rather simple in that these measurements indicate the first data points measured for the entire experiment. Factors contributing to the degradation of the output voltage of the battery grow in influence with time.

After processing the data, the cause of the output voltage disparity was determined to be rusted measurement probes. The rust was primarily confined to the carbon cathode/measurement interface as the probes were made of stainless steel. This event resulted in the DAQ measuring the voltage potential between the rust (most likely iron-oxide) and the magnesium hydroxide (an insoluble by-product of the corrosion process), which has significantly lower potential than the carbon/magnesium potential. Though measures were taken to avoid as much experimental error as possible, the longevity of the experiment combined with the test environment increased the occurrence of these experimental issues. This was an expected trade-off in reliability when deciding to automate the long-term measurement process.

The output power variability of each specimen is shown in Figure 18 and 19. The figures show the measured mean power and one standard deviation, with the mean model power for comparison. The power characteristic for each sweep direction was analyzed separately as a metric of load response linearity. The results for both specimens show that there is a slight difference in the output power near matched impedance depending on the sweep direction. Though the Thévenin equivalent circuit model is linear, and thus does not exhibit a bias with regards to the load sweep direction, the results for each trial still validate the model

with the only variation being the non-ideal source voltage, which is accounted for iteratively with a data-driven approach.

2.3.2. C-SWB Power Capacity

When analyzing an energy harvester for its potential to be deployed in infrastructure monitoring scenarios, it is often instructive to compare the total available energy to that of more conventional power supply technology. A first-order corrosion rate model can estimate the current capacity of an anode of a given material by [9].

$$\frac{It}{V} = \frac{nF\rho}{M}, \tag{21}$$

where, I is anode current [mA], t is the time [hr], V is the anode volume accounting for porosity effects [cm^3], n is the number of electrons produced in the oxidation reaction, F is Faraday's constant [$mA \bullet hr\ mol^{-1}$], ρ is the anode density [$g\ cm^{-3}$], and M is the anode atomic weight [$g\ mol^{-1}$]. The expression relates the current capacity per unit volume for a corroding metal anode encased in cement, where the porosity factor scales the amount of available surface area of the anode for corrosion initiation sites.

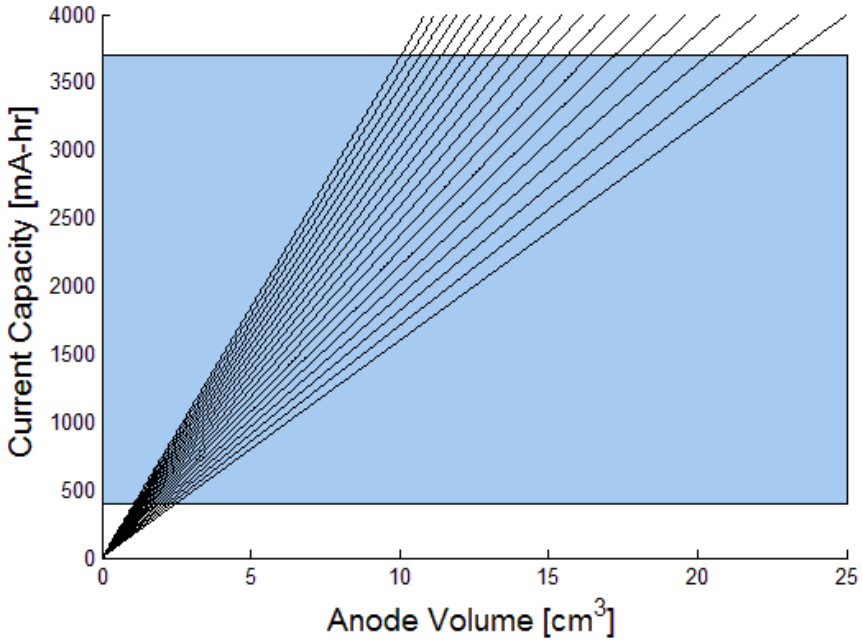

Figure 20. C-SWB capacity for various cement porosity factor values with the current capacity for conventional AA batteries in blue.

A portion of Chapter 2 has been published in IEEE Sensors Journal, Scott Ouellette and Michael Todd, 2013. The title of this paper is "Cement Sea-Water Battery for Marine Infrastructure Monitoring". The dissertation author was the primary investigator and author of this paper.

Another portion of Chapter 2 has been published in Proc. of SPIE, Scott Ouellette and Michael Todd, 2012. The title of this paper is "Ultra-Low Power Corrosion-Enabled Sensor Node". The dissertation author was the primary investigator and author of this paper.

Another portion of Chapter 2 has been published in Proc. of SPIE, Scott Ouellette and Michael Todd, 2013. The title of this paper is "Uncertainty Quantification of a Corrosion-Enabled Energy Harvester for Low-Power Sensing Applications". The dissertation author was the primary investigator and author of this paper.

Chapter 3
Low-Power Sensor Node Design

3.1. Introduction to Power Electronics Design

As explained in Chapter 1, energy harvesting systems for wireless sensor netowrks can be described by three stages: ambient energy transduction, electrical power conditioning, and data acquisition and transmission. Within the past 10 years, developments in low-power CMOS devices have allowed for expanded energy harvesting techniques by reducing the total power demand of sensor nodes. This chapter details the system-level interaction between the C-SWB energy harvester and a custom designed low-power sensor node to which the power is suppled. To accomplish this, I developed an equivalent circuit model of the energy harvester and matched the parameters (source voltage and equivalent series resistance) for use in the design of the power conditioning and wireless transmitter circuitry. Analysis of the power demand from the sensor node is studied to determine the optimum data sampling parameters in terms of available supplied power for long-term *in-situ* sensing operations on a marine structure.

Using the C-SWB as an energy harvester only solves part of the overall monitoring problem. In order to acquire data on the health of a structure subject to corrosive attack, it is imperative that the energy produced by the batteries be used to power appropriate sensing and

communications telemetry. However, based on the output voltage distribution of the cement seawater battery, the sensor node will require a DC-DC boost converter to accommodate the voltage requirements of a CMOS microcontroller. I designed the DC-DC boost converter in this study to convert low input voltages and output a feedback-regulated 3 VDC supply. The power generated by the C-SWB energy harvester is isolated from the boost converter and microcontroller by a low on-resistance analog switch in order to prevent continuous operation of the voltage conditioning circuitry. The analog switch is controlled by a low-power PWM timer IC. The following sections detail each component of the low-power sensor node design

3.1.1. Energy Buffer and Load Isolation

Analysis of the output power characteristics of the cement battery prohibits the direct application of a DC-DC boost converter due to the current demand by most commercially available boost converter ICs. Therefore, it is necessary to use an energy buffer (typically a super-capacitor) to function as the power supply for the boost converter, sensor node, and wireless transmitter. By implementing a low on-resistance analog switch in conjunction with a 100 mF super-capacitor (as seen in Figure 21), the cement battery can store energy for a defined time interval, and then rapidly discharge the energy to power the sensing telemetry.

The analog switch (SN74AUC2G53, Texas Instruments) is a low-voltage single-pole, double throw (SPDT) switch that isolates the buffer capacitor from the boost converter, MCU, and transmitter. It is important that this switch has a low on-resistance in order to avoid losses in power transfer to the boost converter. The switch is controlled by a low-voltage, low-power timer IC (TLC 551, Texas Instruments) set to generate a very low duty cycle PWM signal. It is important to note that the analog switch and timer IC must be able to operate with a low supply voltage (~1 V) and have a minimal current consumption. Between the analog switch and timer

IC, there is only 303 µW of power consumption for operation, with the switch having an additional 1 µA leakage current.

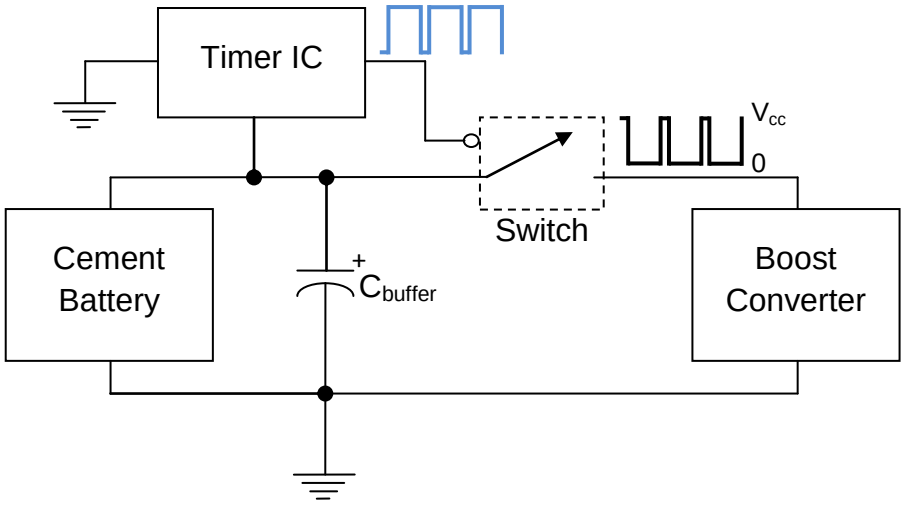

Figure 21. Schematic diagram of the low on-resistance analog switch and energy buffering capacitor

The main concept at work with this use of an energy buffer stems from the desire to have the sensor node operate from a single C-SWB energy harvester supply. Using a capacitor to provide power enables a circuit to drive high load demands. This is because the power delivered by a capacitor is a function of its inherent capacitance, the charge voltage, and, most importantly, the rate at which it discharges the stored energy, as shown in equation (22).

$$P_{capacitor} = CV\frac{dV}{dt} \tag{22}$$

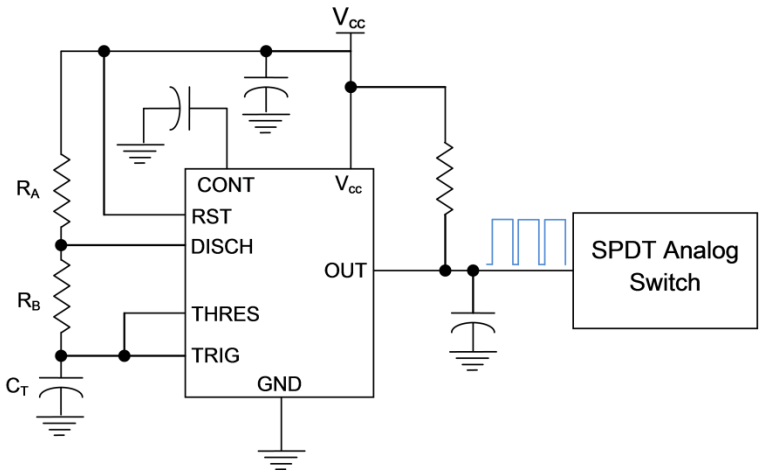

Figure 22. Schematic diagram of the low-power timer IC

Taking advantage of this fact, this design can provide enough power for all the sensing and communication needs by simply tailoring the PWM control signal from the timer IC. The timing control signal IC is essential to the overall sensor node operation, as it sets the functional duty cycle of the device. The charge/discharge time is set by the resistor pair (R_A, R_B), and is scaled by the threshold capacitor (C_T) as seen in Figure. 22. The equations that approximately describe the output PWM duty cycle and frequency are shown below [77]:

$$\begin{Bmatrix} t_{on} \\ t_{off} \end{Bmatrix} \approx C_t ln2 \begin{bmatrix} 1 & 1 \\ 0 & 1 \end{bmatrix} \begin{Bmatrix} R_A \\ R_B \end{Bmatrix} \tag{23}$$

Due to the internal architecture of this specific device, it is largely impractical to generate a duty cycle lower than 50%, with the only method being to drive R_A below the internal device resistance. Given the power demands of the sensor node, and the total output

power of the C-SWB, it is imperative that the charge/discharge cycle of the buffer capacitor must be less than 50% for the energy transfer to be optimal. Therefore, the only option is to set the circuit parameters to generate a very high duty cycle (~99%) and to invert the signal on the control pin of the analog switch. This can be done two ways: 1) implement a simple inverter circuit using an OpAmp, or 2) exploit the internal logic within the SPDT analog switch. For ease of implementation, option 2 was chosen by connecting the output of the switch to the logic scenario when the control input and reference voltage are low (GND). For the purposes of this study, the desired on-time/off-time PWM signal was chosen such that the buffer capacitor would drain for 20 ms for every 1-minute period. A detailed power analysis of the entire sensor node, accounting for the MCU and transmitter, will demonstrate a more optimal duty cycle.

3.1.2. Switched-Mode DC-DC Converter

The output voltage signal from the discharging capacitor is a low duty cycle square wave. The boost converter used in this initiative features a low-voltage micro-power step-up switching regulator IC (LTC3402, Linear Technology). This IC is feedback regulated to provide an adaptive switching frequency which holds the output voltage of the boost converter constant. The component values were chosen to provide a stable 3 V supply to the MCU and transmitter.

Due to the variability in output voltage of the cement battery, Monte Carlo simulations were performed using LTSpice IV (Linear Technology) on the component value variability, as well as input voltage variability to verify robust boost converter operation and a stable output voltage. The circuit model consisted of the 100 mF buffer capacitor supplying power to the boost converter in 20 ms intervals across an ideal switch controlled by a set PWM voltage signal. The charge voltage on the supply (buffer) capacitor varied from 0.5-1.8 V, and the MCU

was modeled as a piecewise linear varistor to account for the power consumption between two programmed states of operation, active mode (AM) and low-power mode (LPM0).

The results of this parametric study suggested the boost converter would be capable of producing an output voltage of 3 V ± 100 mV over an input voltage range of 0.6-1.8 V. The cutoff voltage of the boost converter is mainly a result of the rectifying output diode requiring 600 mV to conduct. A prototype printed circuit board (PCB) of the energy buffer and boost converter design was fabricated and tested in the lab. A lab-bench power supply with an equivalent series resistance was used to emulate the cement battery power as designed, and the output voltage was probed to validate the simulation results.

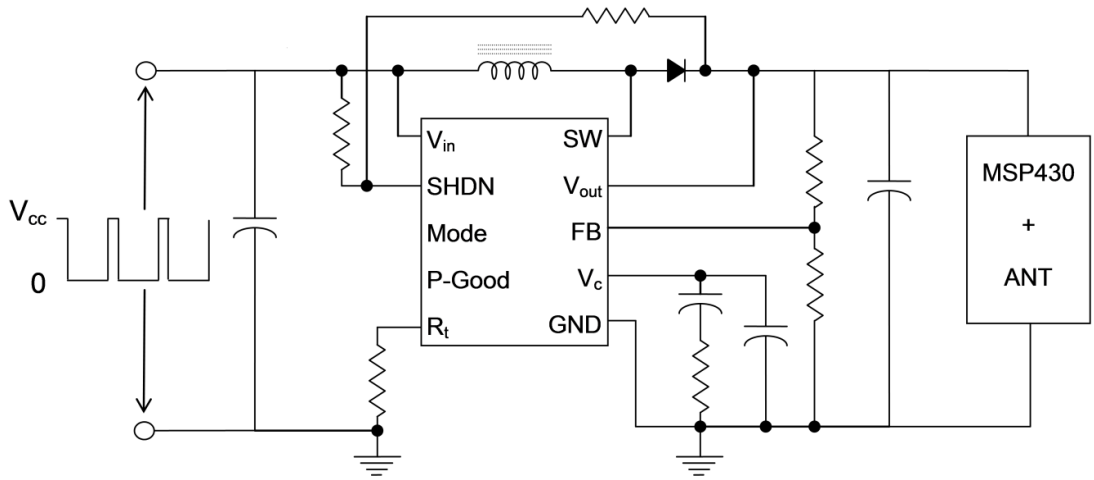

Figure 23. Schematic diagram of boost converter design

(a) (b)

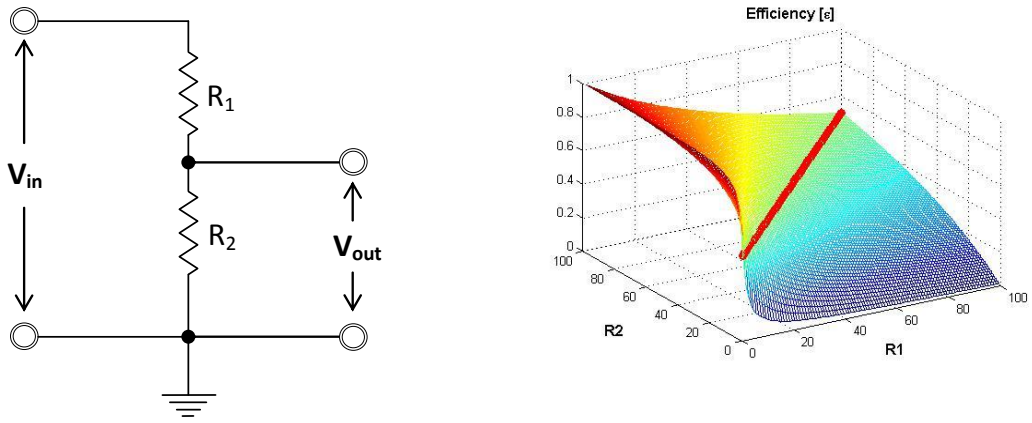

Figure 24. (a) equivalent circuit model of interaction between C-SWB energy harvester and electrical load, (b) power transfer efficiency for a voltage divider circuit as a function of various resistance values with the matched impedance efficiency overlaid in red.

3.2. Power Transfer Efficiency Analysis

It is often instructive to develop an equivalent circuit model for later use towards the design and development of the power conditioning circuitry. For battery-type energy harvesting devices, a good starting model is Thévenin's equivalent circuit. This model parameterizes a two terminal system into an ideal voltage source with a series resistor. A cursory review of corrosion literature suggests a slightly more exotic circuit model for oxidizing metals in concrete; however, the leading-order behavior for ohmic loads is accurately modeled by the Thévenin equivalent, and thus works well for this study.

Determining the equivalent series resistance for the cement seawater battery is accomplished by a resistive load sweep in which the peak measured power occurs at a matched load. For the purposes of this study, the resistive load sweeps were performed bi-directionally to test the source linearity. Based on the experimental data shown in Figure 19 from Chapter 2, the source resistance can be estimated to be 150 Ω. The experimental setup, however, leads

itself to a relatively high parasitic resistance due to the number of clip-connections and the length of wire used for the measurement probes.

Several energy harvesting papers have focused on developing the power electronics with an equivalent resistance to the source resistance, a process referred to as impedance matching [78]–[80]. For a simple ohmic load, the peak power transfer for a Thévenin-type source occurs at matched impedance. A circuit diagram of this scenario is shown in Figure 24. Using Ohm's law to solve for V_{out} gives:

$$V_{out} = \frac{V_{in} R_2}{R_1 + R_2} \tag{24}$$

For matched impedance, $R_1 = R_2$ and thus:

$$(V_{out})_{max} = \frac{V_{in}}{2} \tag{25}$$

and:

$$(P_{out})_{max} = \frac{(V_{out}^2)_{max}}{R_2} = \frac{V_{in}^2}{4R_2} \tag{26}$$

As seen in equation (26), the maximum output power at matched impedance is scaled by the load resistance (R_2). Therefore, reducing the internal resistance of the power source will ultimately increase the output power.

However, when considering the efficiency of power transfer from source to load, operating at matched impedance is sub-optimal with respect to the power source. In essence, for a finite power supply (e.g. a battery), connecting to a matched impedance load will draw the maximum current. In the case of the cement battery, this situation will result in an increased corrosion rate of the anode being consumed, thus reducing the operational lifetime of the sensor node.

Defining the power transfer efficiency as the ratio of output power to input power, it can be shown that the efficiency of a matched impedance circuit is only 50%.

$$\varepsilon = \frac{P_{out}}{P_{in}} = \frac{V_{out} I_{out}}{V_{in} I_{in}} \tag{27}$$

Using Ohm's law to solve for the current expressions results in:

$$\varepsilon = \left(\frac{V_{out}}{V_{in}}\right)^2 \left(\frac{R_1}{R_2} + 1\right) \tag{28}$$

Substituting V_{out} from equation (24) yields an expression for efficiency purely in terms of resistance:

$$\varepsilon = \frac{R_2}{R_1 + R_2} \tag{29}$$

Analysis of equation (29) shows that power transfer efficiency increases greatly for the condition $R_2 >> R_1$, as seen in Figure 24b. Thus for an energy harvesting system with finite supply, a sensor node with a large effective resistance is optimal. This criterion does, however, require special consideration when designing the power conditioning electronics because of the reduced current flow through the load. The following section will present one possible solution to this matter by way of an energy buffer and load isolation.

3.3. SPICE Simulations and Monte Carlo Analysis

Circuit simulations were performed on an equivalent circuit model of the sensor node and power supply using LTSpice IV (Linear Technology). The supply power for the circuit comes from the 100 mF electrolytic capacitor set with an initial voltage range of 0.4-1.7 V. All of the discrete resistors and capacitors chosen were from the LTSpice IV ideal components library. The TLC551 timer IC was modeled as an ideal voltage source supplying a specified PWM signal, which is connected to the control pin on an idealized voltage- controlled switch used to model the SN74AUG2G53 analog switch. The PWM signal in this model is set to activate the analog switch gate at the intended duty cycle and duration described in the previous sub-section. The LTC3402 switching regulator is an empirically based sub-circuit component model that comes built-in with the software download.

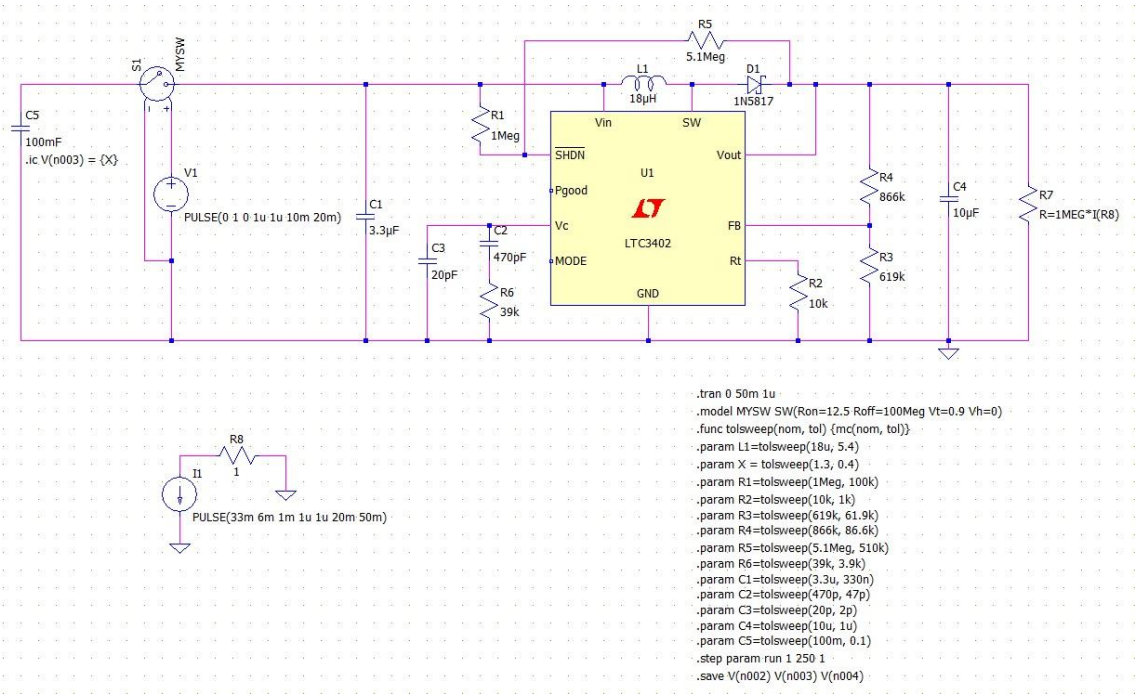

Figure 25. LTSpice IV model for used for Monte Carlo simulations of boost converter output

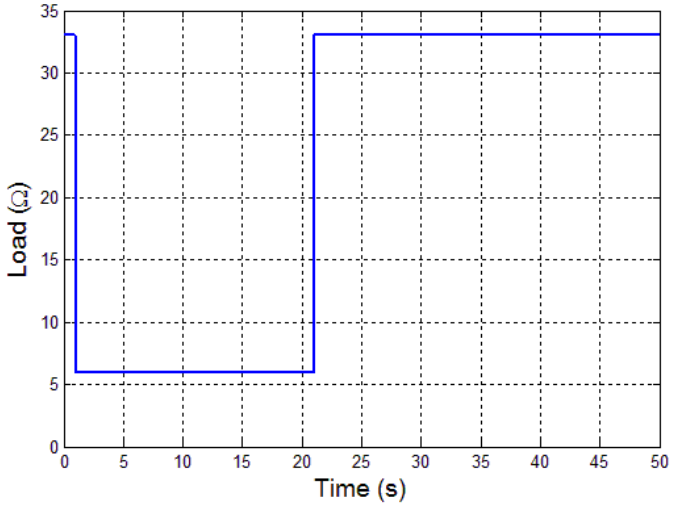

Figure 26. Varistor profile used to model MSP430 switching between operational states

The MSP430 was modeled as a piecewise linear varistor representing the power consumption when set in two different operational modes, namely the active mode (AM), and low-power mode zero (LMP0), as shown in Figure 26. The effective resistance values for the two states were calculated from the known current consumption for a given supply voltage – either 2.2 V or 3 V [22].

Each discrete component has a manufacturer-defined tolerance, and in the case of the power inductor, the tolerance for the rated inductance is as high a 30%. A 250 run, 13-parameter Monte Carlo analysis was performed in order to observe the effect of component value and input voltage variability on the output power characteristics of the boost converter. Since the boost converter employs closed-loop regulated feedback architecture, there is little effect on the output voltage delivered to the microcontroller above input voltages of 800 mV, as seen in Figure 27. However, the variations do have an effect on the output rise time to the MSP430 startup voltage of 2.2 V. As seen in Figure 28, the rise time to the minimum microcontroller supply voltage of 2.2 V can vary from 1-10 ms. Furthermore, the startup time is asymptotic as the input voltage approaches 600 mV, which is expected as the rectifier diode requires 600 mV to conduct.

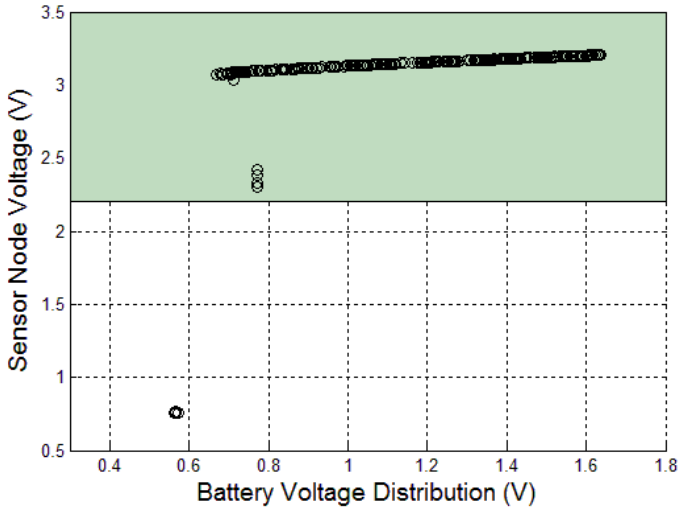

Figure 27. Output voltage distribution of Monte Carlo simulations

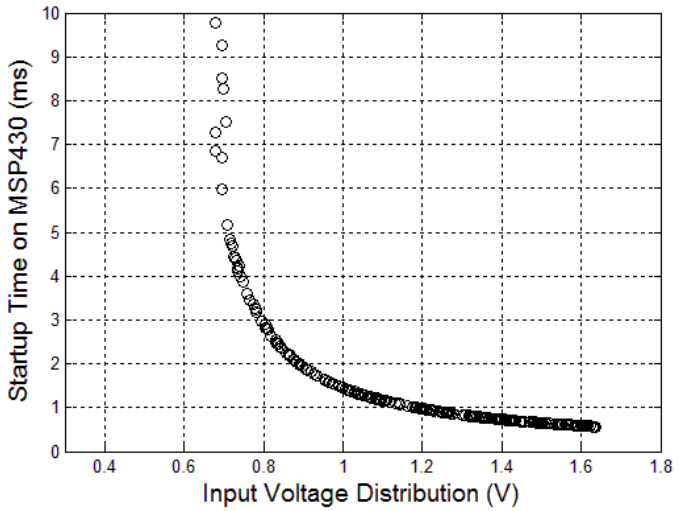

Figure 28. Distribution of startup times for various input voltage initial values

3.4. Design and Fabrication of Dual-Layer Sensor Node PCB

It was necessary to develop a prototype sensor node in order to validate the Monte Carlo simulation results and system design. A schematic of the sensor is shown in Figure 30, which contains all of the components of the sensor node (energy buffer, load isolation switch, and DC-DC converter) linked together. The software suite used to develop the dual-layer printed circuit board (PCB) sensor node was Mentor Graphics PADS Logic and Layout integrated development environments. The schematic of the circuit is designed in PADS Logic, in which discrete components (resistors, capacitors, etc.) are linked with commercial ICs, with each node connection for all components stored as a net list array that is then passed to PADS Layout.

The layout software tool is where the printed circuit board shape, component layout, and copper connection traces are drawn. The low-power sensor node is designed to comfortably fit on a 1” x 1” dual-layer board made of copper and FR4 fiberglass insulation. The top row of images in Figure 29 shows the top and bottom layout for the copper pads and trances connecting all of the circuit components. An 8 mil minimum clearance for copper traces was enforced due to the limitations of the prototyping PCB milling machine (LPKF Protomat S100).

Once the design was verified to not violate any of the preset tolerance/clearance criteria, the layout data for each layer (top copper, bottom copper, solder mask, etc.) was converted to a set of GERBER files to be processed by the LPKF milling machine. The LPKF converts the GERBER files using a proprietary computer-aided manufacturing (CAM) software package, and then transfers the vectorized PCB layout into a native software package that controls the high-precision milling head. Once the vectorized layout is placed onto the representative milling location on a blank dual-layer copper board, the only remaining steps are to have the appropriate milling tool heads loaded into a user-defined holding collet, and

calibrate the milling depth on the drill head. The bottom images in Figure 29 show the completed low-power sensor node prototype with the components affixed by standard soldering techniques.

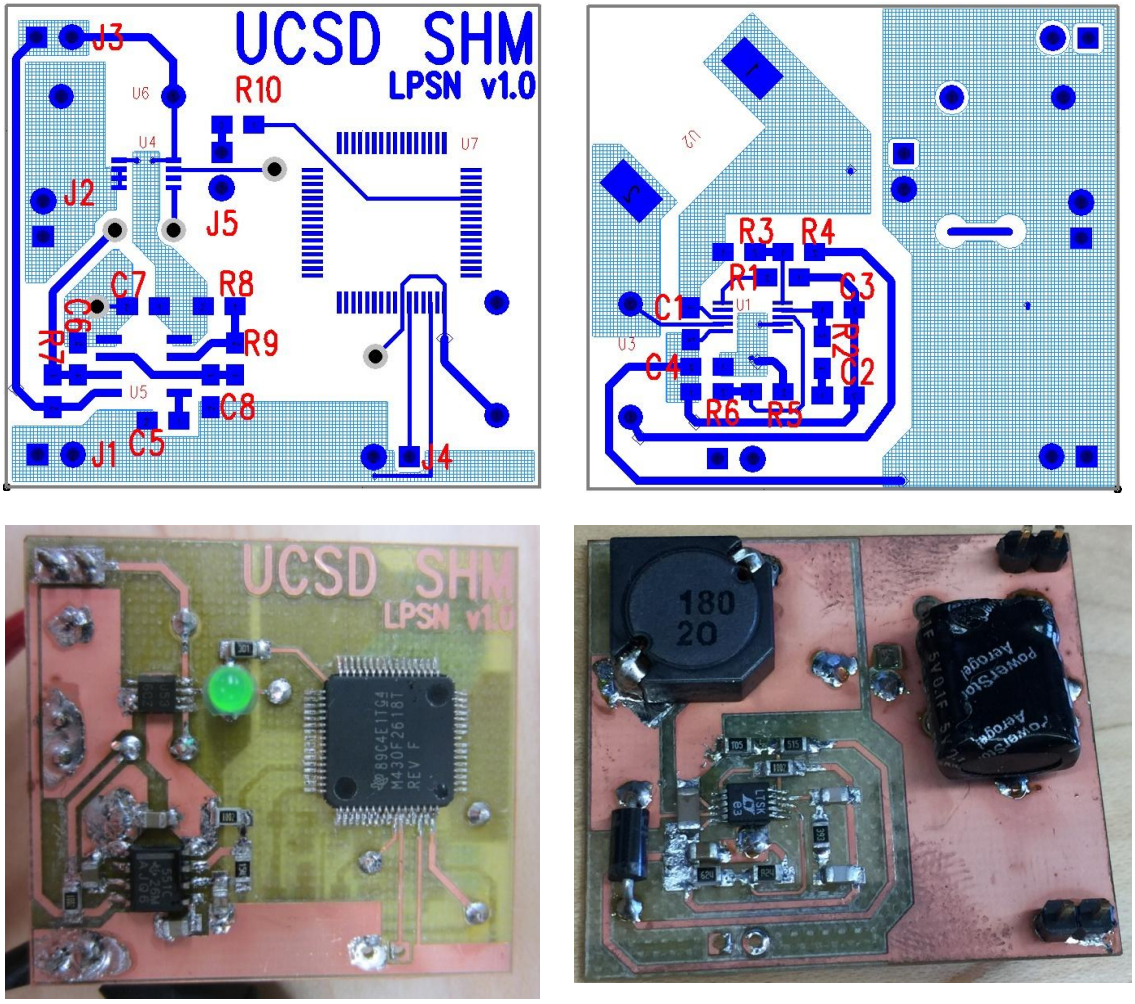

Figure 29. (top) layout diagrams of top and bottom layers, and (bottom) completed prototype top and bottom layers

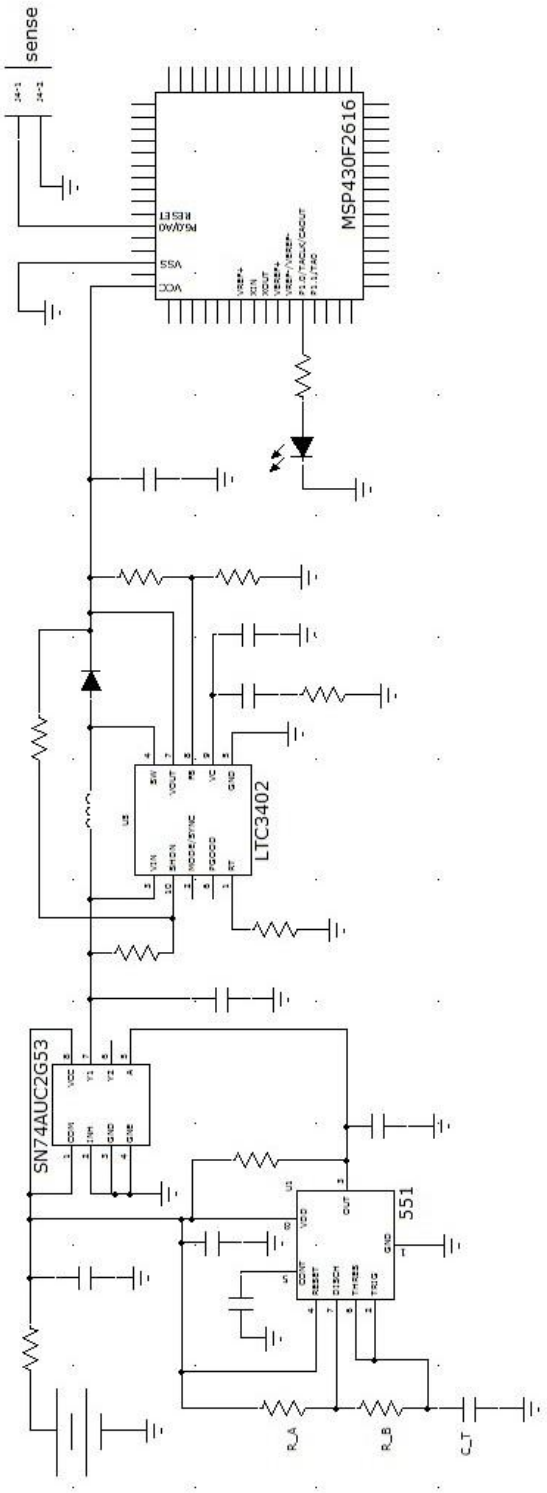

Figure 30. Sensor node schematic diagram

The final step in the development of an autonomous wireless sensing platform concerns the acquisition and management of measurement information. From a development standpoint, this stage offers multiple options in terms of sensing type (e.g. strain, temperature, acceleration, etc.) and network configuration. Furthermore, there exists a plethora of manufacturers and product solutions to choose from. This section describes the decision rationale for the choice of MCU and wireless transmitter. To date, a prototype sensor node has be fabricated and tested without the addition of the wireless transmitter system [82]. The initial results are promising in terms of the sensor node being capable of operating from the output power provided by the cement battery.

The TI MSP430 is an ultra-low power family of mixed-signal microprocessors for portable applications. The specific device used in this study features a wide supply voltage range (2.2-3.6 V) and low power consumption in active mode. In terms of input/output (I/O) capability, this device has six channels, a 12-bit ADC, and 116 kB onboard flash memory. Most importantly, the internal architecture of the MSP430 family has five programmable power modes for extending battery life. In active mode, operating at a 1 MHz clock frequency, the device consumes at most 560 μA (with a 3 V supply).

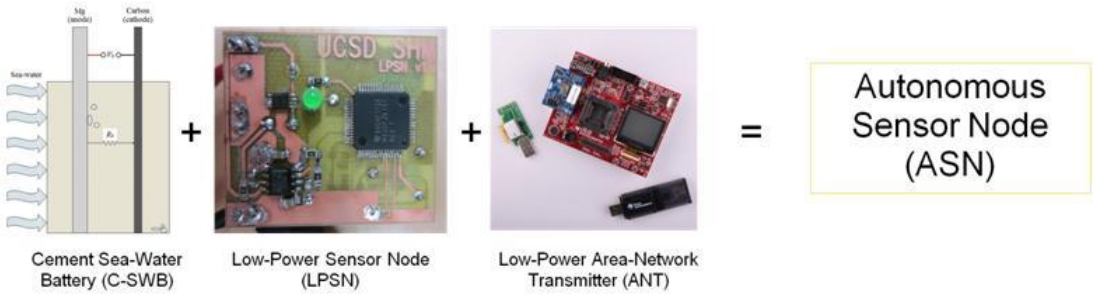

Figure 31. Proposed autonomous sensor node system components

The wireless transmitter/receiver chosen for this study is the ANT CC2571 (Texas Instruments) short-range transceiver network. This product was chosen because of its simple interface with the MSP430 devices. Furthermore, it also features very low power consumption, a user-friendly software programming interface, and a very flexible master/slave network protocol. This particular model features up to 8 transmission channels, and upwards of 200Hz broadcast frequency.

Together, the MSP430 and ANT CC2571 complete the sensing and communications needs for the sensor network. When combined with the cement battery and power conditioning circuitry, the sensing system is entirely autonomous (see Figure 31).

3.5. Power Analysis and Estimated Operational Lifetime of Sensor Node

As mentioned earlier, the timing of the analog switch was pre-determined based on the decision to allow for the buffer capacitor to fully charge prior to taking a measurement and transmitting the data. This timing sequence turns out to be a bit conservative in terms of the optimal charge/discharge rate of the buffer capacitor. This section investigates the power consumption of the sensor node and uses that information to determine the peak measurement rate for the autonomous wireless sensor node operating at max power consumption. The power consumption analysis is then used to determine the necessary anode volume for a long-term sensing operation.

The total load (mW) is calculated as the sum of all the active power consuming elements on the sensor node (resistors, capacitors, and inductors are neglected due to their small power consumption). The elements that comprise the list are: 1) the analog switch, 2) the timer

IC, 3) the boost converter, 4) the MCU, and 5) the transmitter. Reviewing the datasheets for these devices yields the power consumption table (see Table 4 below).

Table 4. Sensor Node Power Consumption

Device	Supply Voltage	Supply Current	Power Consumption
SN74AUC2G53	1.3 V	10 μA	13 μW
TLC 551	1.3 V	225 μA	0.29 mW
LTC 3402	1.3 V	800 μA	1.04 mW
MSP430	3 V	560 μA	1.68 mW
CC2571	3 V	3430 μA	103 mW

The total power consumption of the sensor node calculates to approximately 106 mW. A cursory observation of the table shows that the majority of power is applied to transmitting the data. The value for the transmitting current was obtained from the assumption that the transmitter would be operating at 4-dBm output power.

When evaluating the total power consumption demand of the circuit, it is also important to consider the efficiency of the boost converter operation. Based on the measured performance efficiency as a function of output current, as provided by the manufacturer, the converter efficiency is assumed to be 90%. Therefore, the amount of power required for sensor node operation must account for the 10% loss during voltage conversion. The total required

input power is then obtained by dividing the sensor node power consumption by the converter efficiency.

$$P_{in} = \frac{P_{sensor\_node}}{\varepsilon_{boost}} \tag{30}$$

Based on this condition, the amount of input power needed to operate the sensor node is approximately 118 mW. Dividing the input power by the supply voltage (1.3 V) yields a current consumption of approximately 91 mA. Assuming the input current comes from the buffer capacitor, and further assuming the drain current from the capacitor is constant, then the total time for the buffer capacitor to discharge from 1.3 V is calculated from equation (31) below, where i_{out} is defined as the output current from the capacitor, which is the current demand of the sensor node.

$$dt_{out} = \frac{CdV}{i_{out}} \tag{31}$$

For a buffer capacitor with 100 mF capacitance, the total discharge time is calculated as 1.43 s. That is roughly seven-times the length of operation time than the pre-determined duty cycle of the analog switch gate. However, this does not account for current spikes on device startup, so the total discharge time most likely is slightly less than estimated.

Determining the total charge time for the capacitor requires the knowledge of the source resistance of the cement battery. This was experimentally measured as approximately 150 Ω. A capacitor charges exponentially under a constant applied voltage defined by:

$$V_{charge} = V_{in}\left(1 - e^{-t_{charge}/RC}\right) \tag{32}$$

Solving equation (32) for the charge time (t) results in a logarithmic charge time defined as:

$$t_{charge} = -R_S C \ln\left(1 - V_{charge}/V_{in}\right) \tag{33}$$

Assuming a charge voltage of 1.3 V, and an input voltage of 1.4 V (this can vary depending on Galvanic potential between the anode and cathode), the total charge time for the buffer capacitor is calculated as approximately 40 s. Applying this charge time to equation (31) will determine the output current of the cement battery, which is calculated at 3.25 mA.

The conditions reported in this analysis represent the peak operational duty cycle for the autonomous sensor node operating at max power consumption. The effect of this scenario will be applied to the corrosion dynamics of the cement battery to determine the necessary anode volume (assuming a cylindrical shape) for an operational period of 50 years – similar to that of a large-scale marine structure.

Based on the power demand of the sensor node, the necessary corrosion current required for charging the buffer capacitor was determined. The corrosion current is equivalent to the rate of corrosion of the anode, thus allowing for the application of Faraday's equation of general chemistry [9]:

$$w = \frac{ItM}{nF} \tag{34}$$

where w is the weight of the corroding material [grams], I is the current flow [Amperes], M is the atomic mass for the metal [gram mol^{-1}], n is the number of electrons transferred in the reaction [n = 2 for Mg], and F is Faraday's constant [A s mol^{-1}]. Dividing both sides of equation (15) by the density (ρ) yields an expression for the volume of anode as a function of the current flow and time.

Adjusting the current flow I for the duty cycle for charging the buffer capacitor, and assuming the operational time for the sensor node is 50 years; the necessary anode volume is calculated at approximately 359 cm^3, which is approximately 625 grams. Bulk magnesium is currently priced at $0.29 per 100 grams. Thus, for a sacrificial anode of magnesium operating for 50 years at peak power consumption, the total cost will be approximately $1.82, assuming the entire anodic material is consumed.

A portion of Chapter 3 has been published in IEEE Sensors Journal, Scott Ouellette and Michael Todd, 2013. The title of this paper is "Cement Sea-Water Battery for Marine Infrastructure Monitoring". The dissertation author was the primary investigator and author of this paper.

Another portion of Chapter 3 has been published in Proc. of SPIE, Scott Ouellette and Michael Todd, 2012. The title of this paper is “Ultra-Low Power Corrosion-Enabled Sensor Node”. The dissertation author was the primary investigator and author of this paper.

Another portion of Chapter 3 has been published in Proc. of SPIE, Scott Ouellette and Michael Todd, 2013. The title of this paper is “Uncertainty Quantification of a Corrosion-Enabled Energy Harvester for Low-Power Sensing Applications”. The dissertation author was the primary investigator and author of this paper.

Chapter 4

Introduction to Vibration Energy Harvesting

There is a widely accepted notion in vibration energy harvesting that the assumptions of stationary and narrowband input excitations are insufficient for modeling real world environments. Brian Mann presented an uncertainty analysis of vibration energy harvesters operating in a linear regime [4]. He starts his analysis with a generic dimensionless 2nd –order differential equation for a 1DOF linear oscillator under harmonic forcing.

$$x'' + \mu x' + x = \Gamma \sin(\eta\tau) \tag{35}$$

After assuming a harmonic solution for $x(\tau) = r\cos(\eta\tau - \varphi)$, an expression for the response amplitude (r) can be obtained:

$$r = \frac{\Gamma}{\sqrt{(1-\eta^2)^2 + \mu\eta^2}} \tag{36}$$

The author notes that the output power of a linear energy harvester is proportional to the response amplitude. Next, quantifying the uncertainty in the response amplitude as a function of the dimensionless system parameters (μ, η, Γ) is performed by determining the L2-norm subject to 95% confidence levels in the parameters uncertainties:

$$U_r^2 = \left(\frac{\partial r}{\partial \mu}\right)^2 U_\mu^2 + \left(\frac{\partial r}{\partial \eta}\right)^2 U_\eta^2 + \left(\frac{\partial r}{\partial \Gamma}\right)^2 U_\Gamma^2 \tag{37}$$

The result of this uncertainty analysis "highlights a lack of robustness in achieving a peak response since even small parameter variations or uncertainty can cause large differences in the expected response". A plot of the response amplitude versus the forcing frequency is shown in Figure 32 with the confidence intervals overlaid for reference. A cursory inspection of the confidence bounds generated by the uncertainty analysis illustrates the issues with linear inertial generator designs, in that achieving a resonant response for conventional inertial generators is highly susceptible to small parameter variations.

As such, the linear inertial generator designs are no longer considered practical for field operations in which ambient vibrational energy is predominantly low frequency, non-stationary, and broadband. In order to improve the capability of vibration energy harvesters for deployment, researchers have started investigating methods for developing inertial generators with broadband resonance characteristics. Several techniques for extracting energy from broadband and random excitations have been investigated. These methods are classified by

their approach into three categories: frequency tuning, multi-modal energy harvesting, and nonlinear energy harvesting. In this section, each method is described in detail with regards to their conceptual design idea, the frequency response and power characteristics, and their applicability to field operations.

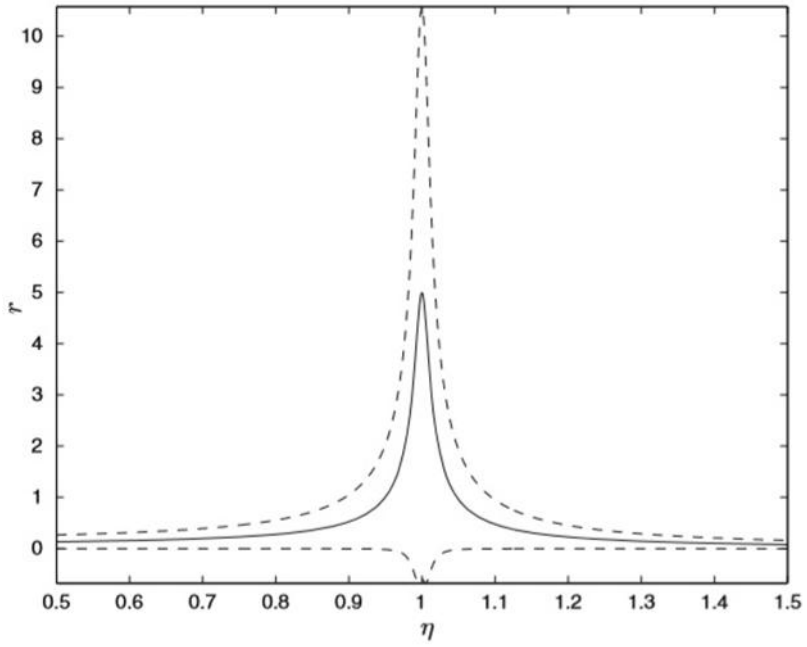

Figure 32. Uncertainty analysis of response in linear oscillator (Source: Mann [83])

4.1.1. Resonant Frequency Tuning

A priori knowledge of the excitation frequency is necessary for defining the geometric, elastic, and mechanical properties of a linear resonant inertial generator. When the excitation frequency is non-stationary, broadband, or unknown, the performance of a linear resonant energy harvester is sub-optimal as the output power of the device decreases significantly if not excited at, or near, resonance. The conventional practice for linear energy harvester design recommends a resonant frequency tuning mechanism to improve the performance functionality.

Roundy and Zhang [6] assert that the resonant frequency of a linear inertial generator can be tuned in either an active mode or passive mode. Active resonant tuning is characterized by continuous, real-time control of the energy harvesting device in order for the system natural frequency to match the excitation frequency. With passive frequency tuning, intermittent adjustments are applied to the energy harvester for frequency matching. A further level of classification for frequency tuning methods exists for systems that are either self-tuning or require manual tuning.

Manual tuning, while requiring relatively less power, is difficult to implement in the field as it requires physical interaction with the energy harvesting device. In this manner, it is best classified as a sub-category of passive tuning methods because once the device is tuned, the system resonant frequency remains set until the next tuning procedure. On the other hand, self-tuning schemes can potentially span the expected excitation frequency range without the need for intervening maintenance. Self-tuning resonant frequency vibration energy harvesters can be categorized as either active (control electronics are required to tune the resonant frequency in real-time) or passive, in which system parameters vary under forcing conditions causing a resulting change in stiffness or mass. The challenge of implementing an active self-tuning approach is to mitigate the power required for the tuning mechanism in order to generate a net-positive power output.

Frequency tuning methods can be are classified based on two metrics: 1) the method in which the system natural frequency is adjusted, and, 2) the dynamic range of resonant frequency of the method (tunability). These methods are classified as mechanical, magnetic, and piezoelectric resonance tuning. Mechanical frequency tuning is generally accomplished by manually adjusting the structural properties of the energy harvesting device, such as the center of gravity of the tip mass, or the mechanical preload. Magnetic tuning employs the use of

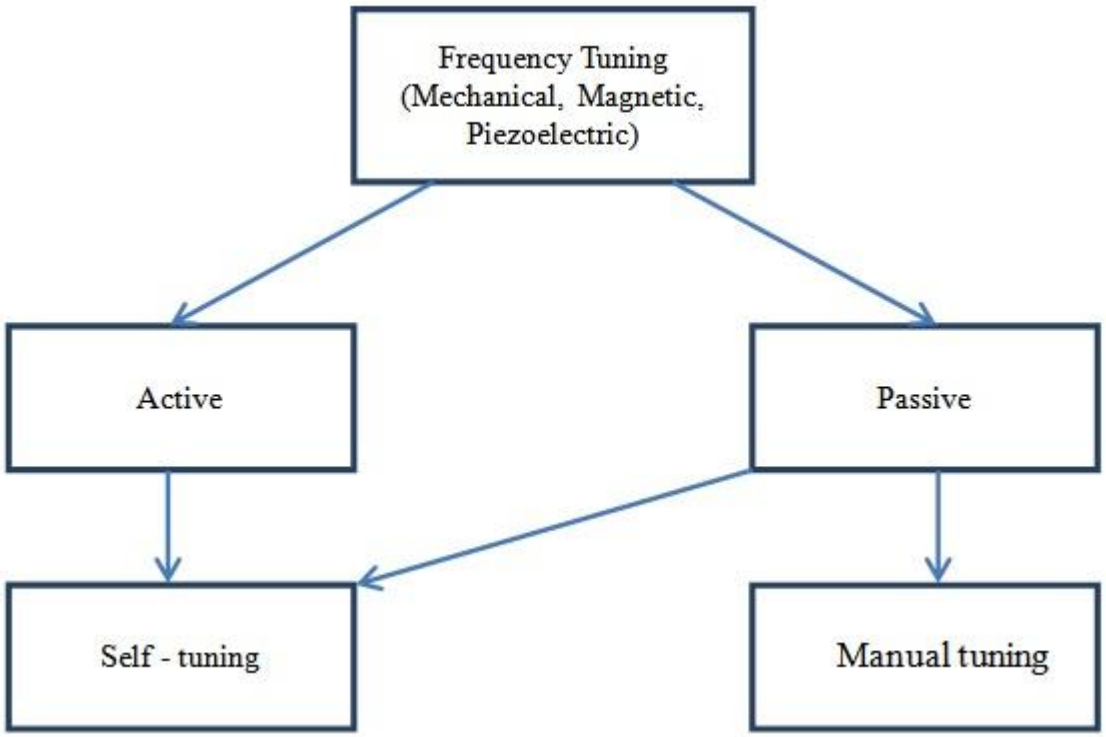

Figure 33. Diagram of frequency tuning methods

magnetic interaction forces to vary the restoring force (stiffness) of the device either actively or passively. Lastly, piezoelectric resonance tuning utilizes part or all of a bonded piezoelectric patch as an actuator to control the beam response to remain at resonance. The rest of this section is dedicated to summarizing literature related to frequency tuning methods for broadband vibrational energy harvesting. Specifically, research associated with each method will be reviewed based on the technique used, specific results provided, and how the method compares to the linear system results – if applicable. Some general observations regarding the three frequency tuning energy harvesting methods reviewed are as follows:

Mechanical frequency tuning approach

- In general, mechanical tuning methods generate the most bandwidth relative to the other methods
- With the exception of two proposed devices [84], [85], most methods reported require manual tuning, which diminishes the overall adaptability to operational deployments
- Since most methods require manual tuning, the amount of energy required for each tuning process was not quantified or reported

Magnetic frequency tuning approach

- Moderate tunability was achieved using external magnets
- Linear actuators were used to adaptively tune the harvesters, however, most reported designs powered the actuators externally
- The designs that did implement self-tuning mechanisms required significant time to gather enough charge for a tuning cycle [86]–[88], and thus, are only applicable for environments in which excitation frequency changes slowly and infrequently

Piezoelectric frequency tuning approach

- Of the three methods presented, piezoelectric frequency tuning features the lowest tuning bandwidth, but also requires the least amount of energy for tuning
- Most convenient for tuning applications because piezoelectric transducer can act as both the energy harvester and actuator

- The energy required for active tuning applications, as reported by the authors [89], [90], outweighs the energy captured by the harvester

Mechanical Tuning Methods

The concept of mechanical resonant frequency tuning stems from elementary vibration theory, in which the natural frequency of a linear system is a function of its stiffness and mass. Since the mass of a system is a bulk property, it is more commonplace to make alterations to the stiffness. This can be accomplished in several ways, the most effective of which is through manipulation of boundary conditions. Initial investigations in altering system stiffness involved the application (experimental or theoretical) of an axial load to either a simply-supported or cantilevered energy harvester [3–5]. Leland and Wright [91] demonstrated 24% reduction in resonant frequency when applying a compressive axial preload to a simply supported bimorph energy harvester with a mid-span proof mass (Note: since the axial load was only compressive, the resonant frequency shift was unidirectional). An interesting effect of the compressive preload was the increase in damping ratio with increased axial load. This damping effect worked opposite the decrease in resonant frequency, and thus resulted in slightly lower output power for lower resonant frequencies. They concluded with noting the energy harvester generated between 300-400 μW when excited in a frequency range of 200-250 Hz with a 1 g acceleration. Similar to Leland and Wright, Eichhorn et al. [92] investigated the effects of an axial prestress on the tip of a cantilever beam. Once again, damping was shown to increase with the axial load applied to the free end of the beam, and resulted in reduced power output at lower frequencies.

An analytical investigation of mechanical tuning of resonant frequency by axial preload was conducted by Hu et al. [93]. In their approach, the governing equations of motion were

derived for a general axial load (compressive or tensile), and the resonant frequency characteristics were studied as a function of the applied load. A resonant frequency range of 58.1Hz – 169.4 Hz was calculated for applied axial loads of 50 N, in compression and tension, respectively.

Other than exploiting the bending mode of abeam, several studies have been conducted where an axial/extensional mode is exploited [6, 7], or the pre-deflection of a circular plate [96], or by adjusting the center of gravity of the tip mass [97]. It is important to reiterate that with the manual tuning approach, the energy harvester is still effectively a linear resonator in each experimental realization. The manner in which the system is considered broadband is through manual intervention, which is sub-optimal in field operations because of associated costs for adjustment, and potential complications with accessing the energy harvesting device.

To address the problem presented with manual tuning techniques, researchers developed passive self-tuning resonant frequency schemes [10, 11]. Jo et al. [85] developed a coupled cantilever system with a moveable mass which generated two distinct operational phases. Passive phase transition occurs as a result of the difference between the horizontal inertial forces between the two beams, as they are fabricated with different cantilever lengths. The moving mass causes each cantilever to exhibit two distinct resonant frequencies, the transition of which is a function of the forcing frequency.

Gu and Livermore [84] designed a passive self-tuning radially-oriented cantilever beam for rotational motion. The rotation is oriented parallel to the gravitational field, and thus the beam experiences continuous variation in loading conditions as a function of the circular path. As the rotational speed varied, the centrifugal forces caused a proportional change in stiffness of the harvester, and thus the device was always working near resonance. The authors

concluded that this passive self-tuning design is particularly well suited for rotating systems with variable rotation speeds – such as tire pressure monitoring devices.

Magnetic Tuning Methods

Aside from altering the mechanical properties of an inertial generator, adjusting the boundary conditions using magnetic forces is another technique that has been investigated for exploiting broadband resonance. Magnetic force interaction can be useful in influencing the displacement shape of a resonant energy harvester by biasing the stable tip position of a cantilever [12, 13]. By varying the separation distance between the interacting magnets the beam stiffness can be tuned to resonate for various excitation frequencies. A self-tuning approach has been investigated in which the separation distance is controlled by a linear actuator [14–16]. This section will summarize the results and characteristics of magnetic frequency tuning devices. The

Challa et al. [98] explored the tunability of a cantilever piezoelectric energy harvester with permanent magnets bonded to the beam tip with corresponding attracting and repulsing permanent magnets fixed to a support structure. They found that being either using an attracting or repulsing magnetic force, the resonant frequency of the energy harvester could be shifted lower or higher, respectively. One experimental concern with this design is the possibility of attracting magnet contact. This can be avoided by optimizing the magnetic separation distance relative to the beam bending stiffness. This device achieved an operational frequency bandwidth of 40% over the range from 22-32 Hz, while producing 240-280 μW from an input acceleration of 0.8 m/s^2. The estimated energy for tuning the magnetic separation distance of 3cm was estimated at 85 mJ.

It should be noted that the implementation of magnetic force interactions results in a nonlinear restoring force, and thus the system response exhibits hardening or softening spring characteristics – this will be addressed in more detail in the Nonlinear Energy Harvesting section. Reissman et al. [99] used magnetic attraction to generate a nonlinear monostable potential to try and generate a broadband response. The degree of nonlinearity was variable based on the magnetic separation distance, which was controlled by a thread rod with locking nuts. The total bandwidth of this device was measured as 11.38 Hz, between the excitation range of 88 – 92 Hz. The addition of a tip mass reduced the resonant frequency, but while simultaneously sacrificing resonance bandwidth.

As was the case for manual tuning of mechanical properties of an energy harvester, the overall system response has a single resonant frequency for each experimental realization. Magnetic self-tuning schemes have been investigated for the purposes of adaptively setting the resonant frequency of an energy harvester to capture as much broadband input energy as possible. The methods proposed by Zhu et al. [86], Ayala-Garcia et al. [87], and Challa et al. [88] feature a "smart" controller setup whereby the power needed for the control hardware is generated by the energy harvester.

The harvesters system proposed by Zhu et al. and Ayala-Garcia et al. is a similar setup to the Reissman apparatus in which magnetic attraction forces tune the resonant frequency of the structure as a function of the separation distance. The method proposed by Zhu et al. featured a microcontroller that would periodically measure the output voltage of the energy harvester, and would then send an actuation message to linear actuator to adjust the magnet separation. They calculated the energy cost for controlling the linear actuator as 2.04 mJ/mm, with a total travel distance of 3.8 mm. Though they did not implement a closed-loop control –

the linear actuator was powered by a separate power supply – they estimated the output power of the energy harvester as sufficient for closed-loop control.

Ayala-Garcia et al. improved upon the system proposed by Zhu et al. by: 1) using the microcontroller to detect the phase difference between the excitation source and the harvester tip, and 2) by implementing a closed-loop control. The setup had a total actuation travel distance of 2 mm, which produced 13.76 Hz of bandwidth. It is important to note that since the power for the linear actuator was generated by the energy harvester, the total time between adjustments was dependent on the rate at which the harvester could charge 550 mF super-capacitor. For an input excitation amplitude of 0.558 m/s^2, the charge time for the capacitor was measured at 2 hours. Therefore, in a closed-loop setup, the energy harvester could still be considered a narrow-band resonant frequency inertial generator. The only improvement between this technique and manual tuning is the benefit that it is more pragmatic for field operations as it does not require physical interaction to tune the device.

Challa et al. also implemented a closed-loop self-tuning approach to their previous design [88]. Similar to the scenario with Ayala-Garcia et al. the total time between adjustments for the harvester was measured to be between 72-88 min. They reported an output power of 736 μW – 1 mW, and a bandwidth spanning the range of 13-22 Hz. Though these systems were capable of automatic control, the required energy for executing the tuning process was too costly for the necessary adjustment duty-cycle that would be required in field operations. In conclusion, these designs are really only well suited for scenarios where frequency variation is quasi-stationary and narrowband, though there is room for improvement in reducing the power demand of the control hardware.

Piezoelectric Tuning Methods

The final approach reported in the category of resonant frequency tuning applies strictly to piezoelectric inertial generators. This method takes advantage of the duality of the piezoelectric effect by using the bonded transducer to both harvest vibrational energy and control the resonant frequency of the energy harvester. The stiffness of a piezoelectric material can be varied by placing a shunt electric load across the poles. With this technique in mind, several researchers have proposed designs that utilize the top layer of a bimorph inertial generator to provide power to control electronics that effect the resonant frequency of the harvester [17, 18], or use a portion of a piezoelectric layer by etching a gap in the patch [89]. Since the piezoelectric material is bonded to the energy harvester, the proposed designs are all self-tuning. The only manner in which manual tuning could be performed would be by interacting with the control electronics via a variable resistor (potentiometer) or variable capacitor. However, since the goal of resonant frequency tuning is to improve the practical application of vibrational energy harvesters for field operations, manual tuning should be avoided as best as possible, especially when considering the minimal power cost of switching between electronic components is all that is needed for piezoelectric resonant frequency tuning.

Wu et al. [100] proposed a piezoelectric bimorph cantilever energy harvester in which the top layer is connected to a capacitor network used to tune the resonant frequency through electromechanical coupling. Recalling that tunability is achieved mainly by manipulating the system stiffness, the effect of applying various shunting loads to one layer of a bimorph energy harvester will have a less significant effect on the total system stiffness. Therefore, the total bandwidth achieved by this method is the least when compared to mechanical and magnetic resonant frequency tuning methods. For the proposed design by Wu et al. a total bandwidth of 3 Hz was reported; however, the power required by the microcontroller system was on the μW

scale. Roundy and Zhang [89] demonstrated analytically that the design proposed by Zhu et al. never resulted in a net-positive power output. Furthermore, they fabricated a similar experimental setup, and validated their analytical study by demonstrating a change in output power of 82 μW, with a total power consumption of the controller network of 440 μW. They concluded their analysis by recommending research initiatives in passive tuning mechanisms.

Lallart et al. [101] proposed a design in which one layer of the bimorph was used as a tuning actuator controlled by an external switching voltage source. Their concept of closed-loop control was to detect changes in the excitation frequency and adjust the cantilever beam stiffness accordingly by determining the phase between the beam and base oscillation. The hardware used to accomplish this was an additional piezoelectric sensor near the beam root to measure the deflection, and an accelerometer mounted to the base. The proposed system had an estimated net-positive power output; however, it was only valid near the natural primary resonance of the harvester, and it was only estimated for the maximum power, not the average power. The authors reported the control protocol increased the bandwidth from 4.1 – 8.1 Hz near the resonant frequency of 112 Hz.

Other piezoelectric resonant frequency tuning methods have been proposed for broadband vibration energy harvesting [19, 20]. Peters et al. [90] developed a novel two-actuator system, in which a free actuator swung about a hinge. When a control voltage was applied to the piezoelectric actuators, the resulting shape generated a much stiffer structure (increasing the resonant frequency bandwidth). This design attempted to overcome the inherent issues in generating large bandwidth by piezoelectric frequency tuning by coupling a secondary beam to the system. The result was successful in generating a larger resonant frequency bandwidth (over 30%); however, the power consumption of the tuning mechanism was significantly larger than the generated output power of the harvester. Wischke et al. [102]

proposed a “semi-passive” tuning approach that called for a large tuning voltage (-100 V to +260 V) to be applied across the poles of a piezoelectric bimorph actuator, with a polymer substrate. The resonant frequency energy harvester utilized electromagnetic induction to collect the vibration energy. The control voltage would be applied across the piezoelectric actuators, altering the structure stiffness. However, due to charge leakage in the actuator, the resonant frequency would drift, eventually returning to the natural resonant frequency.

Frequency tuning methods (mechanical, magnetic, and piezoelectric) have demonstrated varying levels of success in increasing the bandwidth of resonant frequency generators for vibrational energy harvesting. Trade-offs between bandwidth, complexity, and the energy required for tuning defines the central theme of implementing these techniques for broadband energy harvesting. Issues with generating a net-positive power output are still to be completely resolved, with many researchers considering the implementation of custom low-power CMOS integrated circuits to serve as the control hardware. The next sub-sections of this review will highlight different approaches to broadband energy harvesting from exploring the multiple oscillation modes of a beam and their contributions to power generation, to exploiting properties of nonlinear vibration theory for high-energy broadband oscillations.

4.1.2. Multi-Modal Energy Harvesting

In the previous section, researchers attempted to design energy harvesters with a variable resonant frequency for the primary bending mode in order to capture and convert broadband vibration energy. This section investigates a different approach to broadband energy harvesting, in which inertial generator designs exploit multiple bending modes in a beam [21–30], or by treating linear resonant generators as an array of pass-band filter oscillators [31–37].

Some general observations regarding the two multi-modal energy harvesting methods reviewed are as follows:

Multiple bending mode approach

- Most designs employ a cantilever beam configuration, with the exception of two clamped-clamped beam proposals [22, 23]
- Typically, only the first two bending modes contribute to the total harvested energy
- Bending mode ratio (ratio between 1^{st} and 2^{nd} bending mode frequencies) is very large for conventional beam designs (M2/M1 > 6) [24–26]; however, novel beam designs can reduce this ratio significantly (M2/M1 ~ 1.17) [21, 29, 30].
- Broadband power output can be achieved, but with the trade-off of adding weight or volume compared to the standard cantilever device [28, 29]

Cantilever array approach

- Most designs use uncoupled / quasi-coupled cantilever arrays, with the exception of two designs that feature spring coupling [113] or tip-mass coupling [114]
- Cantilever tuning accomplished by varying beam length and tip-mass [33, 35], or piezoelectric transducer thickness [116]
- More complex interface circuitry is required to account for phase differences between tuned cantilevers [36, 37]

- Bandwidth can be modified through electrical connection (series or parallel) between tuned cantilevers [116]
- Cantilever array can be scaled-down to MEMS devices using either piezoelectric [118] or electromagnetic induction [119]

Tadesse et al. [106] presented a hybrid piezoelectric / EMI multi-modal vibration energy harvester that exploited the first two bending resonances of a cantilever beam subject to base excitation. The device used a permanent magnet as the tip mass which would pass through a coil of wire for electromagnetic induction. The authors reported the device harvested more energy through the EMI interface for the primary bending mode, whereas the piezoelectric transducers harvested more energy in the secondary mode. One complication with this approach is with matching the electrical impedance of the two different transduction methods for optimal energy capture / storage. Furthermore, this device had a very large reported mode ratio of 18 (20 Hz and 300 Hz, respectively), effectively rendering the system to be discrete.

Ou et al. [25] performed a theoretical analysis of a similar two-mass cantilever device and found similar issues with the mode ratio being so large that the energy between modes is minimal, and thus fails to capture broadband energy. They later experimentally validated their model results [108]. The issue with mode separation is that the excitation bandwidth often fails to exhaust the frequency space between the two modes. Furthermore, the response between modes drops-off significantly if their mode ratio is too large.

To address the problem or modal separation, researchers began to develop novel beam-system designs to increase the modal density within a reasonable excitation frequency band. Arafa et al. [109] proposed a novel 2DOF cantilever energy harvester with a “dynamic magnifier”. This design reduced the mode ratio to approximately 2.5, while increasing the

harvested power by a factor of 13 over a conventional cantilever harvester. One noted tradeoff in their design is the added mass required by the dynamic magnifier, which could be prohibitive in applications where device weight/volume is critical.

A variation on the 2DOF cantilever approach was proposed by Erturk et al. [103], where they investigated an L-shaped bimorph cantilever. Depending on the tuning parameters (beam length, mass ratio/location) a mode ratio of 2 was achievable. Interface electronics issues persist with this design as a result of mode-shape-dependent voltage cancelation. The authors ultimately suggest further investigation into more complex circuitry to improve the harvested voltage.

Further reducing the mode ratio, Berdy et al. [111] and Wu et al. [112] investigated novel cantilever beam designs which could provide increased modal density with only minimal increase in device volume. A cantilevered meandering bimorph with distributed proof mass was demonstrated by Berdy et al. to exhibit a broadband output power response over a range of 32.3 – 45 Hz. The reported mode ratio for this device was approximately 1.31, with bending resonances at 33 and 43.3 Hz, respectively. The device by Wu et al. featured a more compact and efficient variation on the 2DOF harvester with a dynamic magnifier proposed by Arafa et al. by nesting a second cantilever beam within a primary cantilever beam. This device allows the tip mass on the primary cantilever to act as the dynamic magnifier for the secondary harvester, with the beam parameters selected to achieve a reported mode ratio of approximately 1.17.

Instead of exploiting multiple bending modes of a single cantilever beam, researchers took the approach of using an array of tuned cantilever energy harvesters as a mechanical pass-band filter bank for broadband energy harvesting. Most designs proposed in this approach feature an array of uncoupled/quasi-coupled cantilever beams each tuned to a specific

resonance frequency through tailor mechanical parameters such as length [115], tip mass [117], or piezoelectric bimorph thickness [116]. Micro-scale harvester designs were also proposed for piezoelectric [118] and electromagnetic induction [119] energy harvesting for ultra-low power electronic devices.

Shahruz et al. [115] first proposed the cantilever array vibration energy harvester design in which individual cantilever beams are quasi-coupled (i.e. share the same input excitation) tuned by their length and/or tip mass to discretely span the input excitation frequency bandwidth, Figure 32. The authors reported this concept as a "mechanical pass-band filter". Xue et al. [116] proposed a similar design with the cantilevers tuned by the piezoelectric bimorph thickness. By tailoring the electrical connection (series or parallel) between tuned cantilevers, the device bandwidth could be adjusted. They found that a series connection of the harvesters resulted in an increased bandwidth, whereas connecting in parallel would provide a shift in the response frequency range. Ferrari et al. [117] investigated the power output characteristics of a 3-cantilever device where the excitation frequency varied from in-band (i.e. exciting one the resonances) and out-of-band. The experiment demonstrated the ability of the design to provide enough power to trigger wireless data transmission in a connected sensor node. The authors reported that for resonant excitation, for any of the 3 cantilevers, the energy harvester could generate enough power to trigger a wireless transmission. For an out-of-band excitation, the cantilever harvesters could not trigger a transmission independently; however, as a complete converter array, the device could achieve twice as many measure-and-transmit operations, even for out-of-band excitation, as any single cantilever under resonant excitation.

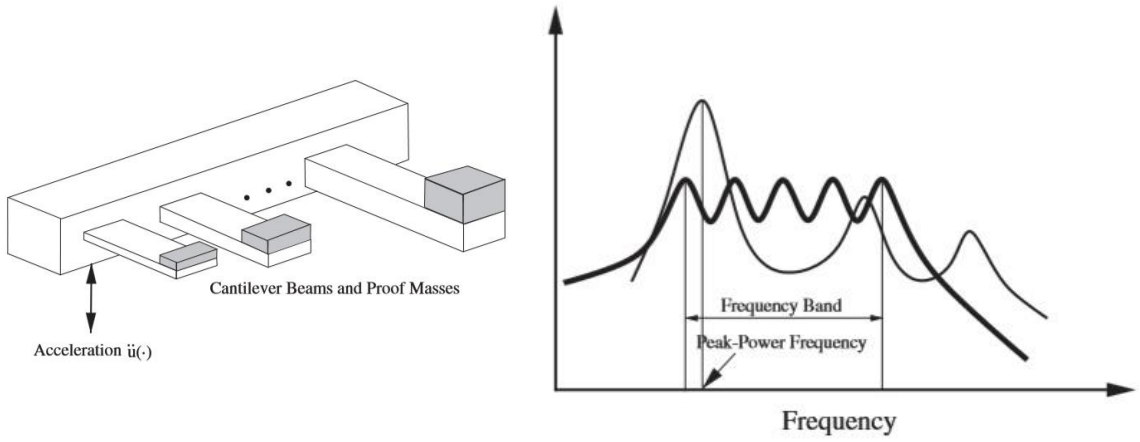

Figure 34. Schematic of cantilever array energy harvester (left) and device frequency response function (Source: Shahruz et al. [115])

Liu et al. [118] and Sari et al. [119] proposed MEMS-scale cantilever array energy harvesters for ultra-low-power wireless sensor networks using the piezoelectric and electromagnetic induction methods, respectively. Liu et al. reported reduced output voltage effects resulting from phase differences between tuned cantilevers. They proposed individual rectifiers for each tuned cantilever to optimally capture and store the output voltage. While this approach did improve the captured output voltage, the complicated rectification circuit could potentially cause significant energy loss for low-level or out-of-band excitations. Sari et al. fabricated a MEMS-scale array consisting of 35 serially connected tuned cantilevers which harvested energy via electromagnetic induction. The authors reported significantly less harvested power than the device proposed by Liu et al., even with cantilevers on a similar scale. This result is consistent with the issues with scaling efficiency of electromagnetic induction harvesters reported by Beeby et al..

4.1.3. Energy Harvesting from Nonlinear Oscillations

As was addressed at the beginning of this chapter, energy harvesters operating in a linear regime lack the necessary robustness to parameter variation (e.g. excitation frequency, damping, etc.) for field operations. To better define the difference between linear and nonlinear configurations, it is instructive to review the generic dimensionless equation of motion for a 1DOF oscillator (equation 35). Here we define a nonlinear energy harvester by the potential energy of the restoring force. This is a geometric-type nonlinearity that can be created through careful design of boundary conditions. Rearranging equation 35 to express the response acceleration as a function of the gradient of the potential energy ($\partial U(x)/\partial x$), viscous damping (μ), and generalized forcing (f(t)), we can see the system nonlinearity depends on the potential energy function (assuming linear forcing). Note, ()' denotes derivation with respect to time.

$$x'' = -\frac{\partial U(x)}{\partial x} - \mu x' + f(t) \tag{38}$$

Equation 38 defines a general 1DOF forced oscillator with viscous damping. It is important to recall from Chapter 1 that an additional electromechanical coupling term (and equation) is required if piezoelectric energy harvesting is used; otherwise, as is the case for electromagnetic induction, the coupling effects can be added to the viscous damping term. Researchers have primarily focused on Duffing-type nonlinear potential functions for broadband energy harvesting purposes. Duffing's equation, equation 39, is a two-parameter quartic polynomial that can exhibit three qualitative characteristics depending on the sign of the two parameters, as seen in Figure 35.

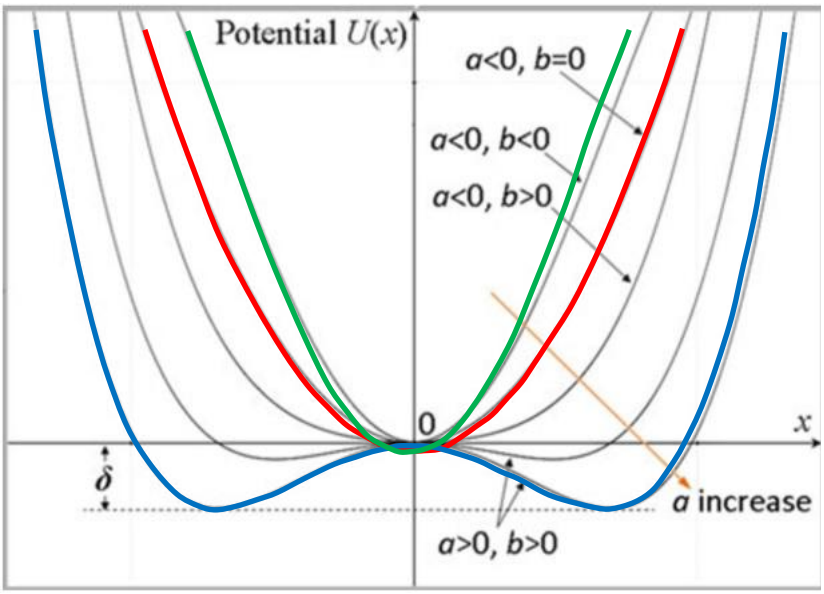

Figure 35. Realizations of Duffing's equation for varying parameter values

$$U(x) = -\frac{1}{2}ax^2 + \frac{1}{4}bx^4 \tag{39}$$

The manner in which these nonlinear potential functions are introduced to the energy harvesting system is mainly by manipulation of boundary conditions. Such a design was highlighted earlier, where researchers were using magnetic forces to tune the resonant frequency of cantilevered piezoelectric beams [99].

Another type of nonlinearity investigated for broadband energy harvesting is introduced by a piecewise linear stiffness through the implementation of a mechanical stopper. In these systems, cantilever beam bending stiffness increases step-wise when it contacts a mechanical stopper, which induces additional strain to the system.

Some general observations regarding the nonlinear energy harvesting methods reviewed are as follows:

Monostable Nonlinear Configuration

- Increased bandwidth observed resulting from hardening or softening response, while output power matched [120], or increased [121] relative to linear energy harvester
- Most designs featured bandwidth increase in only one direction (e.g. hardening or softening response) [120], [122]; however, some designs could exhibit both hardening and softening responses depending on a tuning parameter [121]
- Overall, this configuration is only beneficial for frequency sweeps (e.g. slowly evolving periodic forcing)
- No improvement relative to linear harvester under stochastic (Gaussian) excitation [123], and decreased performance under colored Gaussian excitation
- Energy required to perturb system from low-energy orbit to high-energy orbit sometimes required

Bistable Nonlinear Configuration

- Can exhibit improved performance relative to a linear harvester for both periodic and stochastic forcing over a larger bandwidth
- Three types of response oscillations: large-amplitude periodic, chaotic, and large-amplitude quasi-peroidic [124]

Piecewise Linear Configuration via Mechanical Stoppers

- For harmonic forcing, configurations with mechanical stoppers exhibit increased bandwidth for frequency upsweep excitations, while maintaining the same bandwidth as a linear harvester for downsweeps [125]
- Under colored noise excitation, the configuration had increased bandwidth, but generated less power relative to linear harvester
- Provided the environment excitation PDF is known, an optimization procedure was investigated to improve performance; however, the results converged to a weakly-coupled contact nonlinearity [126]
- Overall, this configuration offers no improvement in performance relative to linear harvesters, and thus exhibits the same issues with operational deployment

Ramlan et al. [120] first investigated the potential benefits of a nonlinear restoring force for broadband vibration energy harvesting systems. In their paper, they analytically and numerically investigated the hardening response of a nonlinear harvester under harmonic excitation. The found the max output power was equivalent to a linear system, however with the added benefit of increased bandwidth. It is important to note that their numerical investigations assumed a constant damping force.

Mann and Sims [122] proposed a nonlinear electromagnetic induction energy harvester for magnetic levitation systems. The device used two permanent magnets as nonlinear restoring force boundary conditions working on an oscillating mass. In their study, they found that for low magnitude excitations, the system behaved very similar to a linear energy harvester. However, for large-amplitude excitations, the energy harvester exhibited a hardening response,

thus increasing the device bandwidth. One drawback noted by the authors was the uni-directional increase in bandwidth of the device.

Stanton et al. [121] proposed a piezoelectric monostable nonlinear oscillator that consisted of a cantilever bimorph beam, with fixed permanent magnets near the beam tip. Unlike the previous nonlinear configurations, this device could exhibit both a hardening and softening response depending on the tuning parameter (magnet separation distance). Furthermore, this device demonstrated an improved power output and bandwidth relative to a linear harvester, as opposed to the results presented by Ramlan et al. The authors suggested this could be a result from variable damping force from the magnets, whereas Ramlan's study assumed constant damping force [120].

In all nonlinear energy harvesting applications, it is important to note that for both hardening and softening responses, the high-energy and low-energy orbit solutions result from a bifurcation in the system dynamics. As such, both high and low-energy branches are equivalently stable solutions depending on system parameters such as input excitation frequency and amplitude, boundary conditions, and damping. Transitioning from low-energy to high-energy solutions can be accomplished by providing a perturbation to any one of the system parameters, with the degree of the necessary perturbation dependent on the sensitivity of the system dynamics to each parameter.

The system proposed by Ramlan et al. [120] featured a bistable "snap-through" mechanism consisting of a mass-damper connected to two obliquely-oriented linear springs. Their numerical study predicted an improved performance over a linear energy harvester. Erturk et al. [127] and Erturk and Inman [128] studied the energy harvesting characteristics of a piezomagnetoelastic generator consisting of a bimorph cantilever beam on a ferromagnetic substrate with stationary magnets near the beam tip. The authors demonstrated a large

amplitude response could be attained for off-resonance excitation frequencies. Furthermore, transition from low-energy orbits to high-energy orbits was achieved by providing a perturbing actuation to the piezoelectric transducers; however, the energy required for a single perturbation was not quantified.

Cottone et al. [129] first introduced the nonlinear bistable configuration consisting of repulsing magnets, in which they studied the harvester response to stochastic excitaitons. Their design featured an inverted pendulum with a permanent magnet at the cantilever tip acting as tip-mass, with an oppositely poled stationary permanent magnet. The degree of nonlinearity was a function of the magnet separation distance (Δ). The authors found that for a specific separation distance and noise excitation level, the max harvested power was 4-6 times greater than a quasi-linear regime (i.e. large Δ). Their study concluded the response increased with greater separation of the stable points; however, this came at a trade-off in the jump/snap-through probability resulting from an increased potential barrier (δ).

The bistable device configuration using repulsing magnetics proposed by Cottone et al. inspired similar designs by Ferrari et al. [130], Lin and Alphenaar [131], Andò et al. [132], Stanton et al. [133], and Wu et al. [134], a diagram of which is shown in Figure 36. These papers investigated magnetic repulsion bistability under various broad-spectrum excitations. The general theme from this suite of papers concerns the issue of how to enable the harvester to exhibit the snap-through response (a.k.a. interwell oscillations) over a range of parameters such as excitation amplitude & frequency, damping, and degree of nonlinearity. The most recent paper exploiting this type of bistability was presented by Wu et al. [134], where they augment their original novel 2DOF nested piezoelectric harvester. The system was demonstrated to have improved performance in a monostable configuration when compared to their previous linear 2DOF design and the conventional 1DOF monostable harvester. Continued research into the

modeling of the device is required to determine design guidelines. Further investigations to the bistable mode are also currently in progress.

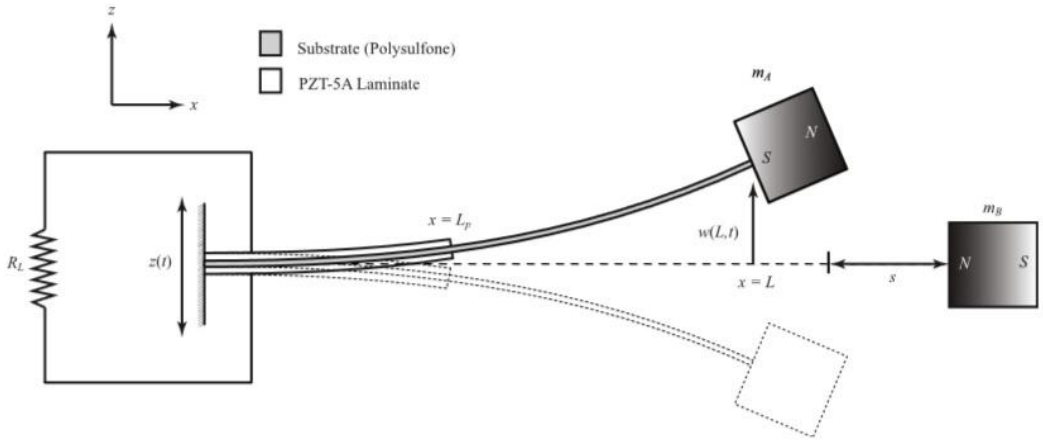

Figure 36. Bistable nonlinear oscillator setup using magnetic repulsion

Fundamentally, the existence of low-energy orbits (a.k.a. intrawell oscillations) is a result of the energy harvester dynamics being unable to overcome the potential energy barrier (the "separatrix") between the two stable states. To address this issue, researchers looked exploit the phenomenon of stochastic resonance, a scenario that arises when the system is forced such that the potential barrier oscillates in phase with the mean transition time between the two stable equilibria [135]–[137]. McInnes et al. [135] studied the manipulation of the spacing between the clamped boundary conditions of a system similar to what was proposed by Ramlan et al. [120]. By actuating the spacing between the spacing of a tuned bistable device, the authors found the energy generated could be significantly greater than the unmodulated system. However, if the system was unturned, then the energy generated was less than the

unmodulated system because the energy required for modulation outweighed the energy captured under active tuning.

Soliman et al. [125] provided a detailed analytical, numerical, and experimental study of a MEMS-based piecewise linear energy harvester with a mechanical stopper. Under harmonic forcing, the device demonstrated improved bandwidth for frequency upsweeps, while showing no change in bandwidth compared to a linear harvester for frequency downsweeps. Their experimental study also showed a lower harvested power compared to a linear device; however, because of the increased bandwidth, the piecewise linear configuration was able to capture 30% more energy over the course of a single frequency upsweep trial.

Blystad and Halvorsen [138] investigated the response characteristics of a piecewise linear device subject to colored noise excitation. Their investigation yielded similar results to Soliman et al. The authors concluded that the overall bandwidth increased at the cost of reduced power output. Soliman et al. [126] then proposed a design optimization procedure for configurations with mechanical stoppers. They were able to determine the harvester performance was dominated by the stiffness ratio and the beam velocity at impact. Their analysis recommended the stopper height should be maximized in order to minimize the contact damping under stochastic excitations, which essentially renders the system to a linear regime. Completing the recent research into configurations with mechanical stoppers, Blystad et al. [139] studied the effects of interface circuits with the performance of MEMS scale harvesters with two-sided mechanical stoppers under harmonic and stochastic excitation. Their simulations demonstrated that for low-amplitude excitations, the effect of interface circuits yielded no performance benefits. For large-amplitude excitations, there was a quantifiable performance improvement for certain interface circuits; however, the power harvested was still less than that of a conventional linear oscillator.

In the next chapter, a new approach to dynamic frequency tuning is demonstrated on an inertial generator which can exhibit multiple response characteristics depending on the amount of current applied to a high-permeability electromagnet interacting with a permanent neodymium magnet

A significant portion of this chapter is to be submitted as a technical report for Los Alamos National Laboratory, Scott Ouellette, Charles Farrar, and Michael Todd, 2015. The title of this report is "Energy Harvesting for Autonomous Sensor Networks." The dissertation author was the primary investigator and author of this paper.

Chapter 5

Broadband Vibration Energy Harvesting via Open-Loop Control of the Bistable Potential Energy Separatrix

In the previous chapter we motivated the need for broadband vibration energy capture techniques to better account for realistic environments in which a remote sensor may operate. As such, the strengths and weaknesses were presented of the various methods previously studied, and it was concluded that harvesting energy from a nonlinear bistable system showed the greatest promise. In this chapter we will present a novel approach to dynamic frequency tuning of an inertial generator by means of tunable electromagnetic repulsion. A 3D SolidWorks render of the proposed Modulated Inertial Generator (MIG) is shown below in Figure 37. The appraoch will utilize a high-permeability electromagnet to generate a user-controlled buckling force within the piezoelectric inertial generator, thus manifesting a dynamic system that can qualitatively alter its dynamic response state from monostable to bistable depending on the direction and magnitude of current flow. In the following sections of this chapter we will present a detailed analysis of the MIG, as well as results from a suite of parametric dynamic tests to verify the hypothesis that precise control of the bistable potential

energy separatrix can result in an augmented broadband resonant response relative to either fixed monostable or bistable configurations.

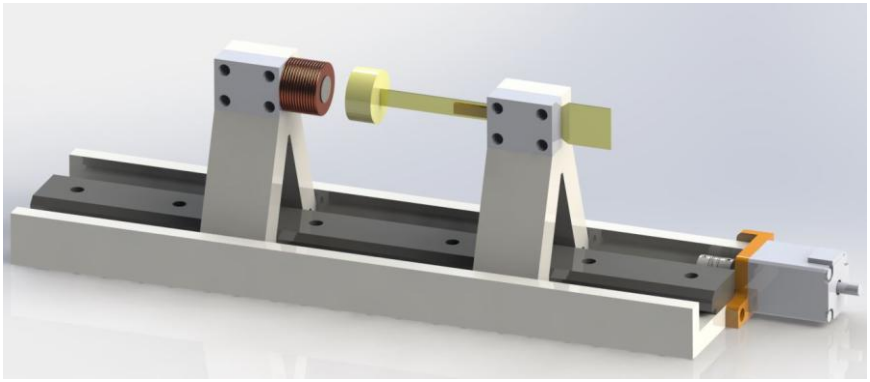

Figure 37. 3D render of MIG experimental setup

5.1. Introduction to Electromagnetism

Prior to deriving the critical buckling load for the inertial generator, it is instructive to first model the force interaction between the two interacting magnets. A vector-gradient method for approximating the force between to interacting magnetic dipoles in free-space was proposed by Yung et al. [140], and later applied to the study of bistable energy harvesters by Stanton et al. [133]. In essence, this approach defines the magnetic potential energy field in the 2D plane as the inner product of the magnetic flux density of the interacting dipole moments ($\mathbf{B_{p\text{-}em}}$) with the stationary buckling magnet ($\boldsymbol{\mu}_{\mathbf{em}}$). With respect to the Cartesian coordinates [$\mathbf{e}_{\mathbf{x}}$, $\mathbf{e}_{\mathbf{z}}$], the magnetic flux density and potential energy are expressed as follows:

$$\vec{B}_{p-em} = \frac{-\mu_0}{4\pi} \nabla \frac{\vec{\mu}_p \cdot \vec{r}_{p-em}}{\left\| \vec{r}_{p-em} \right\|_2^3} \tag{40}$$

$$U_m = -\vec{B}_{p-em} \cdot \vec{\mu}_{em} \tag{41}$$

where, $\|\cdot\|_2$ denotes the Euclidean norm of the position vector. Figure 38 shows a simplified diagram of the interacting magnetic dipoles with respect to the Cartesian reference frame, with the permanent magnet affixed to the beam tip and the electromagnet held stationary. For cylindrical permanent magnets, a first-order approximation of the dipole moment ($\boldsymbol{\mu_p}$) can be expressed as follows:

$$\vec{\mu}_p = \frac{B_r}{\mu_0} \pi {r_p}^2 h_p \tag{42}$$

where B_r represents the remnant flux density of the ferroelectric material after the magnetizing field is removed, μ_o is the permeability of free space, and r_p and h_p are the cylinder radius and height, respectively. A cursory analysis of equation 6 reveals the magnitude of the dipole moment is approximately proportional to its volume and remnant flux density. To fully define the magnetic potential energy, U_m, it is necessary to derive an expression for the dipole moment of the stationary electromagnet.

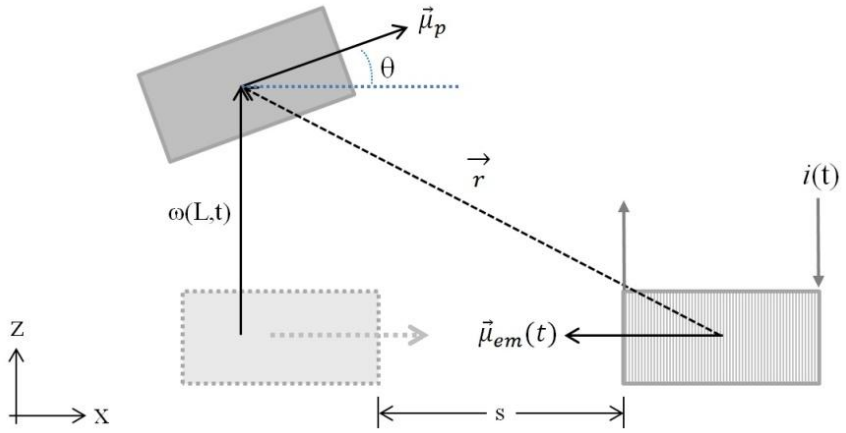

Figure 38. 2D geometric diagram of the magnetic dipole moment interaction

In order to derive an approximate expression for the dipole moment produced by a cylindrical electromagnet, this study employs analytical methods from classical physics in combination with a magnetic circuit modeling approach developed for high-efficiency electrical transformer design. Since the electromagnet used in this study is cylindrical in shape, it is assumed that the dipole moment can be approximated as similar to that of a permanent magnet, with the notable variation being the flux density (B) is a function of the coil current. This assumption is formalized mathematically below in equation (43).

$$\vec{\mu}_{em} = \frac{B(i(t))}{\mu_0} \pi {r_{em}}^2 h_{em} \tag{43}$$

5.2. Derivation of Magnetic Dipole Moment for Cylindrical Electromagnets

In order to derive an approximate equation for the magnetic moment produced by an electromagnet, it is first necessary to review the properties of a solenoid (i.e. an electromagnet

without an iron core). In essence, a solenoid is a wire coil that generates a magnetic field when an electric current is applied. The magnetic field is conventionally described by two parameters, the magnetic flux density (B-field), and the magnetic field strength (H-field). These two fields relate to the electric terminal as follows:

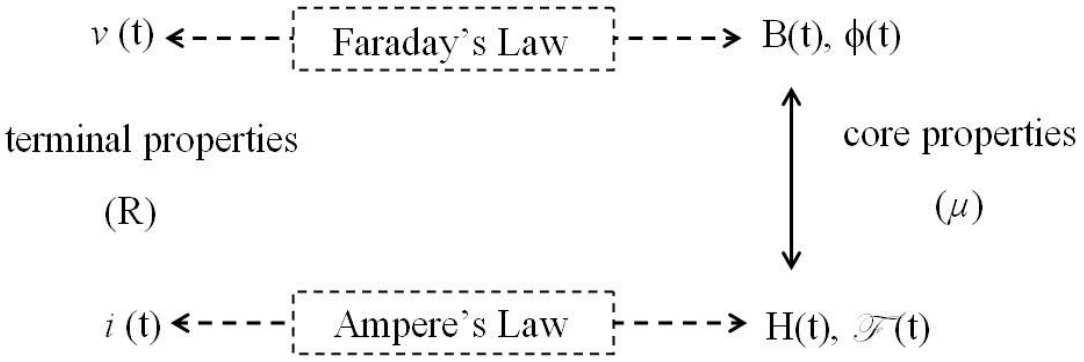

Figure 39. Diagram of electromagnetism relationships

An important conventional note for clarity is that magnetic permeability (μ) is not the same as the magnetic moment (**μ**). For a solenoid, the core is made of air, and thus the two fields are related by the permeability of free space ($\mu_0 = 4\pi \times 10^{-7}$ [N/A^2]). While the permeability for an iron core is much higher allowing for a large **B**-field with little current, the relationship between the two fields is highly nonlinear – an issue that will be addressed later on in this paper.

In this study, all of the magnets will be cylindrical in geometry, thus necessitating the use of cylindrical coordinates when deriving the **B**-field for a solenoid. For an ideal solenoid consisting of a single coil layer that is tightly packed, and infinitely long, the axial (z-direction) component of the B-field is simply:

$$B_z = \mu_0 nI \tag{44}$$

While the field expression becomes much more complicated for a finite length solenoid, there have been several studies that develop closed-form solutions of the respective **B**-fields [141]–[143]. Most recently, Derby and Olbert [143] presented a solution which makes use of the cylindrical symmetry to implement a special case of a generalized complete elliptic integral for determining the radial (ρ) and axial (z) B-field components. Equations 45a,b below are used to describe the axial component of a finite solenoid of radius (a) and length (2b).

$$C(k_c, p, c, s) = \int_0^{\pi/2} \frac{(c\ cos^2\varphi + s\ sin^2\varphi)d\varphi}{(cos^2\varphi + p\ sin^2\varphi)\sqrt{cos^2\varphi + k_c^2 sin^2\varphi}} \tag{45a}$$

$$B_z = \frac{\mu_0 nIa}{\pi(a+\rho)}[\beta_+ C(k_+, \gamma^2, 1, \gamma) - \beta_- C(\beta_-, \gamma^2, 1, \gamma)] \tag{45b}$$

Note, the constants (β±, k±, and γ) are all geometric constants based on the cylinder dimensions. The authors provide a sample code for quickly evaluating the complete elliptic integral, and while this approach is fairly accurate, the equations break-down at the solenoid boundaries (ρ = a, and z = ±b).

5.2.1. Relationship of Coil Current to Magnetic Force

The addition of an iron core to the solenoid has two notable effects: 1) the magnetic field generated per unit of coil current increases greatly due to the alignment of magnetic

domains within the core, making special note that the relative permeability of soft iron cores is in the range of 10^3-10^5, and 2) the field direction is focused within the boundary of the core. Unlike air, an iron core has a finite set of magnetic domains, and thus will saturate. When the magnetizing current is reduced to zero, the iron core still remains magnetized, and thus the material exhibits a hysteretic relationship between the two fields, as shown below in **Error! Reference source not found.**a. It is important to note that once a magnetizing field is applied to the core, it will only return to a de-magnetized state if it is heated to its Curie temperature. For this study, the core characteristics are idealized such that the relationship is piecewise linear, as shown in Figure 40b.

(a) (b)

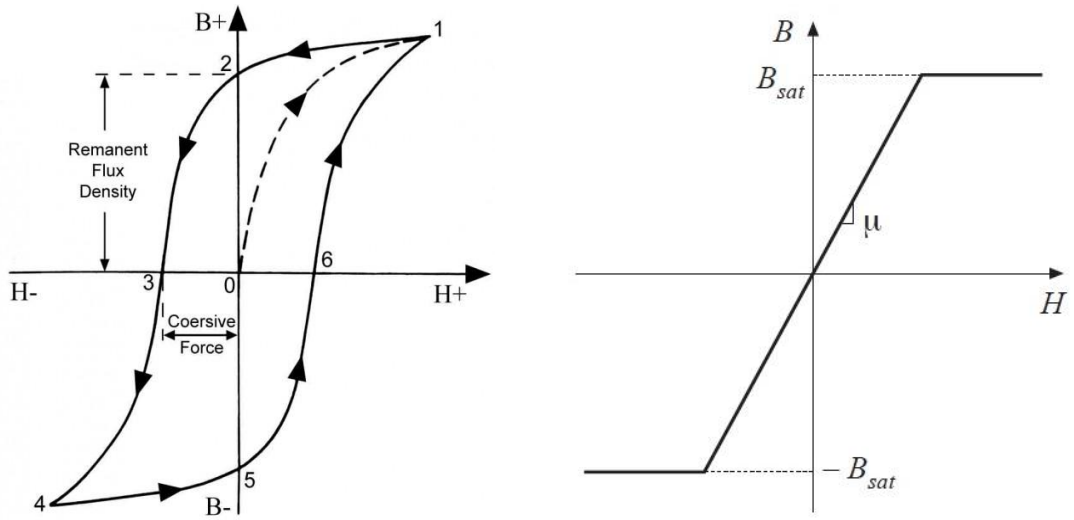

Figure 40. (a) characteristic curve tracing for iron core. At point 0 the material is un-magnetized. Once a magnetizing field is applied, typically via a current carrying coil, the magnetic domains align and the **B**-field saturates at point 1. Once the coil current is reduced to zero, the magnetism in the material domains remain. (b) An idealized, no-loss, core representation used for simple analyses.

Now that a basic foundation for the electromagnet behavior is established, this paper will focus on deriving an approximate expression for the magnetic moment generated by a

cylindrical electromagnet, as depicted below in Figure 41a. To start, this study will assume the magnetization vector, **M**, will be of similar form to the permanent magnet. The restricting condition is that the electromagnet will behave like a permanent magnet when the core is saturated. Thus, the following condition is considered:

$$\boldsymbol{M} = \frac{B_{sat}}{\mu_0} \tag{46}$$

To do this, we must first establish principles of magnetic circuits to account for the effect of the open loop. A fundamental principle of electromagnet analysis is that the magnetic field forms a closed loop from one pole to the other. For a simple toroidal inductor, the path is completed by the core, and thus the field strength, **H**(t), can be assumed to be uniform. The magnetomotive force (MMF), *F(t)*, between two points, x_1 and x_2, is simply the integral of the **H**-field between the points. Thus, for a uniform **H**-field, the MMF is: $F = Hl$, where l is the distance between points. Additionally, the total magnetic flux, $\phi(t)$, is the sum of all flux density vectors through a surface, A_c. Therefore, a uniform flux density through a surface with area, A_c, yields the expression: $\phi(t) = \mathbf{B}A_c$.

Simple application of Ampere's Law to a closed loop inductor – very similar to an electromagnet – shows the MMF is equivalent to the total current in the coil (i.e. $F = Hl = ni(t)$). Assuming the applied current is such that the (idealized) core is saturated, then the following expression holds:

$$I_{sat} = \frac{B_{sat} l_m}{\mu n} \tag{47}$$

Solving equation (47) for the saturation magnetic field, the following expression for the magnetic moment of a closed loop electromagnet as a function of the total current is generated:

$$\vec{\mu}_{em} = \frac{I_{sat} \mu n}{l_m \mu_0} V_{em} \tag{48}$$

It is important to further note that the saturation **B**-field for a soft-magnetic iron core is usually known or provided by the material supplier. While the expression in equation (48) is nice, it does not account for the effect of the air gap on the saturation current. To account for this effect, a simple magnetic circuit model is used. The essential assumptions for a magnetic circuit using an analog of Kirchhoff's node laws are as follows:

- The divergence of **B** = 0;
- Flux lines are continuous with no end;
- Total flux entering a node must be zero;
- The magnetic force and flux are uniform through an element with cross-sectional surface area, A_c (added for completeness)

(a) (b)

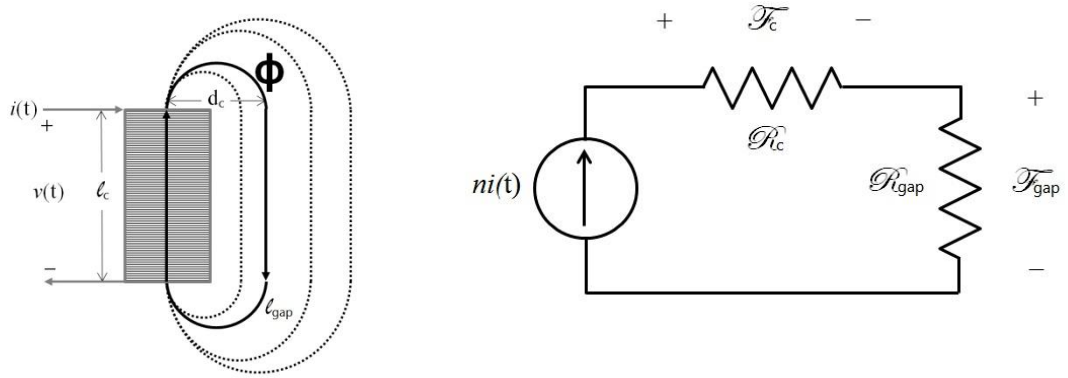

Figure 41. (a) diagram of a cylindrical electromagnet with an assumed magnetic field path (ϕ) shown. (b) an equivalent magnetic circuit accounting for the air gap reluctance, R_{qap}.

Based on these assumptions, the application of Ampere's Law to the magnetomotive force places a restriction that the **H**-field is evaluated over a closed path. Applying the rules listed above to the system shown in Figure 41b, the following expression for Ampere's Law is derived:

$$ni = \phi(\grave{R}_c + \grave{R}_{gap}) \tag{49a}$$

$$\grave{R}_c = \frac{l_c}{\mu A_c} \tag{49b}$$

$$\grave{R}_{gap} = \frac{l_{gap}}{\mu_0 A_c} = \frac{l_c + \pi d_c}{\mu_0 A_c} \tag{49c}$$

Please note, the magnetic path length was calculated as from the center of the iron core and assumes a semi-circular rotation with a diameter equivalent to the core diameter. Applying

equations (49a-c) to equation (46), and assuming a cylindrical electromagnet with an ideal iron core, yields the following expression for the magnetic moment:

$$\vec{\mu}_{em} = \frac{n\pi r_c^2 h_c}{\mu_0 A_c \left(\frac{l_c}{\mu A_c} + \frac{l_c + \pi d_c}{\mu_0 A_c}\right)} \begin{cases} i(t) \;\; for\; |H| < {B_{sat}}/{\mu} \\ I_{sat} \;\; for\; H \;\geq {B_{sat}}/{\mu} \end{cases} \tag{50}$$

Due to the complexity of the calculations, the symbolic manipulation software MATHEMATICA was used to derive the full nonlinear magnetic potential energy. The nonlinear magnetic potential energy function derived in MATHEMATICA using equation 41 is as follows:

$$U_{mag} = \frac{\alpha_0(\alpha_1 \cos\theta + \alpha_2 \cos 2\theta + \alpha_3 \sin\theta + \alpha_4)}{\pi[\beta_0 + \beta_1 \cos\theta + \beta_2 \sin\theta + \omega[L,t]^2]^{5/2}} \tag{51a}$$

where

$$\alpha_0 = 2\left|\vec{\mu}_p\right|\left|\vec{\mu}_{em}\right| \mu_0 \tag{51b}$$

$$\alpha_1 = -2(4a^2 + S^2) + 4\omega[L,t]^2 \tag{51c}$$

$$\alpha_2 = aS \tag{51d}$$

$$\alpha_3 = -4a\omega[L,t]\cos\theta \tag{51e}$$

$$\alpha_4 = S(7a + 6) \tag{51f}$$

$$\beta_0 = 4a^2 + S^2 \tag{51g}$$

$$\beta_1 = 4aS \tag{51h}$$

$$\beta_2 = 8a\omega[L,t] \tag{51i}$$

and $S = 4a + lc + 2s$, where a is the permanent magnet length, lc is the electromagnet core length, and s is the separation distance.

Since magnitude of the potential energy is a function of 4 variables, only specific cross sections of the data can be visualized. Figure 42 shows two such visualizations of the magnetic potential function for various configurations of fixed and variable parameters. Of particular relevance to the bifurcation study is the comparison of the potential energy magnitude for varying spacing and coil current values Figure 42b. This figure shows the highly nonlinear relationship between the magnetic potential and the magnet spacing, whereas, with respect to the coil current, the magnetic potential is roughly linear.

(a) (b)

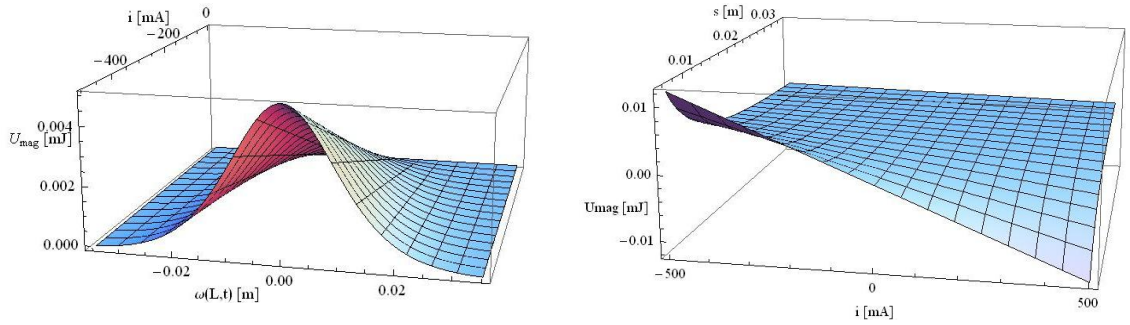

Figure 42. (a) Nonlinear magnetic potential energy for fixed magnet spacing (s = 10.7 mm) and tip rotation (θ = 0), and (b) relationship of potential energy magnitude and for varying magnet spacing and coil current for perfect magnet alignment (i.e. α = 0, and θ = 0).

5.2.2. Electromagnet Power Analysis

A cursory analysis of equation (50) shows the large effect on the air gap significantly increases the saturation current. As such, the required number of coil turns, n, increases greatly to offset the air gap reluctance. However, there are two issues associated with increasing the number of coil turns that lead to diminishing returns: 1) for a finite cylinder height, hc, the increasing number of turns will require coil overlap which results in increased coil diameter, and 2) the increased coil length adds to the parasitic resistance, which thus requires a higher terminal voltage, and higher DC power loss due to joule heating.

For most applications of electromagnets, there are two main sources of power loss: 1) DC copper loss/joule heating, and 2) core hysteresis loss. Since core hysteresis loss primarily occurs during high frequency switching applications, its effects are considered to be negligible in the context of this study. The effect of Joule heating on the power loss is of primary concern in this study due to the manner in which the electromagnet will be employed. Furthermore, in order for this approach to be a viable technique in field operations, its effects must produce a net-positive output power. Therefore, analysis of the primary type of power loss is essential in characterizing the device performance, as well as providing a metric for optimization with regard to design considerations such as material and geometric properties of the ferromagnetic core and wire coil.

The conventional description of Joule heating is to treat the wire coil as a resistor, in which case the power loss is simply I^2Rwire, where the wire resistance for a cylindrical coil can be approximated as:

$$R_{wire} = \frac{4\rho_{wire} d_{coil} n}{d_{wire}^2} \tag{52}$$

where d_{coil} represents the coil diameter, d_{wire} is the wire cross section diameter, and n is the total number of coil turns. The maximum buckling force for a set separation distance becomes limited by the saturation current of the core; thus, the DC power loss in the electromagnet occurs at the saturation current level, which can be determined explicitly via equation (50). Solving equation (50) for I_{sat} in terms of B_{sat} yields the upper bound of the DC power loss:

$$(P_{loss})_{DC} = \frac{\left[B_{sat} A_c \left(\grave{R}_c + \grave{R}_{gap}\right)\right]^2 \rho_{wire} d_{coil}}{n d_{wire}^2} \tag{53}$$

Effectively, the optimal electromagnet design, in terms of minimal power loss, will use a relatively large gauge wire, a high-permeability core material, and a small core diameter. This model does assume a singular layer coil, so there are higher-order layering effects that are unaccounted for in terms of total wire length and magnetic field gap reluctance estimation. Analytically modeling the nonlinear magnetic potential interaction and its effects on the parametric bifurcation space of the inertial generator is the subject of the next section.

5.3. Modulated Inertial Generator (MIG) Buckling Analysis and Modal Model

In order to determine approximate values of interest (e.g., buckling load and natural frequency) for the sections that follow. Additionally, a finite element model was developed to verify the analytical modal model results with regards to the estimated natural frequency for various tip mass values. The inertial generator used in the experimental tests is the V22BL (Midé Corporation) VoltureTM piezoelectric energy harvester. The experimental natural frequency values for various tip masses provided by the manufacturer were used as a means of modal model validation, with the comparison results shown in Figure 45a.

5.3.1. Analytical and Numerical Modal Analysis

The analytical modal model developed to study this inertial generator with an added tip mass follows the procedure outlined by Koplow et al. [144] and Stanton and Mann [145] for beams with step changes in cross section. In this study, the composite beam is parsed into three sections, each with unique bending stiffness properties. Figure 39 shows a layered section of the composite beam stacking sequence, consisting of the four materials that comprise the laminate in a relative scale of their respective thicknesses. To reduce the model complexity often encountered with composite beams, each section is treated as an isotropic prismatic beam, with the elastic modulus calculated as the average modulus for each section in the following manner:

$$E_1 = \frac{E_s A_s + E_p A_p + E_{fr4} A_{fr4} + 4E_e A_e}{A_s + A_p + A_{fr4} + A_e} \tag{54}$$

where, $A_{[]}$ represents the total cross-sectional area of each respective lamina. The specific values used for each lamina are detailed in Table 5. The tip mass was modeled as an isotropic cylinder (non-rigid), with the diameter kept as a variable in order to adjust the overall mass load for the model comparison study.

(a) (b)

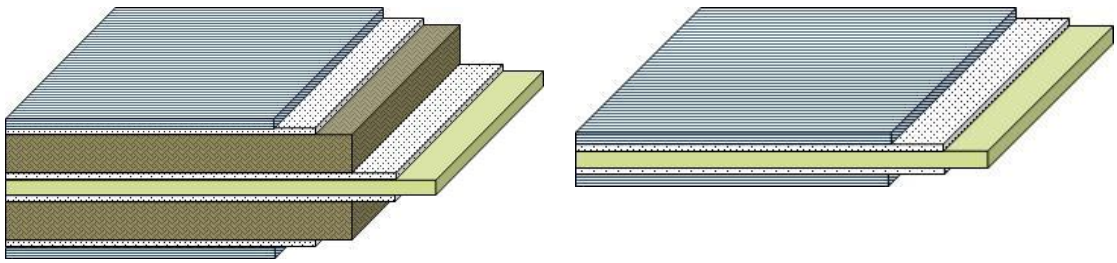

Figure 43. Cross section of composite laminate (a) with piezoelectric layers, and (b) without piezoelectric layers. Note that the diagrams are not to exact scale.

For the finite element model, the beam was again parsed into three sections and modeled using linear-quadrilateral and triangular shell elements, with a mean element size of 1 mm. The only variation between the analytical model and the finite element model is the treatment of the tip mass, in that for the finite element model the geometric properties and moment of inertia were idealized as a distributed mass load on the edge elements. Figure 44 shows the two models.

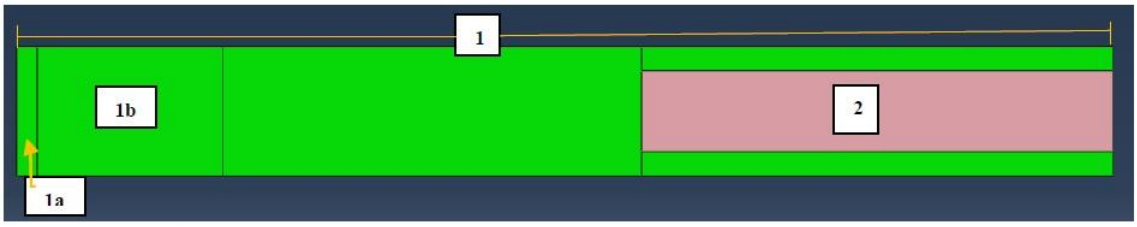

Figure 44. (a) Idealized analytical model of composite inertial generator, and (b) Abaqus finite element model with the piezoelectric layers

Both the analytical model and finite element model assumed an idealized fixed-end condition at the beam root, keeping with the intended application of traditional inertial generator configurations. Comparing the resulting estimations for the primary natural frequency to the experimental values provided by the manufacturer shows each model to have relatively strong agreement to each other, while overall predicting a stiffer beam. However, the models qualitatively predict the asymptotic convergence to a natural frequency of approximately 25 Hz for tip mass values greater than 2 grams, as shown in Figure 41a. For the experimental tests conducted, the tip mass was measured as 5.7 grams, with a measured damped natural frequency of 25.27 Hz. For both models with a 5.7 gram tip mass, the estimated natural frequency was calculated at 25.02 Hz and 26.64 Hz for the analytical and finite element approach, respectively.

(a)

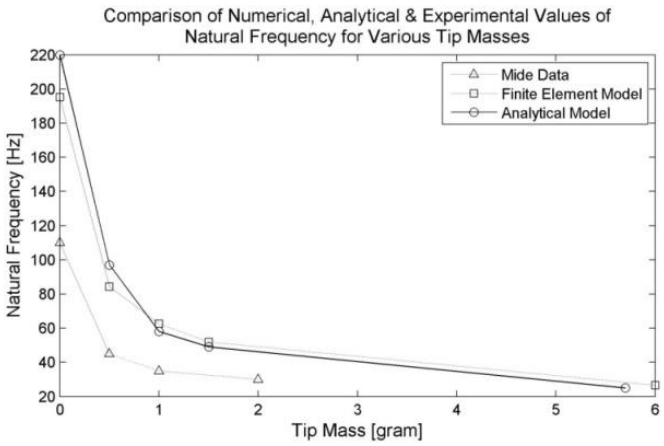

(b)

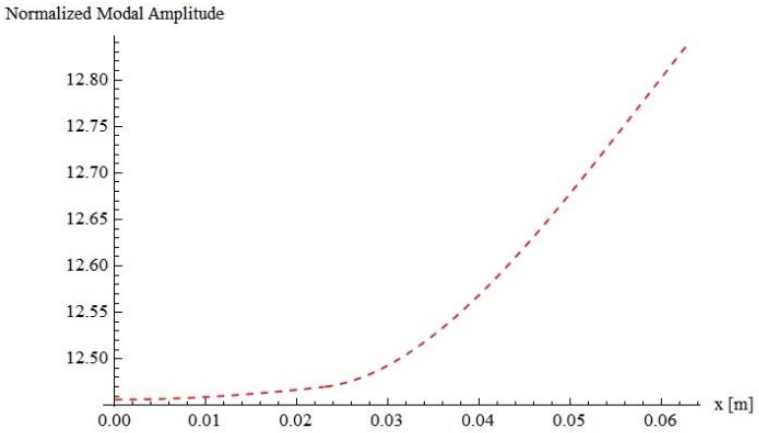

Figure 45. (a) Comparison of analytical and finite element models of the V22BL inertial generator to experimental values provided in the manufacturer datasheet, and (b) the mass-normalized analytical mode shape for the primary bending mode.

5.3.2. Analytical Buckling Analysis

An analytical static buckling model was also derived for the inertial generator independent of the exact description of the magnetic repulsion forces used to generate the nonlinear restoring potential. The insights gained by studying the global buckling of the beam

with an offset eccentricity tuning parameter were instructive in realizing the effective range of mechanical point loads required for generating a bistable potential function. The model approach used in this buckling analysis is nearly identical to the analytical modal model, with the chief difference being the equation of shape due to the presence of an externally applied load as shown in Figure 46.

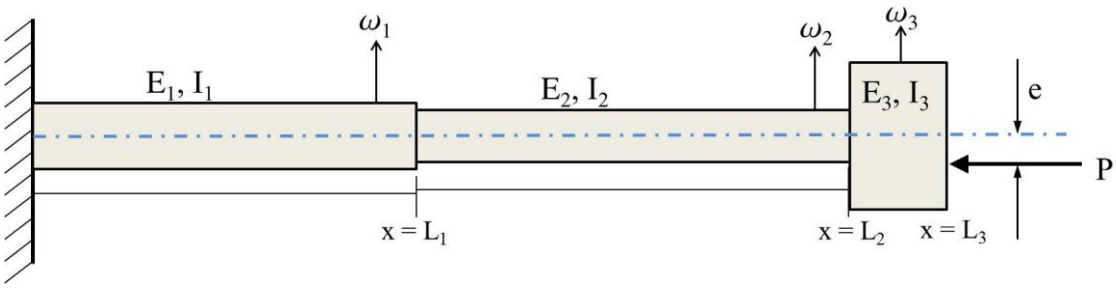

Figure 46. Analytical buckling model with tunable eccentric load

The governing ordinary differential equation for the deformed shape of the beam is as follows:

$$\frac{\partial^4 \omega_i}{\partial x^4} + \lambda_i^2 \frac{\partial^2 \omega_i}{\partial x^2} = 0 \tag{55a}$$

$$\lambda_i^2 = \frac{P}{E_i I_i} \tag{55b}$$

where, λ_i is the non-dimensionalized buckling parameter, and ω_i represents the lateral deflection for each section, with I = 3 sections. Equation (55a) assumes for there are no externally applied lateral loads, and that there are no beam imperfections. A general assumed solution of the form:

$$\omega_i(x) = C_{1i} + C_{2i}x + C_{3i}\sin(\lambda_i x) + C_{4i}\cos(\lambda_i x) \tag{56}$$

is applied with 4 boundary conditions and 8 section-interface compatibility conditions required to satisfy the step-wise tapered beam model. Similar to the modal analysis approach developed by Koplow et al. [144], the displacement, rotation, shear and moment at each section interface must be set equivalent to ensure continuity in the deflected shape. However, since this model includes an eccentric offset parameter (e), a non-zero moment arm manifests at the beam tip, which must be accounted for in the boundary condition. As such, the moment equilibrium boundary condition at the beam tip is as follows:

$$\frac{\partial^2 \omega_3(x = L_3)}{\partial x^2} = \lambda_3^2 e \tag{57}$$

Combining all boundary and compatibility conditions results in a 12x12 matrix set of equations with a non-zero right-hand side resulting from the eccentrically applied buckling load. Inverting the state matrix and solving for all 12 unknown constants will generate an explicit buckling deflection for each beam section.

Since energy is only produced in the inertial generator for strain fields in the piezoelectric layers, this investigation is primarily focused on the buckling loads for section 1. Figure 46 shows the deflection evaluated for $\omega_1(x = L_1)$ as a function of applied load for varying eccentricity values. The critical buckling load for the modeled composite beam, which assumes perfect load alignment by setting the eccentricity value to zero, is calculated as 2.33 mN. Once an imperfection/eccentricity is introduced to the framework, the critical bifurcation

load is no longer an explicit point, and, as such, is generally perceived as the point in which the lateral deflection makes a sharp “knee” bend. Of particular interest in this study is the apparent convergence of eccentrically applied buckling load values. Assuming an experimental misalignment of the magnets of 2 mm will only result in a 5.6% reduction in critical buckling load required to generate the bistability.

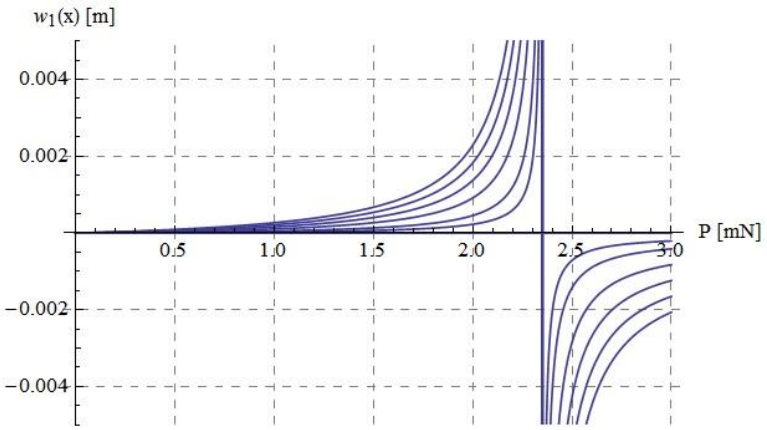

Figure 47. Buckling diagram for piezoelectric beam section as a function of increasing eccentricity (e).

Table 5 below lists all of the geometric and material properties used in the buckling analysis and modal model of the MIG. Manufacturers suggested values for material and elastic properties were used when provided, and estimates for the elastic and geometric properties of the epoxy were made with consultation with the manufacturer. As such, the epoxy material was modeled as having similar elastic properties to Delrin.

Table 5. Elastic and geometric properties used in composite beam analysis

Substrate Properties		
Parameter	Symbol	Value
Modulus	E_s	2.41 Gpa
Thickness	t_s	0.1 mm
Width	b	6.1 mm
Length	L_s	53.16 mm
Density	ρ_s	1290 kg/m^3
Piezoelectric Layer Properties		
Modulus	E_p	63 Gpa
Thickness	t_p	0.254 mm
Width	b_p	3.81 mm
Length	L_p	22.86 mm
Density	ρ_p	7700 kg/m^3
Fiberglass (FR-4) Properties		
Modulus	E_{fr4}	24.8 Gpa
Thickness	t_{fr4}	0.039 mm
Density	ρ_{fr4}	1920 kg/m^3
Epoxy Resin Properties		
Modulus	E_e	1.4 Gpa
Thickness	t_e	2.54 μm
Density	ρ_e	1420 kg/m^3
Tip-Mass Properties		
Mass	m_m	5.7 g
Diameter	d_m	19.05 mm
Length	l_m	9.525 mm
Density	ρ_m	1927 kg/m^3

5.3.3. 2-Parameter Bifurcation Diagram

In order to generate the bifurcation diagram, it is first necessary to evaluate the total potential energy present in the forced inertial generator system. Keeping consistent with the energy description of the system, the elastic strain energy along the axial direction for a prismatic beam is expressed as follows:

$$U_S = \frac{1}{2} E_S I_S \int_0^L [\omega''(x,t)]^2 \, dx \tag{58}$$

where, $E_S I_S$ represents the bending stiffness for an isotropic prismatic section, and $\omega(x,t)$ is the lateral displacement at any point (x) in the beam for all time (t). A common approach for analyzing continuous Euler-Bernoulli beams is to separate the temporal and spatial variables via a modal expansion consisting of a finite sum of orthogonal mode shapes and generalized temporal displacements. By applying a modal expansion of the form $\omega(x,t) = \Sigma\, \alpha(t)\, \phi(x)$, the expression in equation (58) reduces to a simple quadratic function with respect to the temporal displacement parameter $\alpha(t)$.

$$U_S = \frac{1}{2} E_S I_S \Phi \alpha(t)^2 \tag{59a}$$

$$\Phi = \int_0^L \phi''(x)^2 \, dx \tag{59b}$$

where $\phi(x)$ is the composite mode shape developed in section 5.3.1. Since this beam is electromechanically coupled through the piezoelectric layers, it is also necessary to account for the bending enthalpy for each layer within the elastic strain energy formulation. A method for evaluating the bending enthalpy was presented by Stanton et al. and does not require further review with regards to the intent of this investigation [133]. Summing the three potential energy functions gives the total system restoring potential, of which the nonlinear restoring force (Ψ)

can be derived by means of a partial derivative with respect to the generalized temporal displacement $\Psi = \partial U_{total}/\partial \alpha(t)$.

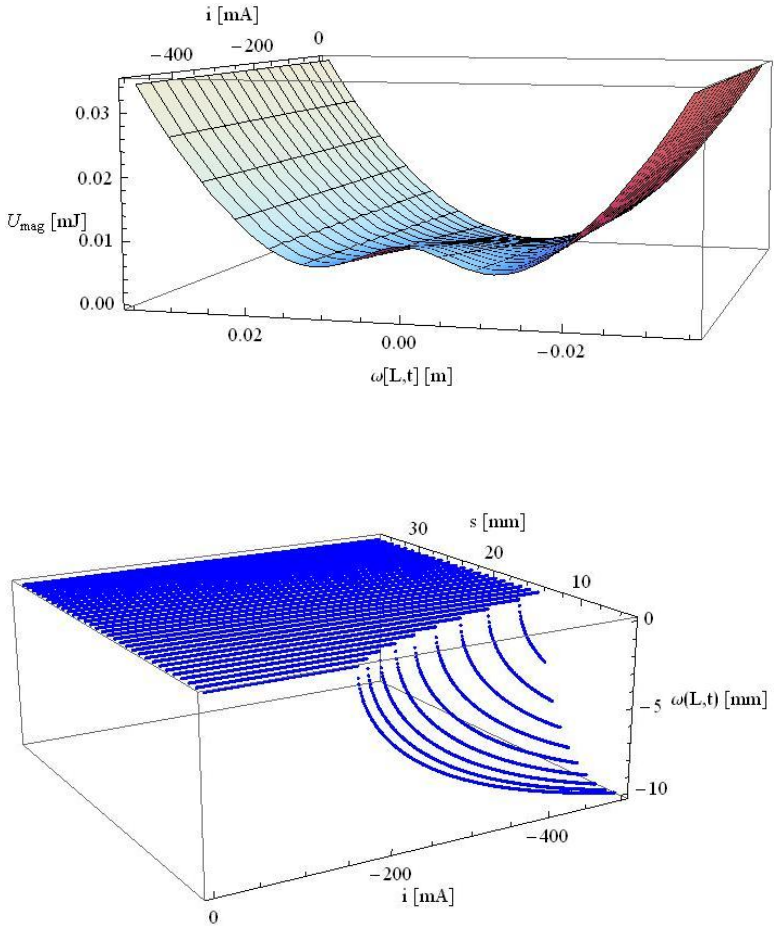

Figure 48. (top) Nonlinear potential energy function with respect to the lateral displacement of the beam tip and an externally applied electromagnet coil current, and (bottom) the 2-parameter bifurcation diagram for various magnet spacing and coil current configurations.

The top image of Figure 48 shows the evaluation of the total potential energy function as the coil current parameter is varied, and in it we see the parabolic function smoothly transition into a bistable potential well system. For a system in which the magnets are initially perfectly aligned, the bifurcation diagram is reduced to a function of two parameters: magnet

spacing (*s*) and coil current (*i*). As such, evaluating the critical points of the nonlinear restoring force (Ψ) for various parametric values of spacing and current yields the 3D bifurcation diagram shown in the bottom image of Figure 48.

Table 6. Properties of tip magnet and electromagnet

Electromagnet properties		
Parameter	Symbol	Value
Core length	l_c	13.8 mm
Core diameter	d_c	9.53 mm
Number of coil turns	n	1000
Core permeability	μ	2.9×10^{6} N/A^2
Permeability of free space	μ_o	4.9×10^{-7} N/A^2
Tip magnet properties		
Length	l_m	4.76 mm
Diameter	d_m	9.53 mm
Remnant flux density	B_r	1.48 T

5.3.4. Model Validation Tests with Laser-Doppler Vibrometer (LDV)

This section describes the experimental tests used to validate the theoretical and analytical models presented in the previous sections. The primary objectives of the tests performed were to quantitatively validate the analytical 2-parameter bifurcation diagram, investigate the bandwidth response of the inertial generator subject to a range of buckling loads, and to confirm the initial hypothesis that the resonant response bandwidth can be augmented by modulating the buckling force in real time during a test.

A picture of the modulated bistable energy harvester experimental setup is shown in Figure 51. As stated previously, the inertial generator used in these experiments is the Midé V22BL. A cylindrical tip mass of polysulfone was fabricated to mount to the tip of the inertial generator, and a 3/8” diameter by 3/16” deep center bore was implemented to embed the permanent tip magnet (D63-N52, K&J Magnetics). A cart and track system was fabricated out

of Delrin to allow for variable magnetic spacing, which was controlled by a stepper motor for accurate spacing tolerances. The electromagnet used is an automotive relay (LD-5F-R, Raylex Elec.) with the protective plastic shell and switch contacts removed.

Figure 52 is a diagram of the experimental setup used to validate the analytical 2-parameter bifurcation diagram. A high resolution Laser-Doppler Vibrometer (OFV 505/5000, Polytec Inc.) was used to measure the lateral displacement of the end mass on the inertial generator. A National Instruments PXI-1042Q data acquisition system was used with LabVIEW to generate the triangle wave excitation signal that cycled from 0-1 A of coil current with a frequency of 0.05 Hz.

A total of 26 trials were conducted over a magnet spacing range of 9 – 36.35 mm, with the results of these tests shown in Figure 53. Comparing the results to the analytical bifurcation diagram in Figure 45b shows a strong quantitative correlation of the initial bifurcation coil current, as well as the spatial dependence. Qualitatively there are two main differences between the analytical and experimental bifurcation diagrams are the result of the modeling assumption of a lossless core material (no hysteresis), and perfect magnet alignment. As seen in Figure 48, there is a clear hysteretic effect on the bifurcation when the current ramps back down from the initial charge.

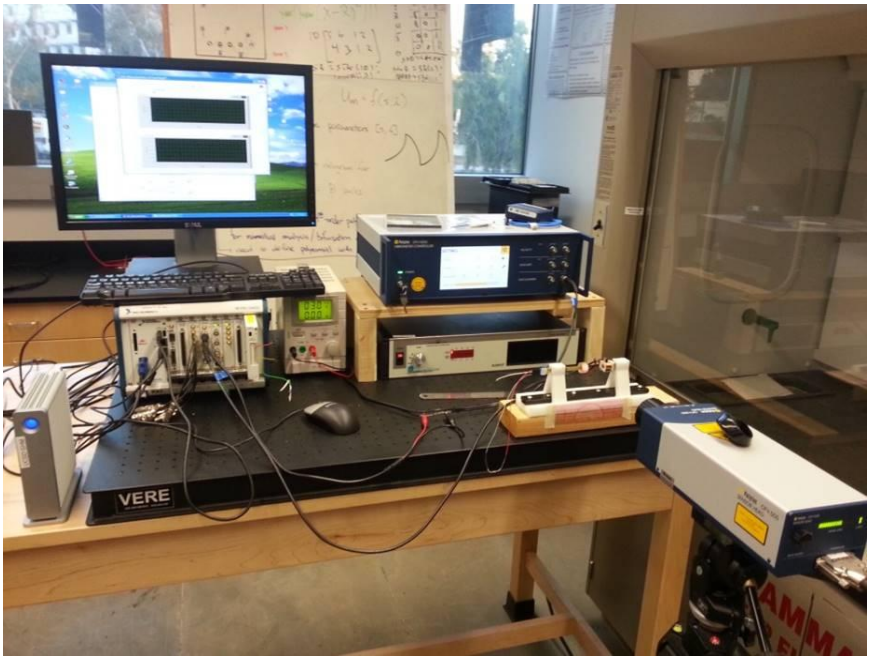

Figure 49. Experimental setup for empirically measured 2-parameter bifurcation diagram

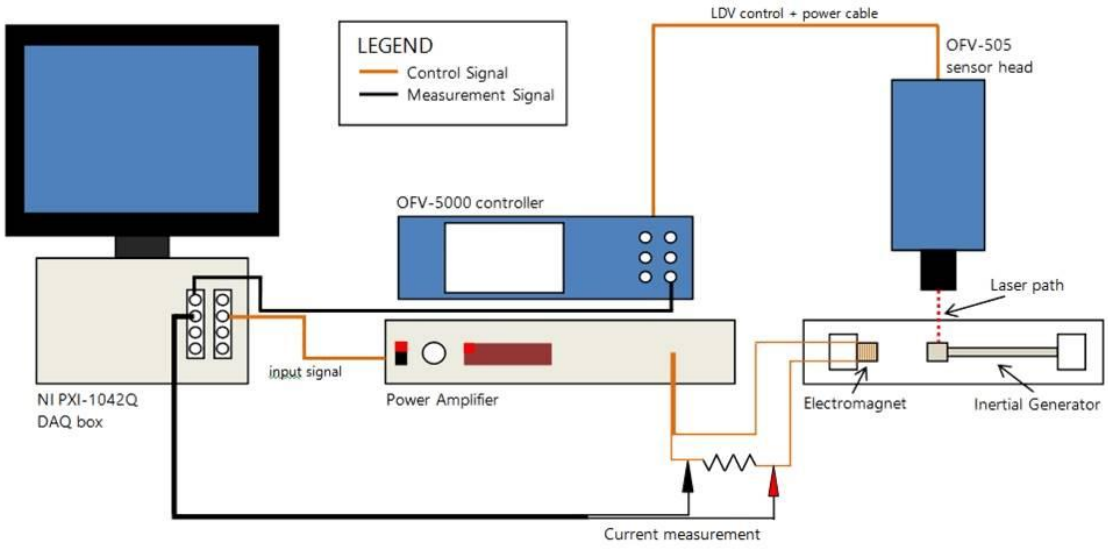

Figure 50. Diagram of 2-parameter bifurcation experimental setup.

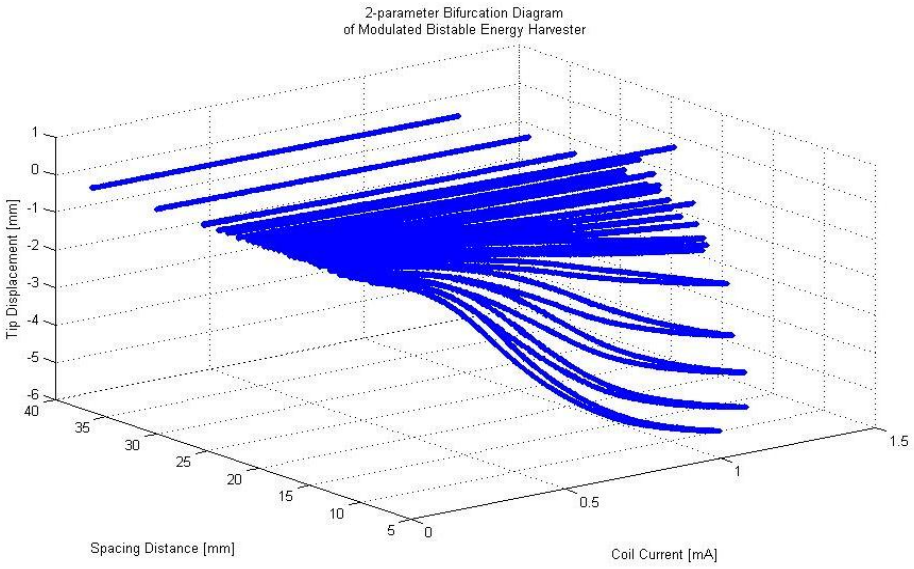

Figure 51. Experimental 2-parameter bifurcation diagram

5.4. Parametric Study of MIG Broadband Resonant Response

This section will review the parametric power output of the nonlinear energy harvester subject to harmonic chirp excitations of amplitude 0.25 g. The parametric study consisted of 40 trials in with the magnet spacing held to a fixed separation distance, and the electromagnet coil current set to a fixed current for the duration of each chirp excitation. Between each trial, the coil current was marginally increased from 0 mA up to a max of 400 mA.

5.4.1. Experimental Setup and Design

The experimental setup for this suite of tests is diagramed in Figure 53. The cart and track system developed for the bifurcation tests was mounted to an electrodynamic shake table, with an NI c-DAQ I/O system used for all control and measurement acquisition. A 1 Ω, 10 W resistor was connected serially to the electromagnet coil to measure the current parameter, and a

68 kΩ, 0.25 W resistor was connected across the external leads of the inertial generator to measure the power output response.

5.4.2. Testing Protocol

The intent of this parametric study was to investigate the full bandwidth of resonant response frequencies for low-amplitude excitations with respect to the nonlinear buckling control parameter. Figure 54a,b shows the power output in the frequency domain for the maximum and minimum electromagnet coil current for up-chirp and down-chirp excitations, respectively. For the up-chirp excitation, a 3 Hz gap in resonance energy exists between the two coil current extrema. Figure 54c,d show that for discrete steps of the coil current, the transition of the resonant frequency peaks is continuous. To that extent, there exists an opportunity to capture vibration energy within an augmented range of frequencies with proper implementation of a control law on the electromagnet coil current.

Further insights into the continuity of the resonant frequency peaks and their relationship to the electromagnet coil current were also required for development of the open-loop control law described in the following sub-section. Figures 54e,f show that for relatively low coil current values, there is a nonlinear shift in the resonant frequency, and for higher coil current values the frequency shift plateaus. This nonlinear relationship is a result of the electromagnet core saturation effect, in which for low values of coil current has a greater net effect on the nonlinear restoring force relative to current modulation when the core is saturated.

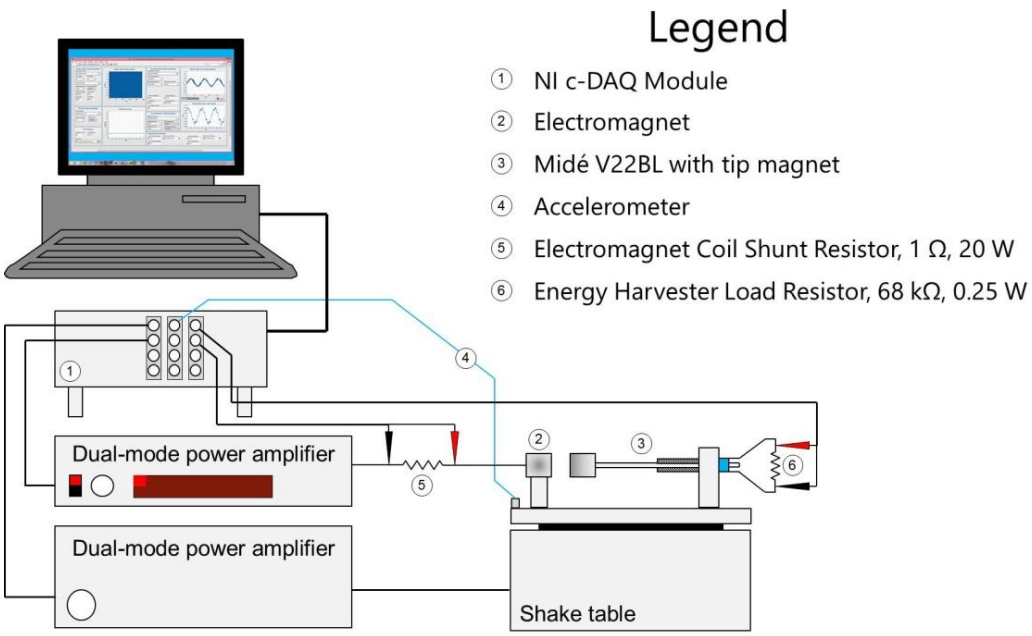

Figure 52. Diagram of parametric study of MIG dynamic response

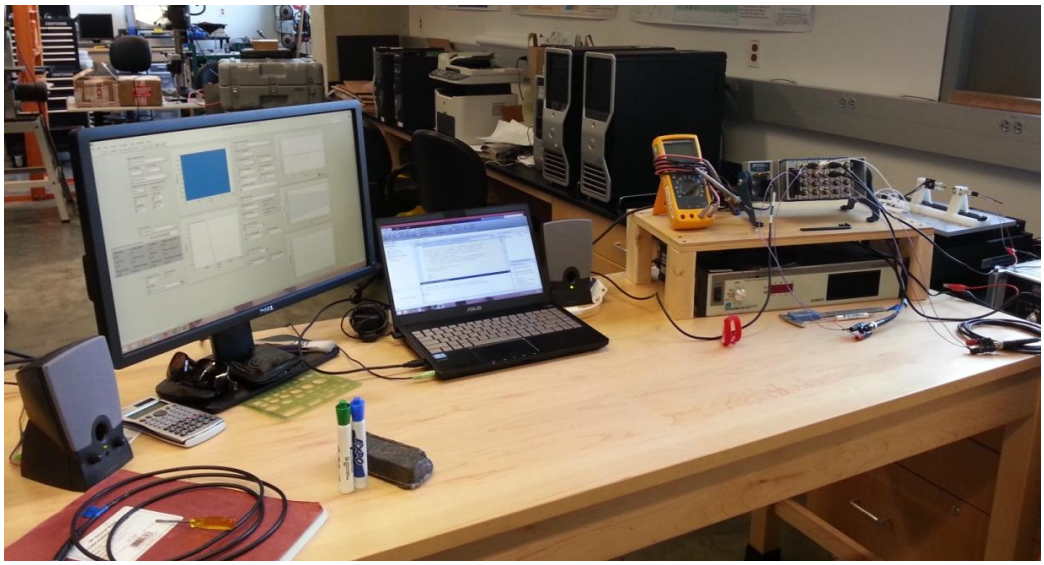

Figure 53. Experimental setup of dynamic tests

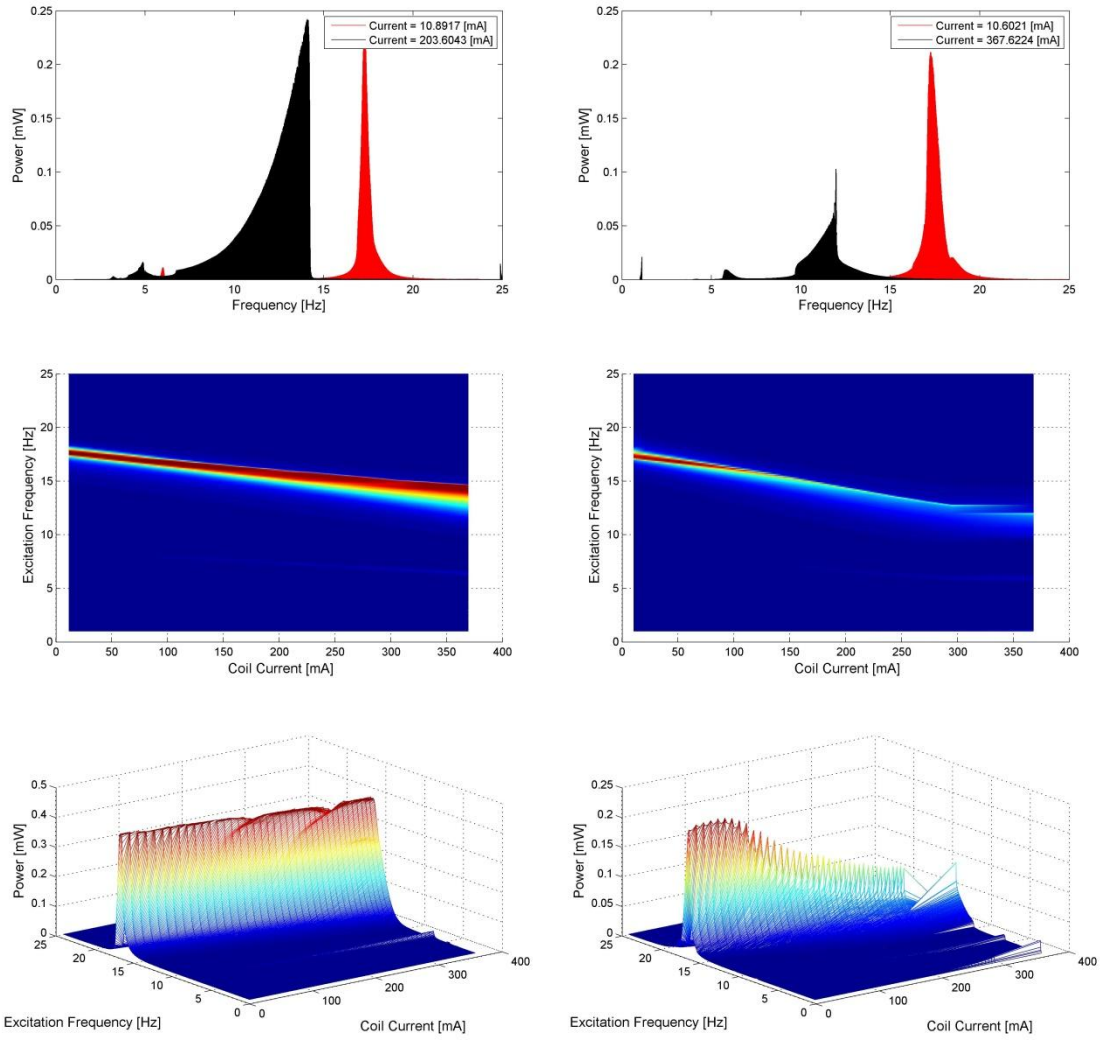

Figure 54. Output power of parametrically controlled inertial generator for harmonically excited chirp excitations

5.5. Open-loop Control of Bistable Separatrix

This section details the design and implementation of an open-loop control law applied to the electromagnet coil in an effort to augment the broadband resonant frequency response of the inertial generator subject to harmonic chirp excitations.

5.5.1. Control Law Development

The open-loop control signal was programmed to linearly modulate the electromagnet coil current in a manner that matches the peak power output across the range of frequencies shown in Figure 54c,d. To accomplish this, the power response signal was enveloped, and the max value was extracted for each trial of the parametric sweep test. Since the measured data was stored as a vector array in Matlab, the index location of the max measured power is directly tied to the excitation frequency in the shake table. Figures 55 and 56 show the peak power points plotted as a function of the base excitation frequency along with an overlaid linear least-squares fit for both harmonic up-chirp and down-chirp excitations. The fitted line was then used as the modulating control signal for the transition region in the chirp excitation tests. While this control approach requires significant a priori knowledge of the parametric power response as the basis for its design, the focus of this initiative is to demonstrate the ability to augment the power output bandwidth by means of external coil current modulation.

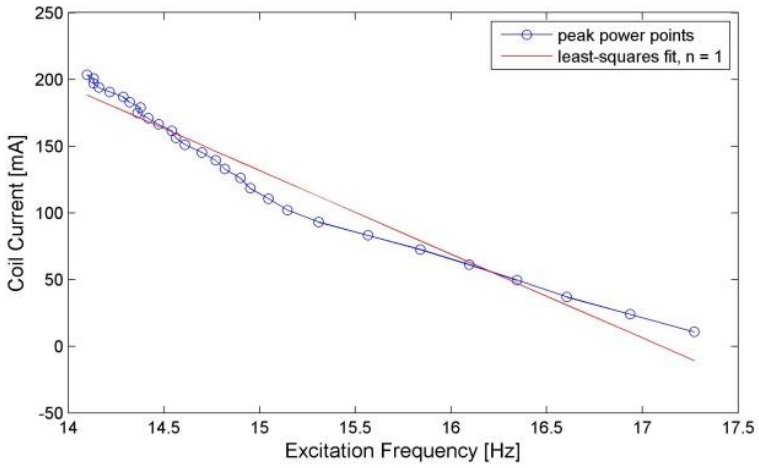

Figure 55. Open-loop control law fitting approach for up-chirp excitation

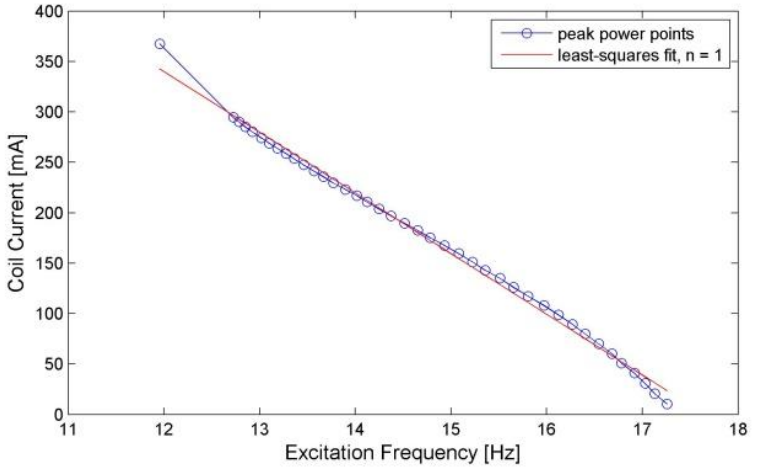

Figure 56. Open-loop control law fitting approach for down-chirp excitation

5.5.2. Open-loop Control Dynamic Testing

As shown in Figure 57a the resulting output power response of the inertial generator now fully captures resonant energy in the transition region, thus validating the experimental hypothesis. This approach was also applied to harmonic down-chirp excitations; however, as

shown in Figure 57b, the power response is significantly less than that of the up-chirp excitations.

(a)

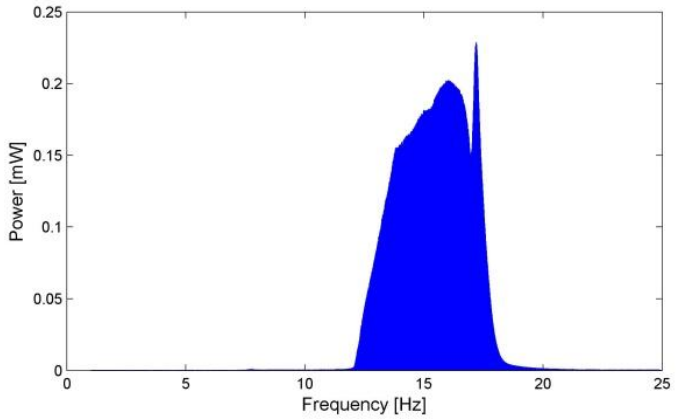

(b)

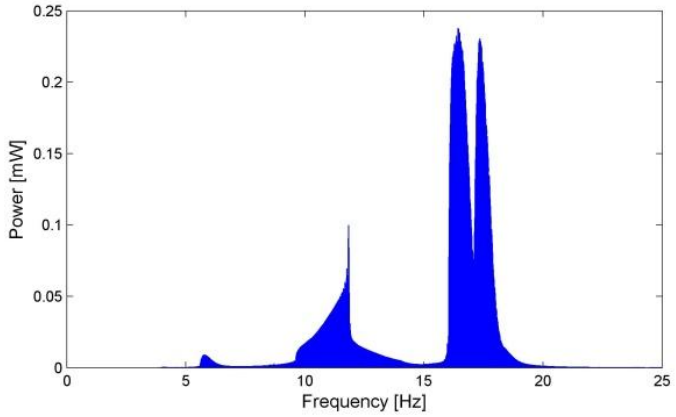

Figure 57. Broadband inertial generator response for chirp excitations under modulated coil currents

As the results show in Figure 57, the hypothesis that controlling the bistable potential energy separatrix can result in an augmented resonant frequency response. However, due to the complex nonlinear dynamics inherent to the system, a more advanced control law is necessary for this method to be viable in field operations.

A significant portion of Chapter 5 has been submitted for publication in Smart Materials and Structures, Scott Ouellette and Michael Todd, 2015. The title of this paper is "Modulating the Bistable Potential Energy Separatrix for Augmented Broadband Vibration Energy Harvesting". The dissertation author was the primary investigator and author of this paper.

Another portion of Chapter 5 has been published in Proc. of SPIE, Scott Ouellette and Michael Todd, 2014. The title of this paper is "Broadband Energy Harvesting via Adaptive Control of the Bistable Potential Energy Separatrix". The dissertation author was the primary investigator and author of this paper.

Chapter 6
Conclusions and Future Work

6.1. Conclusions of Energy Harvesting Methods

The research presented in this dissertation provides a basis framework for future advances in autonomously-powered sensor networks for persistent remote monitoring applications in various environments. First, we established a systemic paradigm of the energy harvesting approach to autonomous sensor networks, and highlighted the necessary design considerations required for a robust implementation in remote field applications. Second, a thorough review of the state of energy harvesting research for a wide variety of transduction methods was conducted in order to provide a global perspective of the scope of energy generation, as well as the requisite power requirements for sensing and communications telemetry.

In Chapters 2 and 3, we developed a novel corrosion-based energy harvester and complimentary low-power sensor node for marine infrastructure health monitoring. In Chapter 2, the chemical process of electron transfer and ion migration was developed in conjunction with an equivalent circuit model as a means for estimating the viability of power output under

various environmental and use-case conditions. Experimental specimen were fabricated, and a suite of parametric tests were performed to generate a statistical metric for power output and performance. In Chapter 3, these models were then applied to the design of a low-power sensor node such that low duty-cycle measurements of structural health could be acquired without the need of an external power source (e.g. a battery). A statistical analysis of the sensor node performance was studied using a Monte Carlo approach to SPICE circuit simulations, with primary focus being the feedback-regulated output voltage of the DC-DC boost converter for a given distribution of supply voltages. Based on the results of this statistical analysis, a prototype dual-layer PCB was developed and tested to validate the simulation results of the SPICE model. Furthermore, a detailed power analysis study of the sensor node was developed, and for an assumed duty-cycle of data acquisition and transmission, the overall operational lifetime of the C-SWB corrosion-based energy harvester was estimated.

The main focus of Chapter 4 was a detailed literature review of the state of vibration energy harvesting (VEH) research as it pertains to broadband energy capture methods. A classification scheme was applied to compare the various methods studied, and to compare their relative strengths and weaknesses. Based on the classification scheme, it was concluded that bistable inertial generators showed the greatest promise towards adaptation in field operations with respect to the other methods of broadband VEH. The specific intent of the chapter was to motivate the necessity of the novel approach to dynamically modulate the potential energy separatrix barrier in bistable inertial generators for augmented broadband energy capture.

Lastly, in Chapter 5, a novel framework for modulating the magnetic field of bistable inertial generators was developed by means of implementing a high-permeability electromagnet. This approach lends itself to a rich system of non-equilibrium nonlinear dynamics as the result of a periodically disappearing saddle node bifurcation qualitatively alters

the response of the inertial generator between a monostable and bistable configuration. Closed-form analytical expressions were developed to model the magnetic dipole moment of a finite-length cylindrical electromagnet, and the nonlinear interaction between dipole moments was studied. Additionally, analytical buckling and free-vibration mode shapes were developed, and the resulting quasi-static expressions were combined with the magnetic forcing model to generate an analytical 2-parameter bifurcation diagram. A quasi-static experimental test was conducted to validate the 2-parameter bifurcation space using a Laser-Doppler Vibrometer (LDV) to measure out-of-plane displacement of the MIG tip mass. Next, a suite of parametric dynamic tests were performed to empirically investigate the MIG response and power output for harmonic chirp excitations. From these results, we developed an open-loop linear control law to modulate the coil current of the buckling electromagnet during a single chirp excitation test to validate the augmented broadband resonant response hypothesis.

A list of the main contributions made in this dissertation is as follows:

Developed a systematic paradigm of the energy harvesting process as a means to provide a cogent description of the multi-disciplinary process of energy capture to usage

Development of a novel corrosion-based energy harvester and complimentary low-power sensor node for applications to long-term, low-cost marine infrastructure health monitoring

Analytically modeled and experimentally verified the ability to extend the broadband resonant response of a piezoelectric inertial generator by adaptively modulating the bistable potential energy separatrix

6.2. Future Work for Autonomous Marine Infrastructure Sensor Networks

From this research, there emerge a few salient new paths for future investigations into corrosion-based energy harvesting. There exist two readily apparent research topics in which contributions to this paradigm can be made, and they are presented below.

6.2.1. Advances in Low-Power ICs and Wireless Network Protocols

With regards to the sensor node design, the commercial hardware selected back in 2013 is now relatively obsolete. New low-power solutions for various communications platforms are continually brought to market, and with semiconductor System-on-Chip (SoC) solutions becoming more commercially prevalent, the overall power demands of the sensing and communications telemetry are rapidly decreasing. Furthermore, recent advances in wireless communication protocols and networking algorithms are particularly well-suited for adaptation to this type of paradigm. Issues with non-stationary power generation, and signal attenuation from the reinforcing steel rebar within pier columns will certainly need to be addressed as well.

6.2.2. Optimal Design of C-SWB Electrodes and Byproduct Control

A detailed power analysis and operational lifetime estimate was developed in this dissertation; however, an optimal design of the electrodes / battery is still to be developed. Parameters such as electrode spacing, electrode shape, and cement porosity are perfect candidates for investigation. Furthermore, a chemical coating that can provide a solvent for the anode should be investigated in order to prevent the formation of the insoluble precipitate, thus allowing for the full consumption of the anodic material.

6.3. Future Work for MIG Energy Harvesters

The research presented on the MIG presents a rich suite of new investigation opportunities with regards to system design. The salient points of future research interest are categorized below in order of relevance.

6.3.1. Numerical Simulations of Dynamic Response

The ability to model the complex coupled dynamics of the MIG will prove essential for future design optimizations, especially as it pertains to the goal of a net-positive power output. While several numerical models exist for bistable IGs, as well as systems for a periodically disappearing separatrix, the ability to numerically simulate the power output response under a dynamically varying separatrix barrier is yet to be seen.

6.3.2. Update Magnetic Force-Interaction Model

While post-processing the experimental data, it was observed that the assumed magnetic interaction model exhibits a dynamic characteristic resulting from Faraday's Law of Induction. In essence, when the MIG is at resonance, a noticeable harmonic fluctuation can be measured within the electromagnet coil. As such, the analytical model for the interacting dipole moments needs to be updated to account for the dynamic action of the fluctuating field, and this model should then be applied to study the effects on power generation in the MIG.

6.3.3. Optimal Design of Electromagnet

This dissertation also provided a detailed power analysis of the electromagnet subject to specific design parameters such as the coil length, materials choice, wire gauge, iron core geometry, and iron core magnetic permeability. Given the analytical buckling analysis provided, the critical buckling coil current can be extracted, which would provide a sensitivity expression around which an optimal set of electromagnet design parameters can be studied.

6.3.4. Develop Closed-Loop Control Law

Lastly, the control law developed in this study was of low-order and only served as a proof-of-concept with regards to the effect of modulating the separatrix barrier. For more realistic vibratory environments, an adaptive closed-loop control law will be required as a means of adequately augmenting the broadband resonant response spectrum.Figure 40. (a) characteristic curve tracing for iron core. At point 0 the material is un-magnetized. Once a magnetizing field is applied, typically via a current carrying coil, the magnetic domains align and the **B**-field saturates at point 1. Once the coil current is reduced to zero, the magnetism in the material domains remain. (b) An idealized, no-loss, core representation used for simple analyses.

Appendix

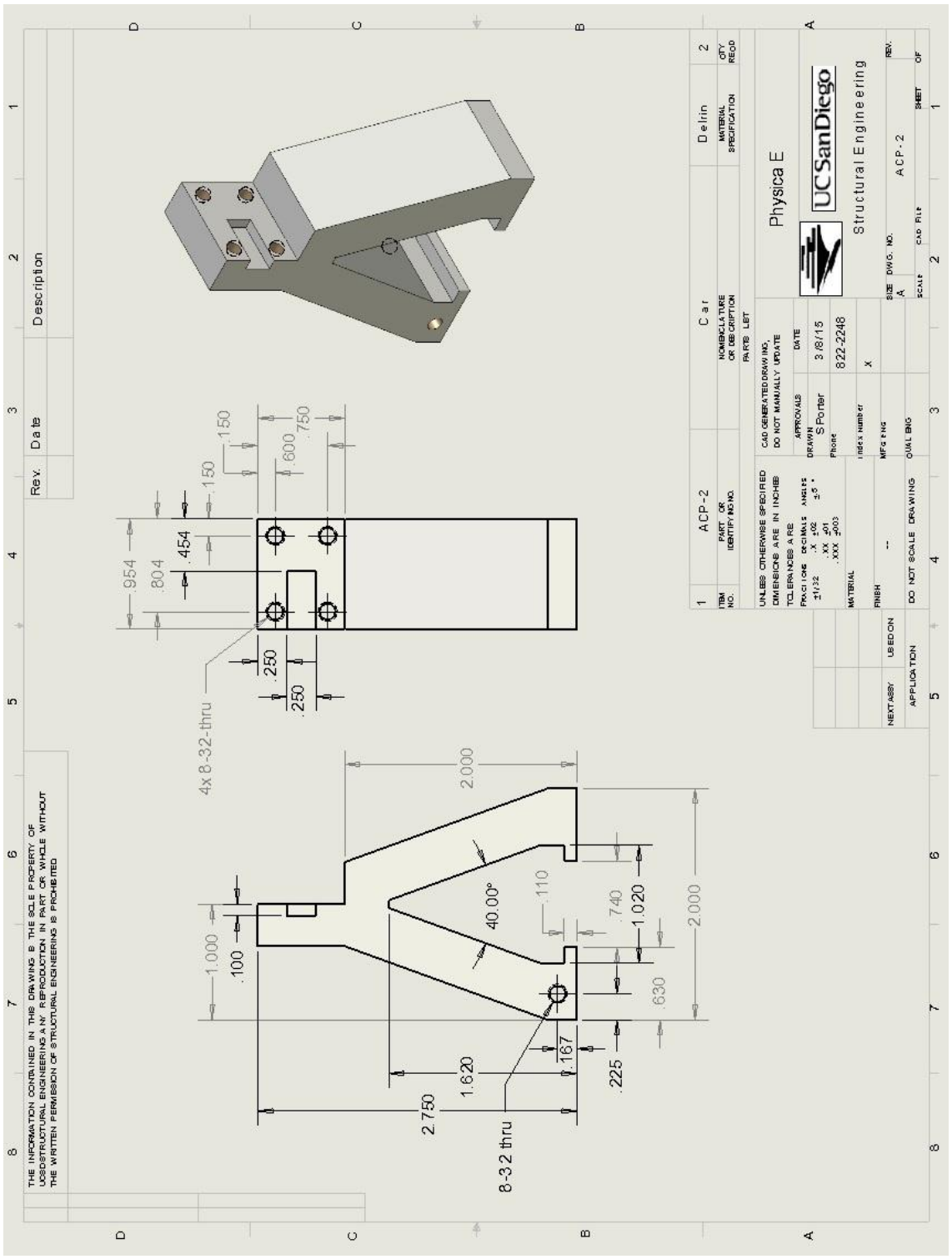

Figure 58. Mechanical drawing of A-frame cart

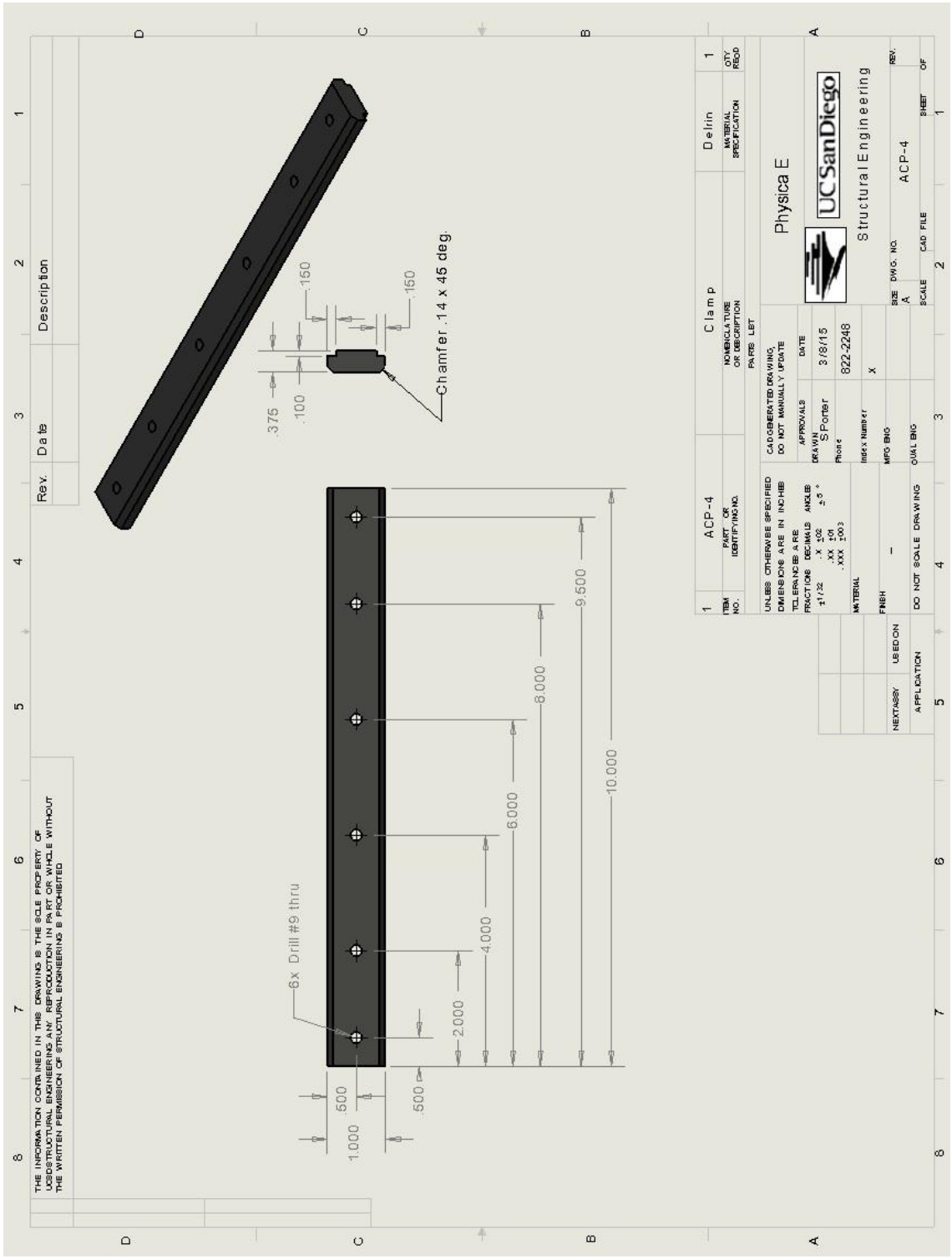

Figure 59. Mechanical drawing of clamp rail

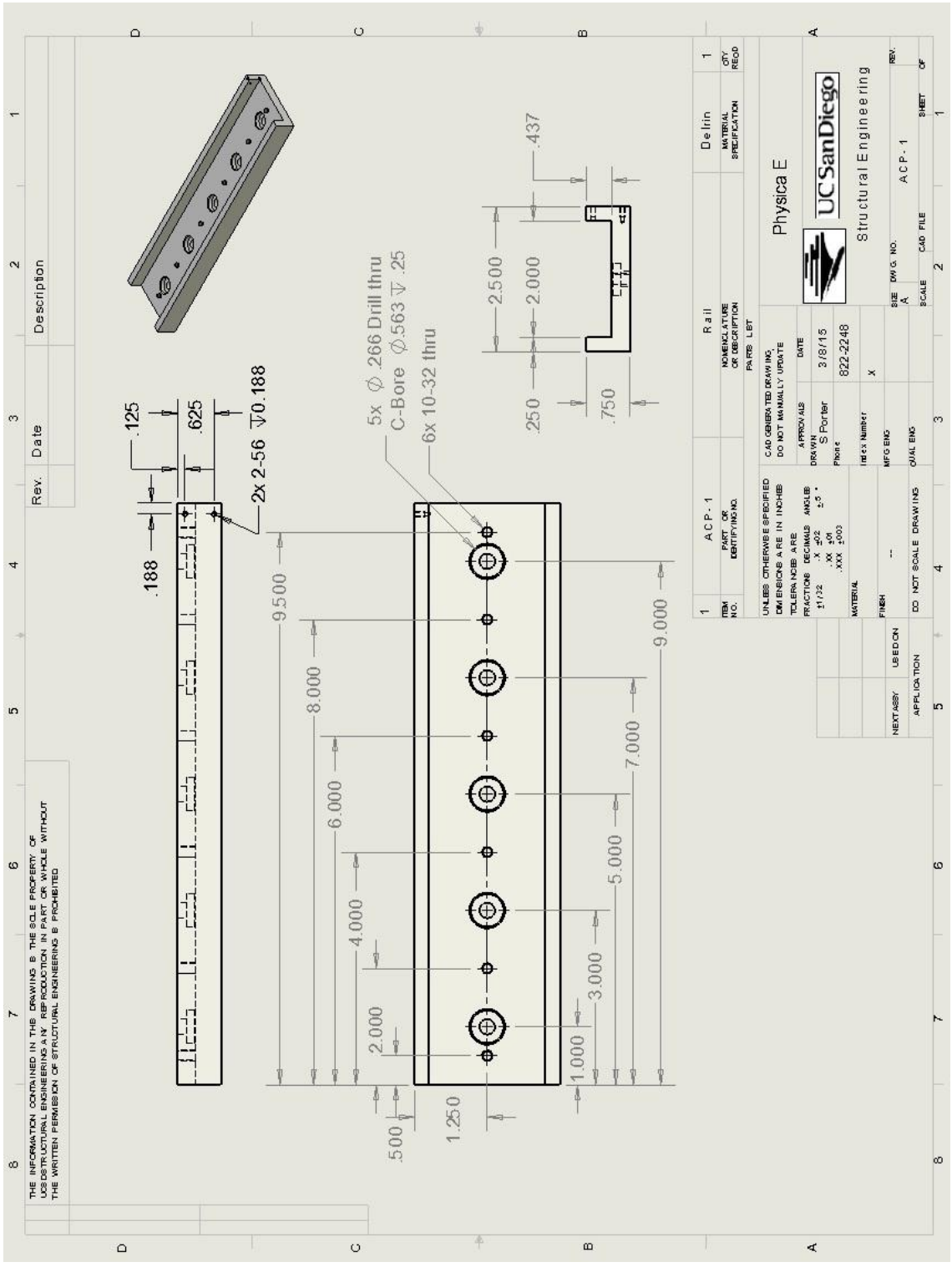

Figure 60. Mechanical drawing of rail mount

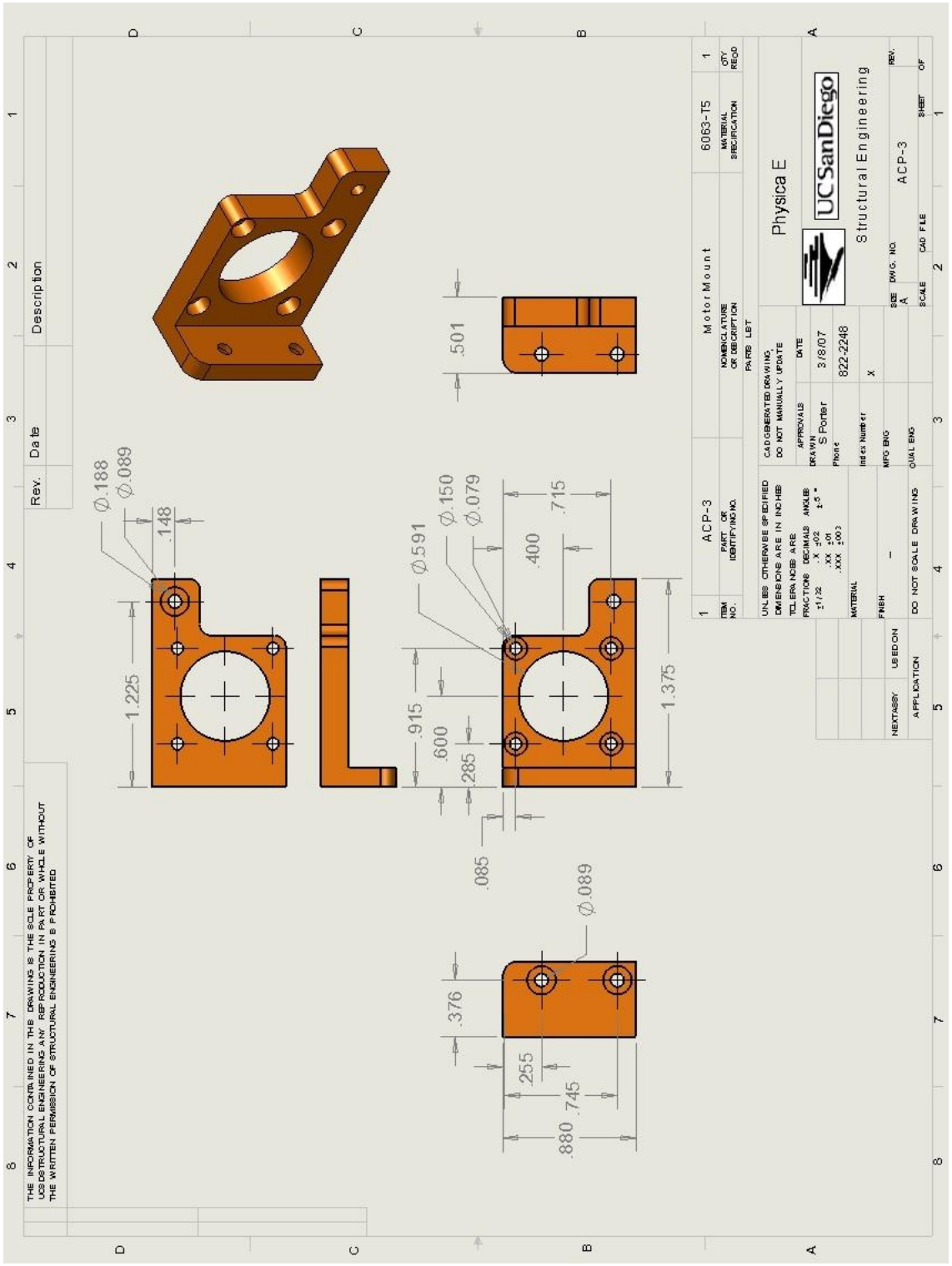

Figure 61. Mechanical drawing of stepper motor mount

References

[1] S. R. Anton and H. A. Sodano, "A review of power harvesting using piezoelectric materials (2003–2006)," *Smart Mater. Struct.*, vol. 16, no. 3, p. R1, Jun. 2007.

[2] D. N. Fry, D. E. Holcomb, J. K. Munro, L. C. Oakes, and M. J. Matson, "Compact portable electric power sources," Oak Ridge National Lab., TN (United States), 1997.

[3] P. Glynne-Jones and N. M. White, "Self-powered systems: a review of energy sources," *Sensor review*, vol. 21, no. 2, pp. 91–98, 2001.

[4] S. J. Roundy, "Energy scavenging for wireless sensor nodes with a focus on vibration to electricity conversion," University of California, 2003.

[5] M. A. Qidwai, J. P. Thomas, J. C. Kellogg, and J. N. Baucom, "Energy harvesting concepts for small electric unmanned systems," 2004, vol. 5387, pp. 84–95.

[6] L. Mateu and F. Moll, "Review of energy harvesting techniques and applications for microelectronics," in *Proc. SPIE*, 2005, vol. 5837, pp. 359–373.

[7] J. A. Paradiso and T. Starner, "Energy scavenging for mobile and wireless electronics," *IEEE Pervasive Computing*, vol. 4, no. 1, pp. 18–27, 2005.

[8] "IEEE Standard on Piezoelectricity," *ANSI/IEEE Std 176-1987*, p. 0_1–, 1988.

[9] W. F. Smith and J. Hashemi, *Foundations of Materials Science and Engineering*, 4th ed. McGraw-Hill, 2005.

[10] M. Walsh, "Single cell seawater batteries," in *Power Sources Symposium, 1990., Proceedings of the 34th International*, 1990, pp. 110–111.

[11] J. S. Lauer, J. F. Jackovitz, and E. S. Buzzelli, "Seawater activated power source for long term missions," in *Power Sources Symposium, 1990., Proceedings of the 34th International*, 1990, pp. 115 –117.

[12] O. Hasvold, "Seawater batteries for low power, long term applications," in *Power Sources Symposium, 1990., Proceedings of the 34th International*, 1990, pp. 50 –52.

[13] W. S. D. Wilcock and P. C. Kauffman, “Development of a seawater battery for deep-water applications,” *Journal of Power Sources*, vol. 66, no. 1–2, pp. 71–75, May 1997.

[14] B. E. Logan and J. M. Regan, “Microbial Fuel Cells—Challenges and Applications,” *Environ. Sci. Technol.*, vol. 40, no. 17, pp. 5172–5180, Sep. 2006.

[15] A. Meehan, H. Gao, and Z. Lewandowski, “Energy Harvesting With Microbial Fuel Cell and Power Management System,” *IEEE Transactions on Power Electronics*, vol. 26, no. 1, pp. 176–181, 2011.

[16] A. Dewan, H. Beyenal, and Z. Lewandowski, “Scaling up Microbial Fuel Cells,” *Environ. Sci. Technol.*, vol. 42, no. 20, pp. 7643–7648, Oct. 2008.

[17] M. F. Silva, J. F. Ribeiro, J. P. Carmo, L. M. Gonçalves, and J. H. Correia, “Thin Films for Thermoelectric Applications,” in *Scanning Probe Microscopy in Nanoscience and Nanotechnology 3*, B. Bhushan, Ed. Springer Berlin Heidelberg, 2013, pp. 485–528.

[18] G. J. Snyder and E. S. Toberer, “Complex thermoelectric materials,” *Nat Mater*, vol. 7, no. 2, pp. 105–114, Feb. 2008.

[19] H. J. Visser and R. J. M. Vullers, “RF Energy Harvesting and Transport for Wireless Sensor Network Applications: Principles and Requirements,” *Proceedings of the IEEE*, vol. 101, no. 6, pp. 1410–1423, 2013.

[20] H. J. Visser, A. C. F. Reniers, and J. A. C. Theeuwes, “Ambient RF Energy Scavenging: GSM and WLAN Power Density Measurements,” in *Microwave Conference, 2008. EuMC 2008. 38th European*, 2008, pp. 721–724.

[21] *e-CFR: TITLE 47—Telecommunication*, vol. TITLE 47—Telecommunication. .

[22] G. Simon, M. Maróti, Á. Lédeczi, G. Balogh, B. Kusy, A. Nádas, G. Pap, J. Sallai, and K. Frampton, “Sensor network-based countersniper system,” in *Proceedings of the 2nd international conference on Embedded networked sensor systems*, New York, NY, USA, 2004, pp. 1–12.

[23] M. Castillo-Effer, D. H. Quintela, W. Moreno, R. Jordan, and W. Westhoff, “Wireless sensor networks for flash-flood alerting,” in *Proceedings of the Fifth IEEE International Caracas Conference on Devices, Circuits and Systems, 2004*, 2004, vol. 1, pp. 142–146.

[24] K. Lorincz, D. J. Malan, T. R. F. Fulford-Jones, A. Nawoj, A. Clavel, V. Shnayder, G. Mainland, M. Welsh, and S. Moulton, “Sensor networks for emergency response: challenges and opportunities,” *IEEE Pervasive Computing*, vol. 3, no. 4, pp. 16–23, 2004.

[25] J. Yick, B. Mukherjee, and D. Ghosal, “Analysis of a prediction-based mobility adaptive tracking algorithm,” in *2nd International Conference on Broadband Networks, 2005. BroadNets 2005*, 2005, pp. 753–760 Vol. 1.

[26] T. Gao, D. Greenspan, M. Welsh, R. Juang, and A. Alm, “Vital Signs Monitoring and Patient Tracking Over a Wireless Network,” in *Engineering in Medicine and Biology Society, 2005. IEEE-EMBS 2005. 27th Annual International Conference of the*, 2005, pp. 102–105.

[27] G. Werner-Allen, J. Johnson, M. Ruiz, J. Lees, and M. Welsh, “Monitoring volcanic eruptions with a wireless sensor network,” in *Proceeedings of the Second European Workshop on Wireless Sensor Networks, 2005*, 2005, pp. 108–120.

[28] J. Yick, B. Mukherjee, and D. Ghosal, “Wireless sensor network survey,” *Computer Networks*, vol. 52, no. 12, pp. 2292–2330, Aug. 2008.

[29] G. Anastasi, M. Conti, M. Di Francesco, and A. Passarella, “Energy conservation in wireless sensor networks: A survey,” *Ad Hoc Networks*, vol. 7, no. 3, pp. 537–568, May 2009.

[30] S. Bhatti and J. Xu, “Survey of target tracking protocols using wireless sensor network,” in *Wireless and Mobile Communications, 2009. ICWMC’09. Fifth International Conference on*, 2009, pp. 110–115.

[31] W. K. Seah, Z. A. Eu, and H.-P. Tan, “Wireless sensor networks powered by ambient energy harvesting (WSN-HEAP)-Survey and challenges,” in *Wireless Communication, Vehicular Technology, Information Theory and Aerospace & Electronic Systems Technology, 2009. Wireless VITAE 2009. 1st International Conference on*, 2009, pp. 1–5.

[32] J. Sen, “A Survey on Wireless Sensor Network Security,” arXiv e-print 1011.1529, Nov. 2010.

[33] M. Di Francesco, S. K. Das, and G. Anastasi, “Data collection in wireless sensor networks with mobile elements: A survey,” *ACM Transactions on Sensor Networks (TOSN)*, vol. 8, no. 1, p. 7, 2011.

[34] G. Werner-Allen, K. Lorincz, M. Ruiz, O. Marcillo, J. Johnson, J. Lees, and M. Welsh, “Deploying a wireless sensor network on an active volcano,” *IEEE Internet Computing*, vol. 10, no. 2, pp. 18–25, 2006.

[35] I. F. Akyildiz, D. Pompili, and T. Melodia, “Underwater acoustic sensor networks: research challenges,” *Ad Hoc Networks*, vol. 3, no. 3, pp. 257–279, May 2005.

[36] J. Heidemann, W. Ye, J. Wills, A. Syed, and Y. Li, “Research challenges and applications for underwater sensor networking,” in *IEEE Wireless Communications and Networking Conference, 2006. WCNC 2006*, 2006, vol. 1, pp. 228–235.

[37] R. Mijarez, P. Gaydecki, and M. Burdekin, “Flood member detection for real-time structural health monitoring of sub-sea structures of offshore steel oilrigs,” *Smart Mater. Struct.*, vol. 16, no. 5, p. 1857, Oct. 2007.

[38] “AMS Journals Online - Weather Classification Using Passive Acoustic Drifters.” .

[39] J. Förster, G. Gust, and S. Stolte, “A Piezoelectrical Rain Gauge for Application on Buoys,” *Journal of Atmospheric and Oceanic Technology*, vol. 21, no. 2, pp. 179–193, Feb. 2004.

[40] E. Cayirci, H. Tezcan, Y. Dogan, and V. Coskun, “Wireless sensor networks for underwater survelliance systems,” *Ad Hoc Networks*, vol. 4, no. 4, pp. 431–446, Jul. 2006.

[41] D. Mascarenas, E. Flynn, C. Farrar, G. Park, and M. Todd, “A Mobile Host Approach for Wireless Powering and Interrogation of Structural Health Monitoring Sensor Networks,” *IEEE Sensors Journal*, vol. 9, no. 12, pp. 1719–1726, 2009.

[42] T. Ishimaru, H. Otobe, T. Saino, H. Hasumoto, and T. Nakai, “OCTOPUS, an Octo parameter underwater sensor, for use in biological oceanography studies,” *Journal of the Oceanographical Society of Japan*, vol. 40, no. 3, pp. 207–212, Jun. 1984.

[43] H. B. Nguyen, H. A. DeFerrari, N. J. Williams, and W. A. Venezia, "Ocean acoustic sensor installation at the South Florida Ocean Measurement Center," *IEEE Journal of Oceanic Engineering*, vol. 27, no. 2, pp. 235–244, 2002.

[44] C. Detweiller, I. Vasilescu, and D. Rus, "An Underwater Sensor Network with Dual Communications, Sensing, and Mobility," in *OCEANS 2007 - Europe*, 2007, pp. 1–6.

[45] S. Ibrahim, J.-H. Cui, and R. Ammar, "Surface-Level Gateway Deployment for Underwater Sensor Networks," in *IEEE Military Communications Conference, 2007. MILCOM 2007*, 2007, pp. 1–7.

[46] M. E. Nielsen, C. E. Reimers, H. K. White, S. Sharma, and P. R. Girguis, "Sustainable energy from deep ocean cold seeps," *Energy Environ. Sci.*, vol. 1, no. 5, pp. 584–593, Nov. 2008.

[47] M. Shinohara, E. Araki, M. Mochizuki, T. Kanazawa, and K. Suyehiro, "Practical application of a sea-water battery in deep-sea basin and its performance," *Journal of Power Sources*, vol. 187, no. 1, pp. 253–260, Feb. 2009.

[48] I. Vasilescu, C. Detweiler, M. Doniec, D. Gurdan, S. Sosnowski, J. Stumpf, and D. Rus, "AMOUR V: A Hovering Energy Efficient Underwater Robot Capable of Dynamic Payloads," *The International Journal of Robotics Research*, vol. 29, no. 5, pp. 547–570, Apr. 2010.

[49] C. C. Enz, A. El-Hoiydi, J.-D. Decotignie, and V. Peiris, "WiseNET: an ultralow-power wireless sensor network solution," *Computer*, vol. 37, no. 8, pp. 62–70, 2004.

[50] R. Szewczyk, J. Polastre, A. Mainwaring, and D. Culler, "Lessons from a Sensor Network Expedition," in *Wireless Sensor Networks*, H. Karl, A. Wolisz, and A. Willig, Eds. Springer Berlin Heidelberg, 2004, pp. 307–322.

[51] R. Cardell-Oliver, M. Kranz, K. Smettem, and K. Mayer, "A Reactive Soil Moisture Sensor Network: Design and Field Evaluation," *International Journal of Distributed Sensor Networks*, vol. 1, no. 2, pp. 149–162, 2005.

[52] D. Diamond, S. Coyle, S. Scarmagnani, and J. Hayes, "Wireless Sensor Networks and Chemo-/Biosensing," *Chem. Rev.*, vol. 108, no. 2, pp. 652–679, Feb. 2008.

[53] A.-K. Othman, K. M. Lee, H. Zen, W. A. W. Zainal, and M. F. M. Sabri, "Wireless sensor networks for swift bird farms monitoring," in *International Conference on Ultra Modern Telecommunications Workshops, 2009. ICUMT '09*, 2009, pp. 1–7.

[54] Y. Sun, L. Li, P. Schulze Lammers, Q. Zeng, J. Lin, and H. Schumann, "A solar-powered wireless cell for dynamically monitoring soil water content," *Computers and Electronics in Agriculture*, vol. 69, no. 1, pp. 19–23, Nov. 2009.

[55] R.-H. Ma, Y.-H. Wang, and C.-Y. Lee, "Wireless Remote Weather Monitoring System Based on MEMS Technologies," *Sensors*, vol. 11, no. 12, pp. 2715–2727, Mar. 2011.

[56] D. Diamond, F. Collins, J. Cleary, C. Zuliani, and C. Fay, "Distributed Environmental Monitoring," in *Autonomous Sensor Networks*, vol. 13, D. Filippini, Ed. Berlin, Heidelberg: Springer Berlin Heidelberg, 2012, pp. 321–363.

[57] J. A. Nystuen and H. D. Selsor, "Weather Classification Using Passive Acoustic Drifters," *Journal of Atmospheric and Oceanic Technology*, vol. 14, no. 3, pp. 656–666, Jun. 1997.

[58] B. R. Thomas, E. C. Kent, and V. R. Swail, “Methods to homogenize wind speeds from ships and buoys,” *International Journal of Climatology*, vol. 25, no. 7, pp. 979–995, 2005.

[59] A. Ethier and J. Bedard, “Development of a Real-Time Water Quality Buoy for the Fraser River Estuary,” in *OCEANS 2007*, 2007, pp. 1–6.

[60] J. F. Vesecky, K. Laws, S. I. Petersen, C. Bazeghi, and D. Wiberg, “Prototype autonomous mini-buoy for use in a wireless networked, ocean surface sensor array,” in *Geoscience and Remote Sensing Symposium, 2007. IGARSS 2007. IEEE International*, 2007, pp. 4987–4990.

[61] G. H. Koch, M. P. H. Brongers, N. G. Thompson, Y. P. Virmani, and J. H. Payer, “Corrosion cost and preventive strategies in the United States,” Turner-Fairbank Highway Research Center, 2002.

[62] B. Phares, G. Washer, D. Rolander, B. Graybeal, and M. Moore, “Routine Highway Bridge Inspection Condition Documentation Accuracy and Reliability,” *Journal of Bridge Engineering*, vol. 9, no. 4, pp. 403–413, 2004.

[63] R. B. Polder and M. R. De Rooij, “Durability of marine concrete structures-field investigations and modelling,” *HERON-ENGLISH EDITION-*, vol. 50, no. 3, p. 133, 2005.

[64] P. L. Fuhr, D. R. Huston, A. P. McPadden, and R. F. Cauley, “Embedded chloride detectors for roadways and bridges,” pp. 229–237, Apr. 1996.

[65] P. L. Fuhr, D. R. Huston, and B. MacCraith, “Embedded fiber optic sensors for bridge deck chloride penetration measurement,” *Opt. Eng*, vol. 37, no. 4, pp. 1221–1228, Apr. 1998.

[66] P. A. GAYDECKP and F. M. BURDEKIN, “Nondestructive Testing of Reinforced and Pre-Stressed Concrete Structures,” *Nondestructive Testing and Evaluation*, vol. 14, no. 6, pp. 339–392, 1998.

[67] G. Park, T. Rosing, M. Todd, C. Farrar, and W. Hodgkiss, “Energy Harvesting for Structural Health Monitoring Sensor Networks,” *Journal of Infrastructure Systems*, vol. 14, no. 1, pp. 64–79, 2008.

[68] Ø. Hasvold, H. Henriksen, E. Melv‡r, G. Citi, B. Ø. Johansen, T. Kjønigsen, and R. Galetti, “Sea-water battery for subsea control systems,” *Journal of Power Sources*, vol. 65, no. 1–2, pp. 253–261, Mar. 1997.

[69] G. Qiao, G. Sun, Y. Hong, Y. Qiu, and J. Ou, “Remote corrosion monitoring of the RC structures using the electrochemical wireless energy-harvesting sensors and networks,” *NDT and E International*, vol. 44, no. 7, pp. 583–588, 2011.

[70] G. Qiao, T. Liu, J. Dai, Y. Hong, and J. Wan, “Qualitative and Quantitative Sensors Based on Electrochemical Techniques for the Corrosion Assessment of RC Panels,” *IEEE Sensors Journal*, vol. 12, no. 6, pp. 2062–2063, 2012.

[71] G. Qiao, Y. Hong, G. Sun, and O. Yang, “Corrosion energy: A novel source to power the wireless sensor,” *IEEE Sensors Journal*, vol. 13, no. 4, pp. 1141–1142, 2013.

[72] J. Raven, K. Caldeira, H. Elderfield, O. Hoegh-Guldberg, P. Liss, U. Riebesell, J. Shepherd, C. Turley, and A. Watson, “Ocean acidification due to increasing atmospheric carbon dioxide,” 2005.

[73] V. Feliu, J. A. González, C. Andrade, and S. Feliu, “Equivalent circuit for modelling the steel-concrete interface. I. Experimental Evidence and theoretical predictions,” *Corrosion Science*, vol. 40, no. 6, pp. 975–993, 1998.

[74] V. Feliu, J. A. González, C. Adrade, and S. Feliu, “Equivalent circuit for modelling the steel-concrete interface. II. Complications in applying the stern-geary equation to corrosion rate determinations,” *Corrosion science*, vol. 40, no. 6, pp. 995–1006, 1998.

[75] S. A. Ouellette and M. D. Todd, “Ultra low-power corrosion-enabled sensor node,” pp. 834523–834523, Apr. 2012.

[76] M. Mellas, B. Mezghiche, and J. E. Ash, “Estimation of the porosity of Portland cement pastes using backscattered electron image,” in *Role of Cement Science in Sustainable Development*, 2003.

[77] Texas Instruments, “TLC 551 LinCMOS Timers.” Sep-1997.

[78] H. Kim, S. Priya, H. Stephanou, and K. Uchino, “Consideration of impedance matching techniques for efficient piezoelectric energy harvesting,” *Ultrasonics, Ferroelectrics and Frequency Control, IEEE Transactions on*, vol. 54, no. 9, pp. 1851–1859, 2007.

[79] L. R. Clare and S. G. Burrow, “Power conditioning for energy harvesting,” in *Proc SPIE*, 2008, vol. 6928, p. 69280A.

[80] N. Kong, D. S. Ha, A. Erturk, and D. J. Inman, “Resistive Impedance Matching Circuit for Piezoelectric Energy Harvesting,” *Journal of Intelligent Material Systems and Structures*, vol. 21, no. 13, pp. 1293–1302, Sep. 2010.

[81] S. A. Ouellette and M. D. Todd, “Uncertainty quantification of a corrosion-enabled energy harvester for low-power sensing applications,” p. 86921G–86921G, Apr. 2013.

[82] S. A. Ouellette and M. D. Todd, “Uncertainty quantification of a corrosion-enabled energy harvester for low-power sensing applications,” 2013, p. 86921G–86921G–8.

[83] B. P. Mann, “Broadband Energy Harvesting from a Bistable Potential Well,” in *Advances in Energy Harvesting Methods*, N. Elvin and A. Erturk, Eds. Springer New York, 2013, pp. 91–115.

[84] L. Gu and C. Livermore, “Passive self-tuning energy harvester for extracting energy from rotational motion,” *Applied Physics Letters*, vol. 97, no. 8, pp. 081904–081904–3, 2010.

[85] S. E. Jo, M. S. Kim, and Y.-J. Kim, “Passive-self-tunable vibrational energy harvester,” in *Solid-State Sensors, Actuators and Microsystems Conference (TRANSDUCERS), 2011 16th International*, 2011, pp. 691–694.

[86] D. Zhu, S. Roberts, J. Tudor, and S. Beeby, “Closed loop frequency tuning of a vibration-based micro-generator,” 2008.

[87] I. N. Ayala-Garcia, D. Zhu, M. J. Tudor, and S. P. Beeby, “A tunable kinetic energy harvester with dynamic over range protection,” *Smart Materials and Structures*, vol. 19, no. 11, p. 115005, 2010.

[88] V. R. Challa, M. G. Prasad, and F. T. Fisher, “Towards an autonomous self-tuning vibration energy harvesting device for wireless sensor network applications,” *Smart Materials and Structures*, vol. 20, no. 2, p. 025004, 2011.

[89] S. Roundy and Y. Zhang, “Toward self-tuning adaptive vibration-based microgenerators,” 2005, vol. 5649, pp. 373–384.

[90] C. Peters, D. Maurath, W. Schock, F. Mezger, and Y. Manoli, “A closed-loop wide-range tunable mechanical resonator for energy harvesting systems,” *Journal of Micromechanics and Microengineering*, vol. 19, no. 9, p. 094004, 2009.

[91] E. S. Leland and P. K. Wright, “Resonance tuning of piezoelectric vibration energy scavenging generators using compressive axial preload,” *Smart Mater. Struct.*, vol. 15, no. 5, p. 1413, Oct. 2006.

[92] C. Eichhorn, F. Goldschmidtboeing, and P. Woias, “A frequency tunable piezoelectric energy converter based on a cantilever beam,” *Proceedings of PowerMEMS*, vol. 9, no. 12, pp. 309–312, 2008.

[93] Y. Hu, H. Xue, and H. Hu, “A piezoelectric power harvester with adjustable frequency through axial preloads,” *Smart Mater. Struct.*, vol. 16, no. 5, p. 1961, Oct. 2007.

[94] D. J. Morris, J. M. Youngsman, M. J. Anderson, and D. F. Bahr, “A resonant frequency tunable, extensional mode piezoelectric vibration harvesting mechanism,” *Smart Mater. Struct.*, vol. 17, no. 6, p. 065021, Dec. 2008.

[95] J. M. Youngsman, T. Luedeman, D. J. Morris, M. J. Anderson, and D. F. Bahr, “A model for an extensional mode resonator used as a frequency-adjustable vibration energy harvester,” *Journal of Sound and Vibration*, vol. 329, no. 3, pp. 277–288, Feb. 2010.

[96] J. Loverich, R. Geiger, and J. Frank, “Stiffness nonlinearity as a means for resonance frequency tuning and enhancing mechanical robustness of vibration power harvesters,” 2008, vol. 6928, pp. 692805–692805–10.

[97] X. Wu, J. Lin, S. Kato, K. Zhang, T. Ren, and L. Liu, “A frequency adjustable vibration energy harvester,” *Proceedings of PowerMEMS*, pp. 245–248, 2008.

[98] V. R. Challa, M. G. Prasad, Y. Shi, and F. T. Fisher, “A vibration energy harvesting device with bidirectional resonance frequency tunability,” *Smart Materials and Structures*, vol. 17, no. 1, p. 015035, 2008.

[99] T. Reissman, E. M. Wolff, and E. Garcia, “Piezoelectric resonance shifting using tunable nonlinear stiffness,” in *The 16th International Symposium on: Smart Structures and Materials & Nondestructive Evaluation and Health Monitoring*, 2009, p. 72880G–72880G.

[100] W.-J. Wu, Y.-Y. Chen, B.-S. Lee, J.-J. He, and Y.-T. Peng, “Tunable resonant frequency power harvesting devices,” 2006, vol. 6169, p. 61690A–61690A–8.

[101] M. Lallart, S. R. Anton, and D. J. Inman, “Frequency Self-tuning Scheme for Broadband Vibration Energy Harvesting,” *Journal of Intelligent Material Systems and Structures*, vol. 21, no. 9, pp. 897–906, Jun. 2010.

[102] M. Wischke, M. Masur, F. Goldschmidtboeing, and P. Woias, “Electromagnetic vibration harvester with piezoelectrically tunable resonance frequency,” *J. Micromech. Microeng.*, vol. 20, no. 3, p. 035025, Mar. 2010.

[103] A. Erturk, J. M. Renno, and D. J. Inman, "Modeling of piezoelectric energy harvesting from an L-shaped beam-mass structure with an application to UAVs," *Journal of Intelligent Material Systems and Structures*, vol. 20, no. 5, pp. 529–544, 2009.

[104] S. Roundy, E. S. Leland, J. Baker, E. Carleton, E. Reilly, E. Lai, B. Otis, J. M. Rabaey, P. K. Wright, and V. Sundararajan, "Improving power output for vibration-based energy scavengers," *IEEE Pervasive Computing*, vol. 4, no. 1, pp. 28–36, 2005.

[105] B. Yang, C. Lee, W. Xiang, J. Xie, J. H. He, R. K. Kotlanka, S. P. Low, and H. Feng, "Electromagnetic energy harvesting from vibrations of multiple frequencies," *J. Micromech. Microeng.*, vol. 19, no. 3, p. 035001, Mar. 2009.

[106] Y. Tadesse, S. Zhang, and S. Priya, "Multimodal Energy Harvesting System: Piezoelectric and Electromagnetic," *Journal of Intelligent Material Systems and Structures*, vol. 20, no. 5, pp. 625–632, Mar. 2009.

[107] Q. Ou, X. Chen, S. Gutschmidt, A. Wood, and N. Leigh, "A two-mass cantilever beam model for vibration energy harvesting applications," in *2010 IEEE Conference on Automation Science and Engineering (CASE)*, 2010, pp. 301–306.

[108] Q. Ou, X. Chen, S. Gutschmidt, A. Wood, N. Leigh, and A. F. Arrieta, "An experimentally validated double-mass piezoelectric cantilever model for broadband vibration–based energy harvesting," *Journal of Intelligent Material Systems and Structures*, vol. 23, no. 2, pp. 117–126, Jan. 2012.

[109] M. Arafa, W. Akl, A. Aladwani, O. Aldraihem, and A. Baz, "Experimental implementation of a cantilevered piezoelectric energy harvester with a dynamic magnifier," 2011, vol. 7977, p. 79770Q–79770Q–9.

[110] M. H. Arafa, "Multi-Modal Vibration Energy Harvesting Using a Trapezoidal Plate," *Journal of vibration and acoustics*, vol. 134, no. 4.

[111] D. F. Berdy, B. Jung, J. F. Rhoads, and D. Peroulis, "Increased-bandwidth, meandering vibration energy harvester," in *Solid-State Sensors, Actuators and Microsystems Conference (TRANSDUCERS), 2011 16th International*, 2011, pp. 2638–2641.

[112] H. Wu, L. Tang, Y. Yang, and C. K. Soh, "A novel two-degrees-of-freedom piezoelectric energy harvester," *Journal of Intelligent Material Systems and Structures*, vol. 24, no. 3, pp. 357–368, 2013.

[113] Z. Yang and J. Yang, "Connected vibrating piezoelectric bimorph beams as a wide-band piezoelectric power harvester," *Journal of Intelligent Material Systems and Structures*, vol. 20, no. 5, pp. 569–574, 2009.

[114] I.-H. Kim, H.-J. Jung, B. M. Lee, and S.-J. Jang, "Broadband energy-harvesting using a two degree-of-freedom vibrating body," *Applied Physics Letters*, vol. 98, no. 21, pp. 214102–214102–3, 2011.

[115] S. M. Shahruz, "Design of mechanical band-pass filters for energy scavenging," *Journal of Sound and Vibration*, vol. 292, no. 3–5, pp. 987–998, May 2006.

[116] H. Xue, Y. Hu, and Q.-M. Wang, "Broadband piezoelectric energy harvesting devices using multiple bimorphs with different operating frequencies," *IEEE Transactions on Ultrasonics, Ferroelectrics and Frequency Control*, vol. 55, no. 9, pp. 2104–2108, 2008.

[117] M. Ferrari, V. Ferrari, M. Guizzetti, D. Marioli, and A. Taroni, “Piezoelectric multifrequency energy converter for power harvesting in autonomous microsystems,” *Sensors and Actuators A: Physical*, vol. 142, no. 1, pp. 329–335, Mar. 2008.

[118] J.-Q. Liu, H.-B. Fang, Z.-Y. Xu, X.-H. Mao, X.-C. Shen, D. Chen, H. Liao, and B.-C. Cai, “A MEMS-based piezoelectric power generator array for vibration energy harvesting,” *Microelectronics Journal*, vol. 39, no. 5, pp. 802–806, May 2008.

[119] I. Sari, T. Balkan, and H. Kulah, “An electromagnetic micro power generator for wideband environmental vibrations,” *Sensors and Actuators A: Physical*, vol. 145–146, pp. 405–413, Jul. 2008.

[120] R. Ramlan, M. J. Brennan, B. R. Mace, and I. Kovacic, “Potential benefits of a non-linear stiffness in an energy harvesting device,” *Nonlinear dynamics*, vol. 59, no. 4, pp. 545–558, 2010.

[121] S. C. Stanton, C. C. McGehee, and B. P. Mann, “Reversible hysteresis for broadband magnetopiezoelastic energy harvesting,” *Applied Physics Letters*, vol. 95, no. 17, pp. 174103–174103–3, 2009.

[122] B. P. Mann and N. D. Sims, “Energy harvesting from the nonlinear oscillations of magnetic levitation,” *Journal of Sound and Vibration*, vol. 319, no. 1–2, pp. 515–530, Jan. 2009.

[123] M. F. Daqaq, “Response of uni-modal duffing-type harvesters to random forced excitations,” *Journal of Sound and Vibration*, vol. 329, no. 18, pp. 3621–3631, Aug. 2010.

[124] J. Moehlis, B. E. DeMartini, J. L. Rogers, and K. L. Turner, “Exploiting nonlinearity to provide broadband energy harvesting,” in *Proceedings of the ASME 2009 Dynamic Systems and Control Conference, Hollywood, CA*, 2009.

[125] M. S. M. Soliman, E. M. Abdel-Rahman, E. F. El-Saadany, and R. R. Mansour, “A wideband vibration-based energy harvester,” *J. Micromech. Microeng.*, vol. 18, no. 11, p. 115021, Nov. 2008.

[126] M. Soliman, E. M. Abdel-Rahman, E. F. El-Saadany, and R. R. Mansour, “A Design Procedure for Wideband Micropower Generators,” *Journal of Microelectromechanical Systems*, vol. 18, no. 6, pp. 1288–1299, 2009.

[127] A. Erturk, J. Hoffmann, and D. J. Inman, “A piezomagnetoelastic structure for broadband vibration energy harvesting,” *Applied Physics Letters*, vol. 94, no. 25, p. 254102, 2009.

[128] A. Erturk and D. J. Inman, “Broadband piezoelectric power generation on high-energy orbits of the bistable Duffing oscillator with electromechanical coupling,” *Journal of Sound and Vibration*, vol. 330, no. 10, pp. 2339–2353, May 2011.

[129] F. Cottone, H. Vocca, and L. Gammaitoni, “Nonlinear Energy Harvesting,” *Phys. Rev. Lett.*, vol. 102, no. 8, p. 080601, Feb. 2009.

[130] M. Ferrari, V. Ferrari, M. Guizzetti, B. Andò, S. Baglio, and C. Trigona, “Improved energy harvesting from wideband vibrations by nonlinear piezoelectric converters,” *Sensors and Actuators A: Physical*, vol. 162, no. 2, pp. 425–431, Aug. 2010.

[131] J.-T. Lin and B. Alphenaar, “Enhancement of Energy Harvested from a Random Vibration Source by Magnetic Coupling of a Piezoelectric Cantilever,” *Journal of Intelligent Material Systems and Structures*, vol. 21, no. 13, pp. 1337–1341, Dec. 2009.

[132] B. Andò, S. Baglio, C. Trigona, N. Dumas, L. Latorre, and P. Nouet, "Nonlinear mechanism in MEMS devices for energy harvesting applications," *J. Micromech. Microeng.*, vol. 20, no. 12, p. 125020, Dec. 2010.

[133] S. C. Stanton, C. C. McGehee, and B. P. Mann, "Nonlinear dynamics for broadband energy harvesting: Investigation of a bistable piezoelectric inertial generator," *Physica D: Nonlinear Phenomena*, vol. 239, no. 10, pp. 640–653, May 2010.

[134] H. Wu, L. Tang, P. V. Avvari, Y. Yang, and C. K. Soh, "Broadband energy harvesting using nonlinear 2-DOF configuration," 2013, vol. 8688, p. 86880B–86880B–11.

[135] C. R. McInnes, D. G. Gorman, and M. P. Cartmell, "Enhanced vibrational energy harvesting using nonlinear stochastic resonance," *Journal of Sound and Vibration*, vol. 318, no. 4–5, pp. 655–662, Dec. 2008.

[136] F. Formosa, T. Büssing, A. Badel, and S. Marteau, "Energy harvesting device with enlarged frequency bandwidth based on stochastic resonance," *Proceedings of PowerMEMS*, pp. 229–232, 2009.

[137] T. Wellens, V. Shatokhin, and A. Buchleitner, "Stochastic resonance," *Rep. Prog. Phys.*, vol. 67, no. 1, p. 45, Jan. 2004.

[138] L.-C. J. Blystad and E. Halvorsen, "An energy harvester driven by colored noise," *Smart Mater. Struct.*, vol. 20, no. 2, p. 025011, Feb. 2011.

[139] L.-C. J. Blystad, E. Halvorsen, and S. Husa, "Piezoelectric MEMS energy harvesting systems driven by harmonic and random vibrations," *IEEE Transactions on Ultrasonics, Ferroelectrics and Frequency Control*, vol. 57, no. 4, pp. 908–919, 2010.

[140] K. W. Yung, P. B. Landecker, and D. D. Villani, "An Analytic Solution for the Force Between Two Magnetic Dipoles," *Magnetic and Electrical Separation*, vol. 9, no. 1, pp. 39–52, 1998.

[141] E. E. Callaghan and S. H. Maslen, *The Magnetic Field of a Finite Solenoid*. 1960.

[142] J. T. Conway, "Exact solutions for the magnetic fields of axisymmetric solenoids and current distributions," *IEEE Transactions on Magnetics*, vol. 37, no. 4, pp. 2977–2988, 2001.

[143] N. Derby and S. Olbert, "Cylindrical magnets and ideal solenoids," *American Journal of Physics*, vol. 78, no. 3, pp. 229–235, Feb. 2010.

[144] M. A. Koplow, A. Bhattacharyya, and B. P. Mann, "Closed form solutions for the dynamic response of Euler–Bernoulli beams with step changes in cross section," *Journal of Sound and Vibration*, vol. 295, no. 1–2, pp. 214–225, Aug. 2006.

[145] S. C. Stanton and B. P. Mann, "On the dynamic response of beams with multiple geometric or material discontinuities," *Mechanical Systems and Signal Processing*, vol. 24, no. 5, pp. 1409–1419, Jul. 2010.